VYSOKÉ UČENÍ TECHNICKÉ V BRNĚ
BRNO UNIVERSITY OF TECHNOLOGY

FAKULTA STROJNÍHO INŽENÝRSTVÍ
FACULTY OF MECHANICAL ENGINEERING

ÚSTAV AUTOMOBILNÍHO A DOPRAVNÍHO INŽENÝRSTVÍ
INSTITUTE OF AUTOMOTIVE ENGINEERING

ANALÝZA RADIÁLNÍCH KLUZNÝCH LOŽISEK S VYUŽITÍM POKROČILÝCH VÝPOČTOVÝCH METOD
RADIAL SLIDE BEARING ANALYSIS USING ADVANCED COMPUTATIONAL METHODS

DIPLOMOVÁ PRÁCE
MASTER'S THESIS

AUTOR PRÁCE — **Bc. Tomáš Orbán**
AUTHOR

VEDOUCÍ PRÁCE — **doc. Ing. Pavel Novotný, Ph.D.**
SUPERVISOR

BRNO 2017

VYSOKÉ UČENÍ TECHNICKÉ V BRNĚ
FAKULTA STROJNÍHO INŽENÝRSTVÍ

Zadání diplomové práce

Ústav:	Ústav automobilního a dopravního inženýrství
Student:	**Bc. Tomáš Orbán**
Studijní program:	Strojní inženýrství
Studijní obor:	Automobilní a dopravní inženýrství
Vedoucí práce:	**doc. Ing. Pavel Novotný, Ph.D.**
Akademický rok:	2016/17

Ředitel ústavu Vám v souladu se zákonem č.111/1998 o vysokých školách a se Studijním a zkušebním řádem VUT v Brně určuje následující téma diplomové práce:

Analýza radiálních kluzných ložisek s využitím pokročilých výpočtových metod

Stručná charakteristika problematiky úkolu:

Práce se zabývá výpočtovou analýzou radiálních kluzných ložisek klikového mechanismu s využitím pokročilých výpočtových metod. Součástí práce je hodnocení vlivu vybraných konstrukčních parametrů a provozních podmínek motoru na tribologické charakteristiky kluzných ložisek. Výpočtové modelování předpokládá uvažování vlivu elastických deformací okolních struktur, vlivu kontaktu nerovností povrchů, tlakově a teplotně proměnné vlastnosti mazacího média. Předpokládá se využití komerčních nástrojů na bázi multibody systémů. Daná problematika je aplikována na moderní spalovací motory.

Cíle diplomové práce:

Rešerše soudobých výpočtových nástrojů pro řešení dynamiky a tribologie ložisek včetně uvedení teoretických předpokladů.
Stanovení parametrů povrchů ložiska na základě reálných vzorků.
Parametrická studie popisující vliv geometrických rozměrů a provozních podmínek motoru na tribologické charakteristiky ložiska.
Vyhodnocení výsledků a definování závěrů pro využití v aplikační sféře.

Seznam doporučené literatury:

GOHAR, Ramsey. Elastohydrodynamics. 2. vyd. London: Imperial College Press, 2001. ISBN 1-86094-170-2.

HAMROCK, Bernard J., SCHMID, Steven R. a JACOBSON, Bo. O. Fundamentals of fluid film lubrication. 2. vyd. New York: Marcel Dekker, 2004. ISBN 0-8247-5371-2.

KHONSARI, Michael M. a Richard E. BOOSER. Applied Tribology: Bearing Design and Lubrication. 2. vyd. London: Wiley, 2008. ISBN 0-7506-7836-4.

STACHOWIAK, Gwidon W. a Andrew W. BATCHELOR. Engineering Tribology. 3. vyd. Boston: Elsevier Butterworth-Heinemann, 2005. ISBN 0-7506-7836-4.

Termín odevzdání diplomové práce je stanoven časovým plánem akademického roku 2016/17

V Brně, dne

L. S.

prof. Ing. Václav Píštěk, DrSc. ředitel ústavu	doc. Ing. Jaroslav Katolický, Ph.D. děkan fakulty

ABSTRACT

This master's thesis introduces a slide bearing analysis using the MBS software tool of FEV Virtual Engine, including real surface topography based on 3D roughness measurements. The first half of the thesis gives a brief overview about gasoline combustion engines, slide bearing usage in engines, slide bearing construction and about essential approaches for the characterization of elasto-hydrodynamic behavior. In the second half, the process of model building, rough surface measurement and preparation of analyses are described. At the end of this thesis, the results of the analyses are shown and discussed.

KEYWORDS

radial slide bearing, cranktrain, rough surface profile, flow-factors, steady-state analysis, tribology, elasto-hydrodynamics, asperity contact

ABSTRAKT

Tato diplomová práce uvádí analýzu kluzných ložisek pomocí MBS softwaru FEV Virtual Engine zahrnutím struktury reálných povrchů získané pomocí 3D měření drsného povrchu. První polovina práce udává stručný přehled o zážehových motorech, využití kluzných ložisek v motorech, konstrukci kluzných ložisek a o základních přístupech charakterizujících problematiku elasto-hydrodynamiky. V druhé polovině je popsán postup vytvoření modelu, proces měření vzorků a příprava simulací. Na konci této práci jsou uvedené a projednávané výsledky analýz.

KLÍČOVÁ SLOVA

radiální kluzné ložisko, klikový mechanismus, profil drsného povrchu, faktory toku, analýza ustáleného stavu, tribologie, elasto-hydrodynamika, kontakt nerovností

BIBLIOGRAPHIC CITATION

ORBÁN, T. Radial Slide Bearing Analysis Using Advanced Computational Methods. Brno: Brno University of Technology, Faculty of Mechanical Engineering, 2017. 97 p. Supervisor: doc. Ing. Pavel Novotný, Ph.D.

DECLARATION OF AUTHORSHIP

I, Tomáš Orbán, hereby declare that this master's thesis – "Radial Slide Bearing Analysis Using Advanced Computational Methods" – is my own work and all the sources have been quoted and acknowledged by means of a complete list of references in this document.

Brno, May 26, 2017 ……..……..……..

Tomáš Orbán

ACKNOWLEDGEMENT

First of all, I would like to thank my supervisor, doc. Ing. Pavel Novotný, Ph.D. for his advices during completing this master's thesis. I would like to thank Dr. Michal Pavlov, for his helpfulness, support and friendly attitude during my internship at Škoda Auto in Mladá Boleslav.
Special thank belongs to my family for their constant and unlimited love, support and belief in me, not only during my university studies.

CONTENT

INTRODUCTION

Since the last decades of the 20th century, the exhaust gas emissions of new passenger cars, light-duty vehicles and heavy-duty vehicles are being regulated. In the last few years, the limitations agreed by the Parliament of the European Union became a lot stricter, which exerts an enormous pressure on the engine manufacturers. For this reason, they must raise their invests in research and development. These costs can be effectively moderated by using reliable computations, involving as many factors of real parameters and conditions as possible. However, these cannot replace the expensive testing procedures of newly developed engines, but the major part of the critical cases can be eliminated before the building of the first engine prototypes.

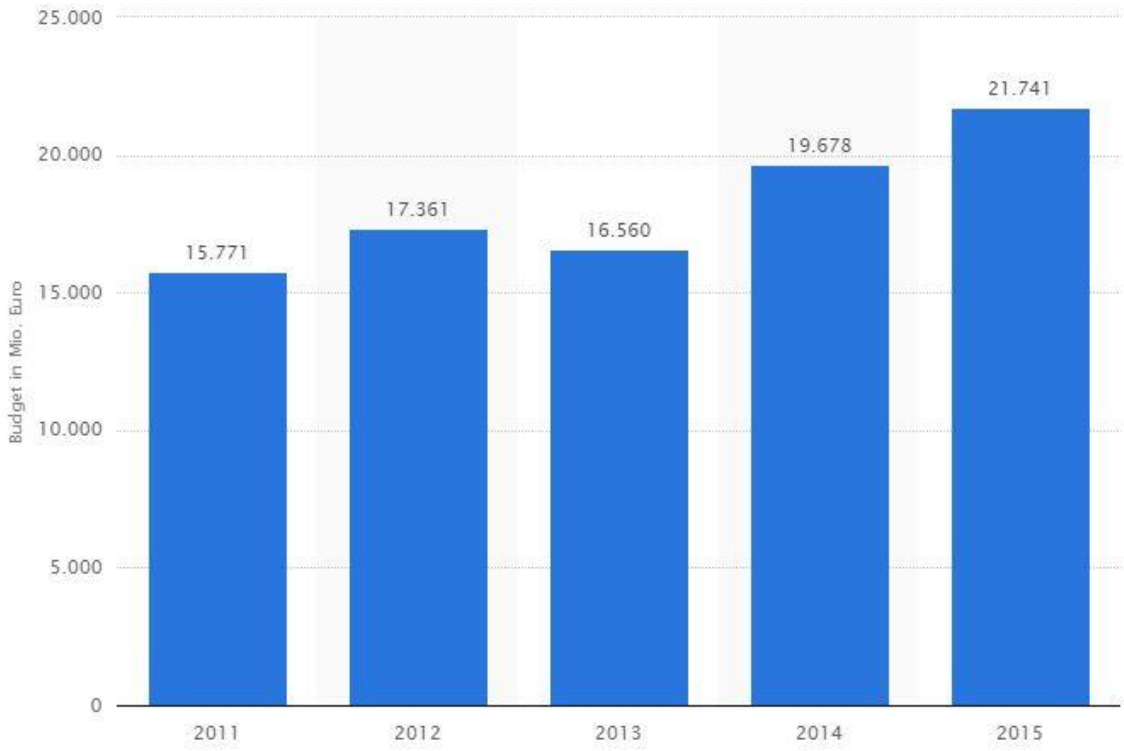

Figure 1 Investments of the German automobile manufacturers into research and developement [30]

1 FUNDAMENTALS OF GASOLINE FOUR-STROKE INTERNAL COMBUSTION ENGINE (ICE)

A modern four-stroke petrol engine is a heat engine, which transforms the chemical energy of the fuel to mechanical work. To complete one power cycle, each cylinder undergoes four piston strokes, what represents two revolutions of the crankshaft. [6]

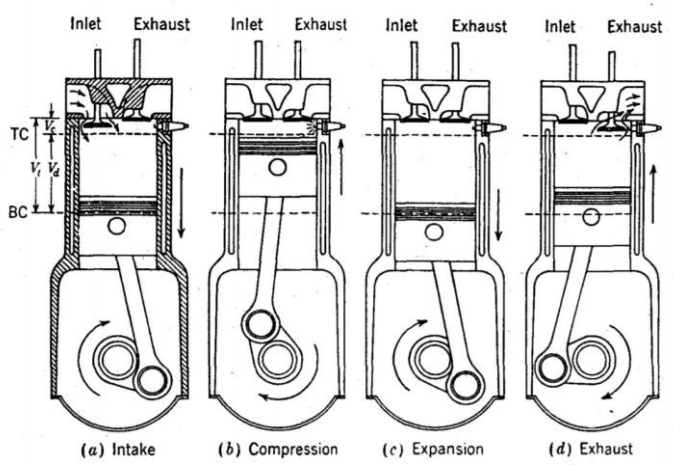

Figure 2 Operating cycles of four-stroke engines [6]

In the first section of the cycle the piston moves downwards, creating subatmospheric pressure in the cylinder. In the case of engines with indirect injection this motion draws fresh air-fuel mixture into the combustion chamber. Otherwise, in the case of direct injection engines only fresh air is sucked in and the mixture is prepared directly in the cylinders. This section lasts until the piston reaches the lowest position, called bottom dead center (BDC), when the cylinder volume is at its maximum (V_t).

The second phase of the cycle is the compression. The mixture in the cylinder is compressed by the piston, until top dead center (TDC) crank position is achieved. At this position, the mixture is compressed to the minimum cylinder volume, called the clearance volume (V_c). The ratio of maximum to minimum volume is the compression ratio. The typical value of compression ratio of a gasoline engine is between 8 and 12.

Third step is initiated by the ignition of the air-fuel mixture. The pressure and the temperature in the combustion chamber rapidly rises and pushes the piston downwards, forcing the crankshaft to rotate. This phase is also called as power stroke.

The fourth, exhaust stroke finishes the cycle. While the piston moves towards the TDC the remaining burned gases exit the cylinder. [6]

1.1 Forces Acting on the Crank Mechanism

The crank mechanism of a multi-cylinder gasoline engine consists of the piston assemblies (piston, piston rings and pin), connecting rods and crankshaft. The whole assembly is designed to convert cyclic linear motion of the pistons to rotation. These elements of an internal combustion engine are highly loaded by the gas forces produced in the combustion chamber (primary forces) and by the inertia forces caused by the rotation and translation of masses (secondary forces). These time dependent variables are continuously changing their direction of acting and magnitude, causing enormous load on the engine parts [8][7].

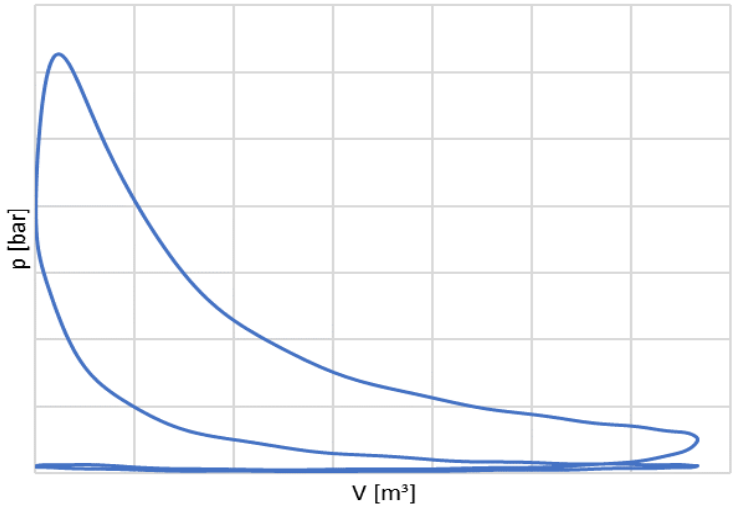

Figure 3 p-V diagram for a four-stroke cycle petrol engines

1.1.1 Primary Forces

Primary forces burdening the crank assembly originate from the gas pressure above the piston in the combustion chamber.

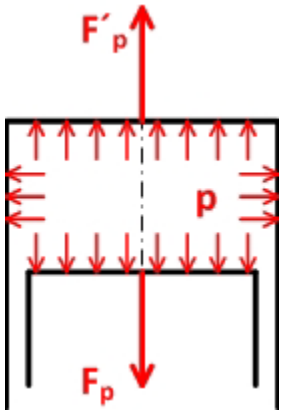

Figure 4 Gas forces in the combustion chamber [3]

The gas pressure equally strains the cylinder wall, the cylinder head and the piston. The gas force obtruding the piston for motion is defined as:

$$F_P = \frac{\pi \cdot D^2}{4} \cdot \left(p_g - p_0 \right), \tag{1}$$

where D is the cylinder bore diameter, p_g is the pressure in the combustion chamber and p_0 represents the atmospheric pressure. For a given engine both the cylinder bore diameter and atmospheric pressure have a constant value, therefore the gas force F_p is only dependent on the pressure in the combustion chamber. The gas pressure is on the function of the angle of rotation of the crankshaft. Combustion takes place once per period of a four-stroke cycle, therefore every 720 degrees is one peak in gas pressure [3].

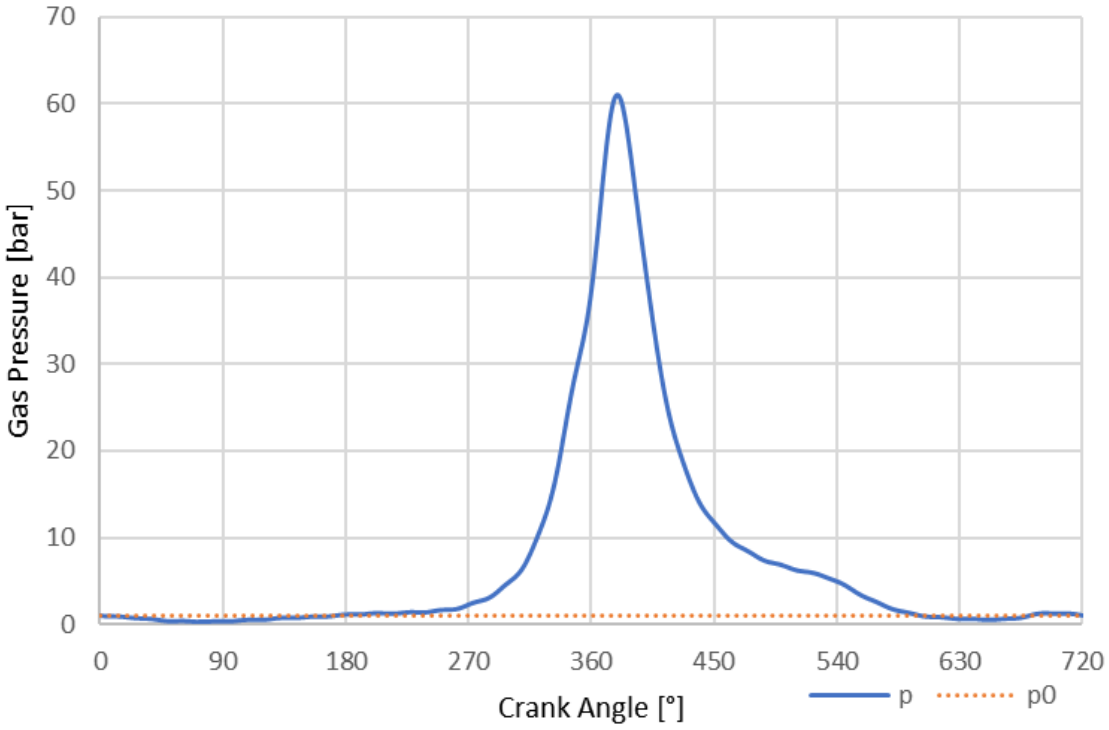

Figure 5 Pressure-crank angle diagram

1.1.2 SECONDARY (INERTIA) FORCES

The scale of inertia forces acting on the crank assembly is given by the mass of moving parts and by the magnitude of the acceleration of their motion. For simple computational purposes the weight of the connecting rod is reduced into two mass points so that static and dynamic properties, total weight, center of gravity and moment of inertia remain unchanged. One mass point is placed in the conrod's small end, and performs translational movement. The second mass point takes place in the center of the conrod's big end, where only rotational movement is carried out [14]. All these forces can be discretized and lots of equations could to be demonstrated for their calculation, which is not the aim of this master's thesis.

2 RADIAL SLIDE BEARINGS IN AN ICE

Reciprocating engines are characterized by cyclic loading of their parts, especially bearings. Only slide bearings can deal with a sufficient wide range of applied load to allow to be mounted in an internal combustion engine.
Radial slide bearings are used in present modern internal combustion engines at several places to support the crankshaft, camshaft or balancing shaft. Other slide bearings, like conrod bearings, piston pin bearings are used to link the piston, conrod and crankshaft together, and to transfer forces from pistons to crankshaft [21].

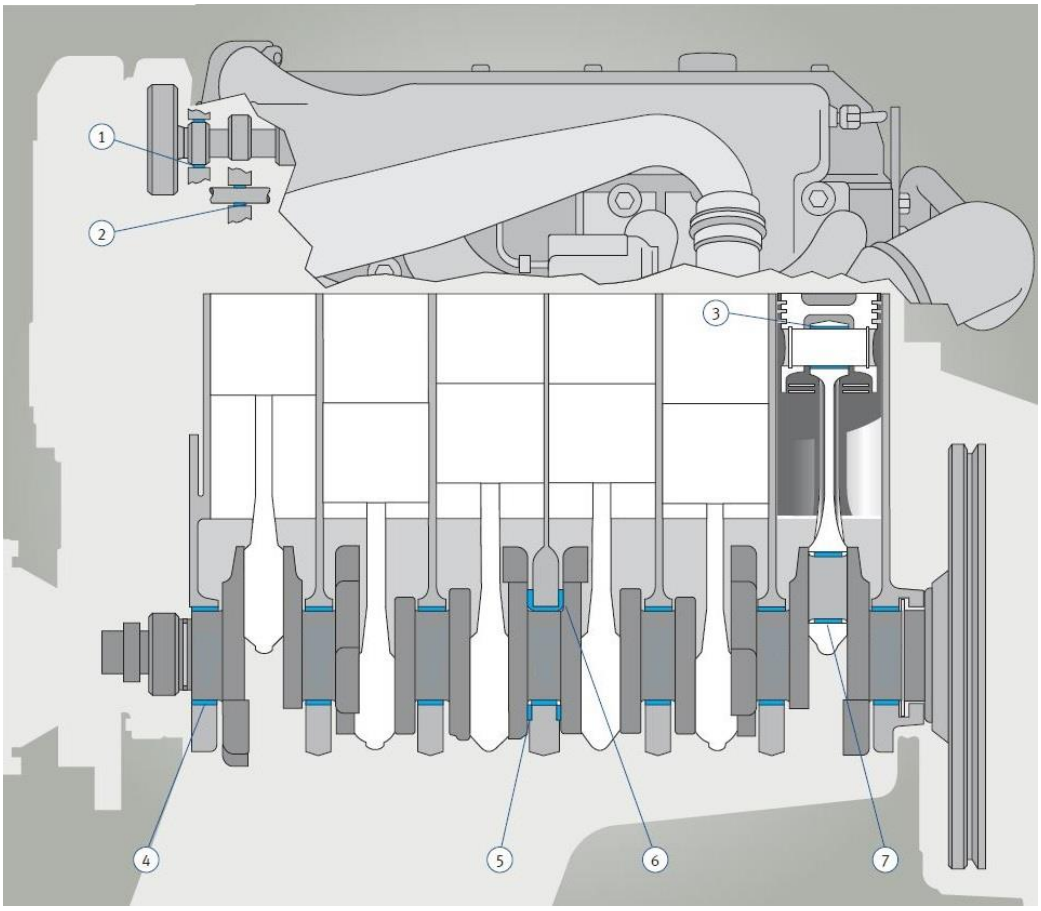

1. Camshaft bearing *2. Rocker arm bush* *3.Conrod bush* *4. Main bearing*

5. Thrust washer *6. Flanged bearing* *7. Conrod bearing*

Figure 6 Engine bearings [18]

Conrod bush in cooperation with piston pin allow relative motion of piston and connecting rod. Piston pin bushing is commonly molded into the small end of the connecting rod.
The connecting rod transfers gas forces to the crankshaft through crankpin bearing, where the translational motion of piston is transferred to rotation. Crankpin bearings are placed in the big end of the connecting rod and consist of two parts, which are commonly interchangeable.
Main bearings are placed in the crankcase, providing support for the crankshaft, which carries the load from the combustion pressure and the load from the rotation and translation of masses. A main bearing consists of two parts: upper and lower bearing shell. The upper part of the main bearing commonly has an oil groove on the inner surface. A main bearing also has a hole for passing oil to the feed holes in the crankshaft. Some main bearings in addition to enable the rotating movement of the shaft, may also have thrust elements supporting the crankshaft in the axial direction. Main bearings of such type are called flange main bearings [21].

2.1 CONSTRUCTION OF RADIAL SLIDE BEARINGS

Flat bearing shells

Flat bearing shells are in use in an internal combustion engine as main and conrod bearings. Commonly they consist of thin-walled composite bearing shells. These types of slide bearings have a steel back, which is plated with the bearing metal [18].

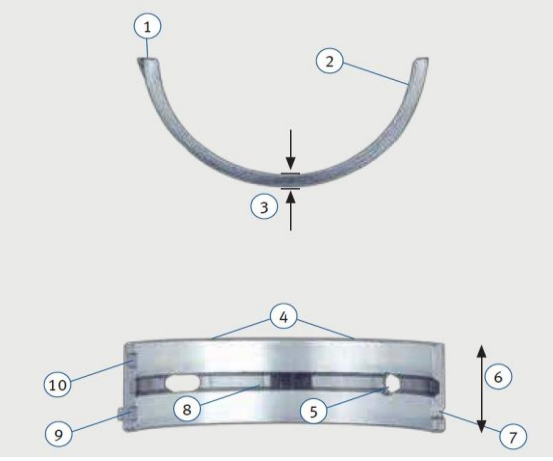

1. Parting face
2. Bore relief
3. Wall thickness
4. Face relief
5. Oil hole
6. Bearing width
7. Locking hole
8. Inside oil groove
9. Left cam
10. Right cam

Figure 7 Construction of a flat bearing shell [18]

Flanged bearing shells

Flanged bearing shells, or collar bearing shells are designed to support the crankshaft in longitudinal direction as well. Depending on the engine design, one or two flanged bearing shells are mounted [18].

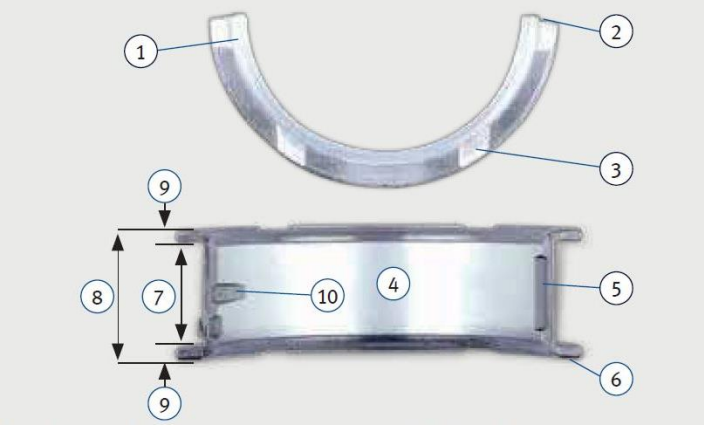

1. Thrust face relief
2. Parting face relief
3. Oil groove on thrust face
4. Sliding surface
5. Oil distributing pocket
6. Face relief
7. Flange spacing
8. Bearing width
9. Flange thickness
10. Crescent groove

Figure 8 Flanged bearing construction [18]

Thrust washers

Thrust washers are responsible for guiding the crankshaft axially. They are a substitute for flanged bearings in conjunction with flat bearing shells. Along the outside diameter of thrust washers locking lugs are placed to prevent rotation. This type of axial guiding of the crankshaft needs a specially designed bearing housing, and they cannot be replaced by flanged bearings [18].

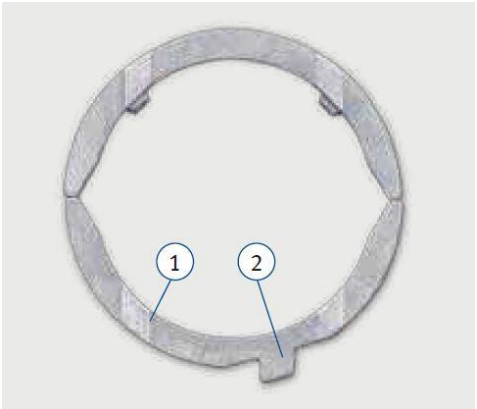

1. Oil groove
2. Locking lugs

Figure 9 Thrust washer construction[18]

The axial forces, caused by clutch pressure and vehicle dynamics while driving, are absorbed by the thrust washers or by the flanges of the flanged bearing shells.

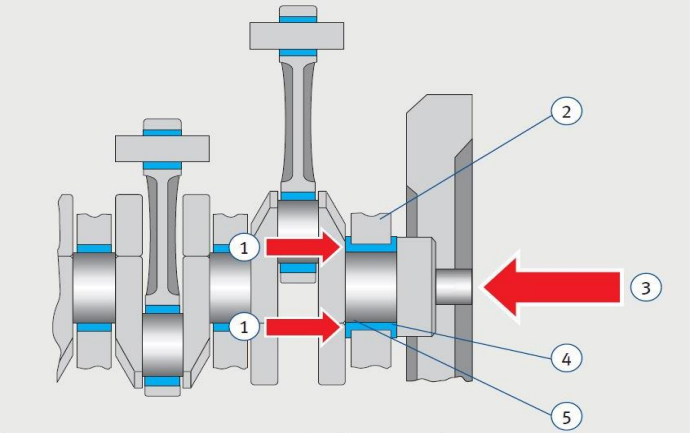

1. Guiding forces
2. Casing
3. Clutch pressure
4. Thrust bearing
5. Radial bearing

Figure 10 Axial forces acting on the crankshaft [18]

2.2 BEARING MATERIALS

Materials used for the production of slide bearings must fulfill several requirements to ensure long life and durability of vehicle engines at every condition, such as [22]:

- Resistance to -fatigue damage,
  -erosion,
  -cavitation,
  -abrasive wear and
  -corrosion.
- Ability to absorb dirt.
- Adaptability.

The bearing materials have to be strong but soft at the same time. In the ideal case the bearing material must be able to carry high load at high temperatures to reliably work with insufficient amount of oil, to absorb contaminations and to resist erosive and corrosive impact of the lubricant. Besides these resistive properties, the bearing material has to excel with possibly the lowest coefficient of friction [22].
To match the above-mentioned properties, bearing materials have a composite structure. In the following section two types of composite bearing structures are presented, the one introduced by KS Gleitlager GmbH, and another, specially developed for engines with start-stop system by Federal-Mogul.

Steel-aluminum composite

Plain bearings made of lead-free steel-aluminum composite materials are widely used as main and conrod big-end bearings in gasoline and diesel engines. Bearing structure is composed of steel back, an intermediate layer made of pure aluminum and an aluminum-tin-copper running layer. The thickness of individual layers is defined as a function of theapplication. The thickness

of the steel layer ranges between 1.0 to 3.0 mm, the thickness of the intermediate layer varies between 0.01 and 0.05 mm and the thickness of the running layer measures between 0.2 and 0.5 mm. These types of bearing materials are suitable to be applied in common internal combustion engines from low specific performance to higher performance class [23].

Figure 11 Steel-Aluminum composite bearing structure [23]

Steel-brass composite

Hydrodynamic bearing shells made of lead-free steel-brass composite with sputtered running surface are suited for highly supercharged diesel engines. The bearing steel back is coated with a 0.2 to 0.5 mm thick brass alloy layer and a sputtered-on aluminum-tin-copper alloy. This 8.0 to 16.0 µm thick layer is separated from the brass layer by a 1.0 to 3.0 µm thin nickel diffusion barrier, which prevents uncontrolled diffusion of the components of the sliding layer and the overlay layer [24].

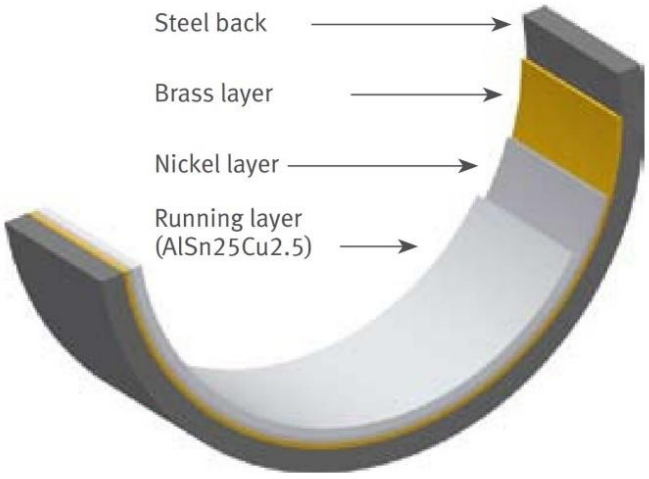

Figure 12 Steel-brass composite bearing structure [24]

Steel-aluminum composite bearing material with polymer coating

In vehicle engines with start-stop system the journal bearings are more affected by boundary and mixed lubrication regimes, than ever. The engines designed 10-20 years before were commonly engineered for up to 100.000 engine startups, whereas at engines equipped with start-stop this number reaches up to 300.000 start cycles. The coating layer of the bearing structure must be able to resist the raised amount of boundary and mixed friction regimes to ensure the expected lifetime of the engine [19].
For this purpose, a polymer coating was developed, made of polymer resin binder with the addition of anti-wear additive and solid lubricant. Based on the test results made with and without the polymer coating, following conclusions are reported [19]:

- up to 90% lower wear,
- up to 30% lower coefficient of friction,
- up to 25% higher load carrying capability,

compared to a conventional bare aluminum bearings.

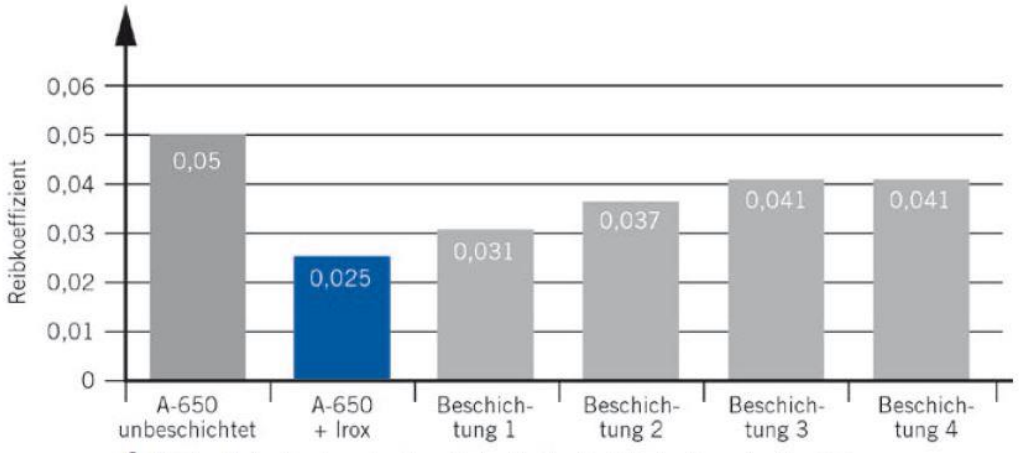

Figure 13 Coefficient of friction of various bearing materials[19]

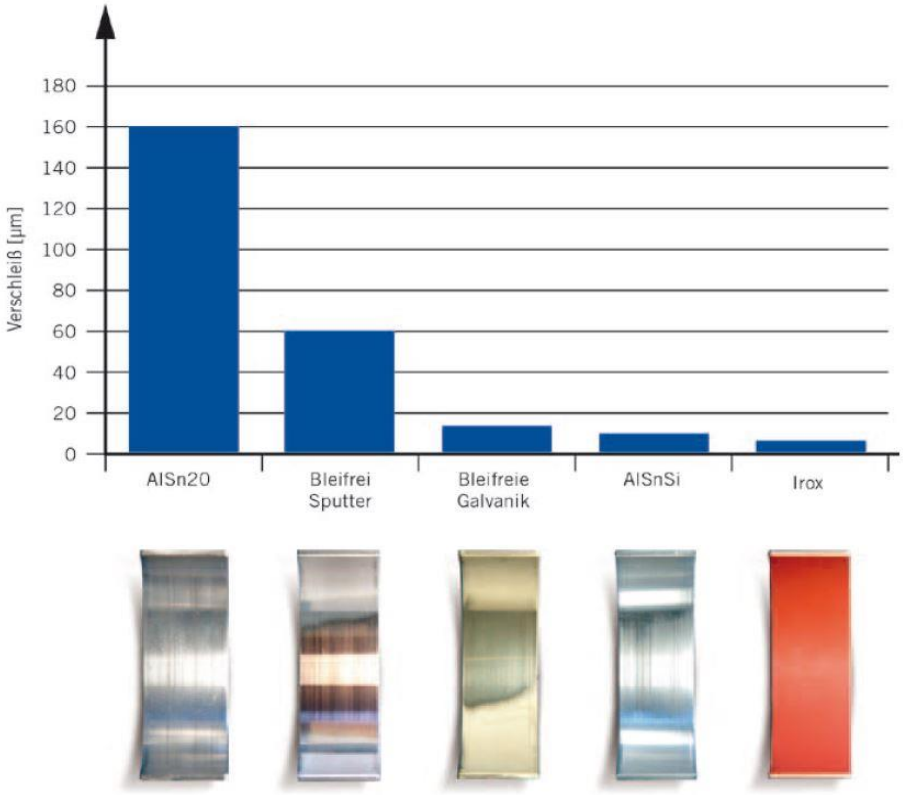

Figure 14 Wear of various bearing materials after 15000 cycle [19]

3 TRIBOLOGY

Tribology is defined by DIN 50320 norms as a study that deals with the design, friction, wear and lubrication of interacting surfaces in relative motion. In the picture is shown a tribosystem, represented by two bodies in relative motion and medium filling the gap between the entities [1].

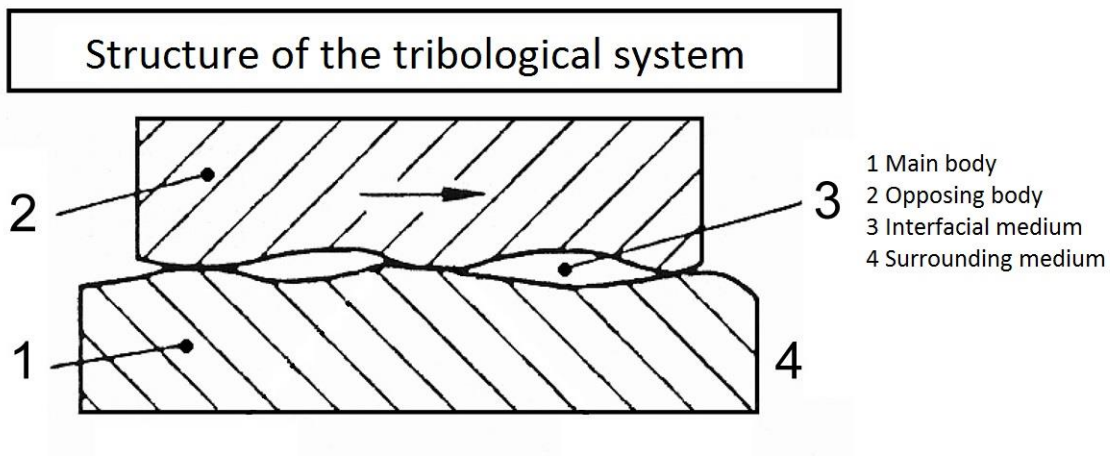

Figure 15 Tribological system [1]

3.1 FRICTION

Friction between interacting bodies does exist as well in the nature as in the wide range of fields in the science. Friction is responsible for energy loss causing fall of efficiency of mechanisms. The main disadvantage of friction is wear, which causes reduced service life and reliability of moving parts of machines. Overleaf the friction is necessary if accelerating, breaking or stop of moving parts is required.

Investigating of friction was initiated for about 500 years by Leonardo da Vinci. He has declared the friction depends on the load and is independent of the contact area. 1785 Charles-Augustin de Coulomb published his studies about static and kinetic friction and formed laws of friction. Coulomb as the first hypothesized that one of the reasons of friction is cohesion of molecules between the moving surfaces [26].

Friction is relatively complicated physical phenomena. The surface of every object has a complex topology on microscopic scale represented by peaks and valleys. For this reason, two bodies are never in full contact. Upper body is supported by the peaks of the surface of lower body. The real contact area between the surfaces represents approximately the one ten-thousandth of the visible contact area [20].

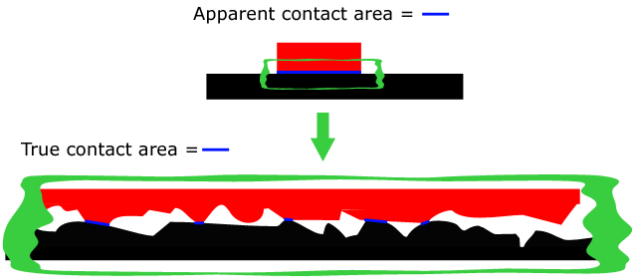

Figure 16 True vs. Apparent contact area [32]

3.2 LUBRICATION

Lubrication is one of the most effective ways to reduce sliding friction and wear, and to improve effectiveness and reliability of machine parts. The inner engine components are lubricated by constant supply of engine oil. In order to lubricate all the moving part of the engine, all oil systems use common components [31]:

- oil pump,
- relief valve,
- oil filter,
- oil passages,
- oil cooler,
- oil pan and
- oil jets.

The main bearings of the crank do have their own oil supply via oil passages in the block. The oil channel bored from main bearings through the web provides the needed amount of oil to the crankpin journals.

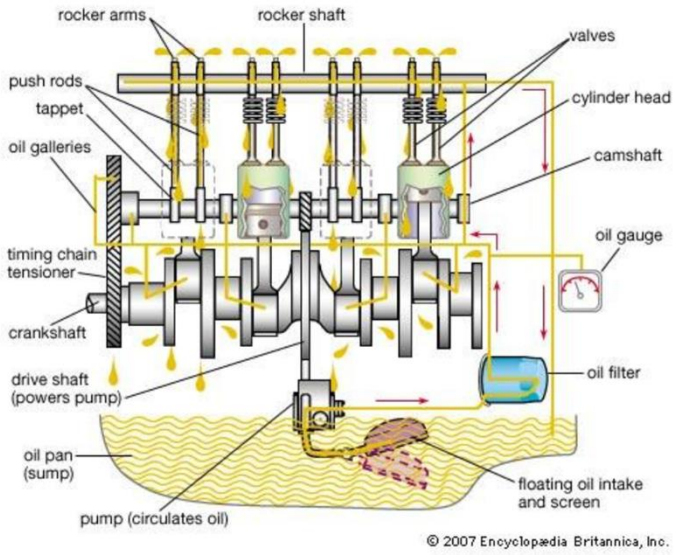

Figure 17 Lubrication system of ICE [28]

3.3 LUBRICATION REGIMES

Depending on the amount of lubricant, load and relative velocity of surfaces of hte tribological system, four basic lubrication regimes can occur in engine bearings:

- boundary lubrication,
- mixed lubrication,
- hydrodynamic lubrication and
- elasto-hydrodynamic lubrication.

The Stribeck curve describes the frictional characteristics of a liquid lubricant over the lubrication regimes. Each regime is defined by the ratio of the film thickness to the surface roughness h/σ.

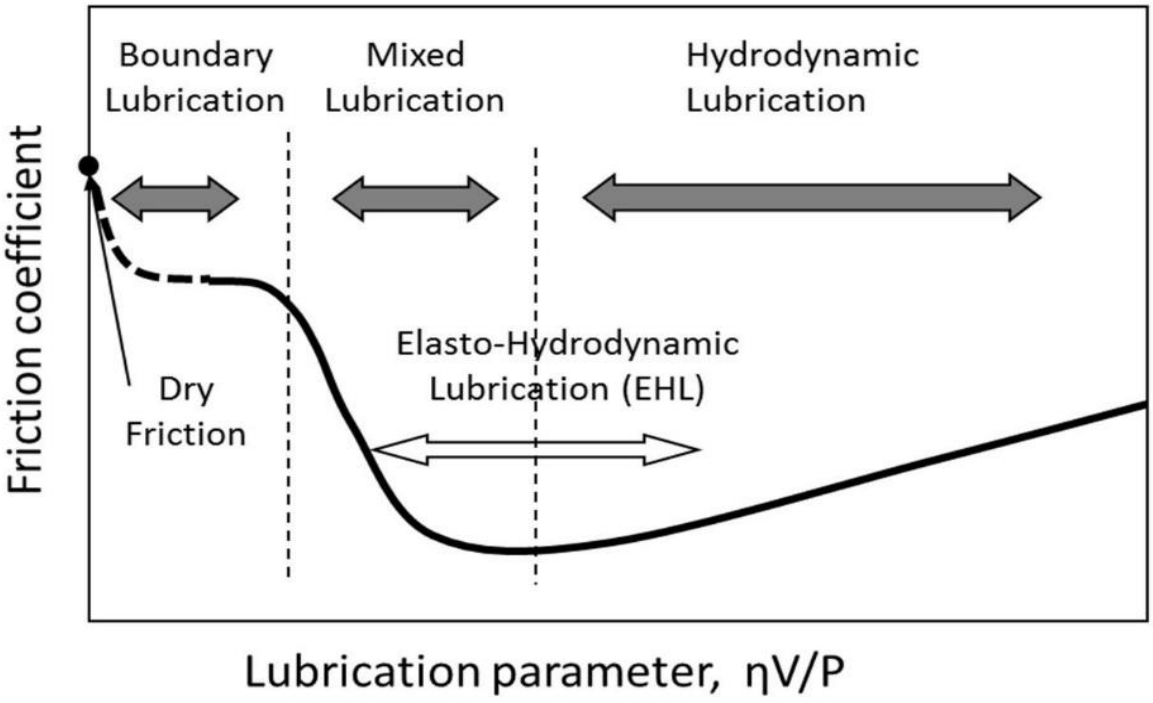

Figure 18 Stribeck curve [33]

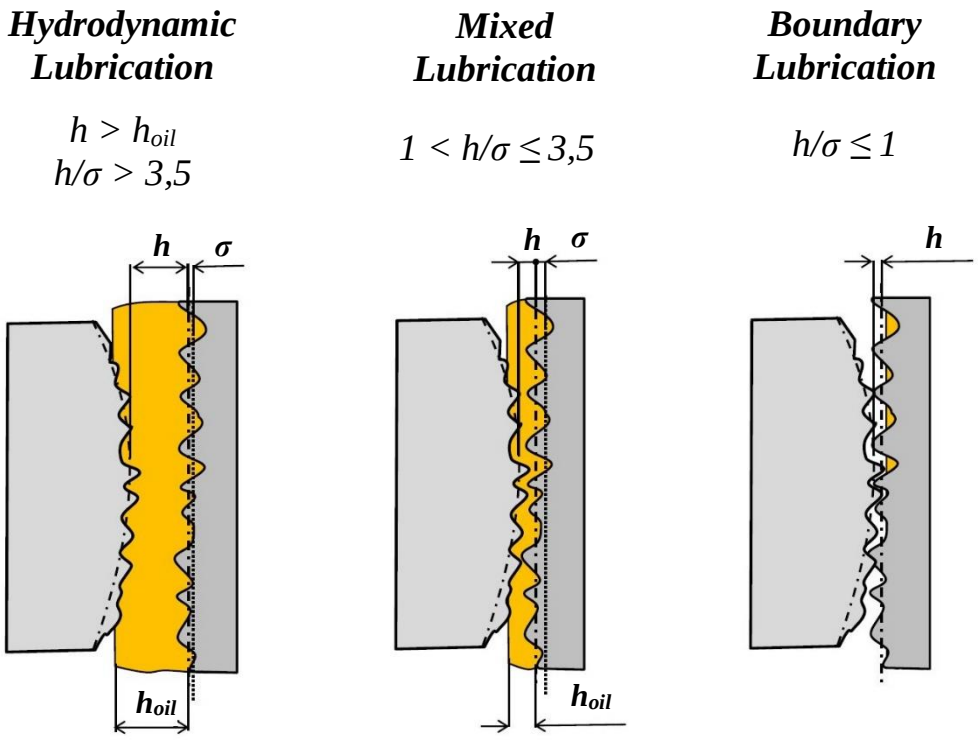

Figure 19 Lubrication regimes [25]

Boundary lubrication

Boundary lubrication regime in the engine's journal bearings is the result of very low speed (engine startup or shutdown), or extreme bearing loads. In the case of boundary lubrication constant contact occurs between the microasperities. This regime is the most unwanted, because of the increased coefficient of friction, elevated wear and unfavorable load distribution.

Mixed lubrication

The mixed lubrication regime represents limited load support from the lubricant film and partial load support from direct contact of surface irregularities.

Hydrodynamic lubrication

Hydrodynamic lubrication regime is the most desired condition in the engine's journal bearing. There is no contact between the bearing journal and shell. It occurs at high rotation speed at relatively low bearing load.

3.4 THEORY OF FUNCTION OF RADIAL SLIDE BEARINGS WITH HYDRODYNAMIC LUBRICATION

Radial slide bearings in internal combustion engines are hydrodynamic journal bearings, in which the bearing surface is separated from the journal surface by a lubricant film generated by the journal's rotation. For the fluid film pressure generation is indispensable a viscous lubricant and the relative motion of the surfaces, which pulls the lubricant into a wedge-shaped zone. For the creation of a necessary pressure separating the surfaces, the relative velocity of rotating surfaces must be sufficiently high. Hydrodynamic lubrication suggests that the surfaces of the bearing are separated by a relatively thick film of lubricant. So is prevented metal to metal contact [15].

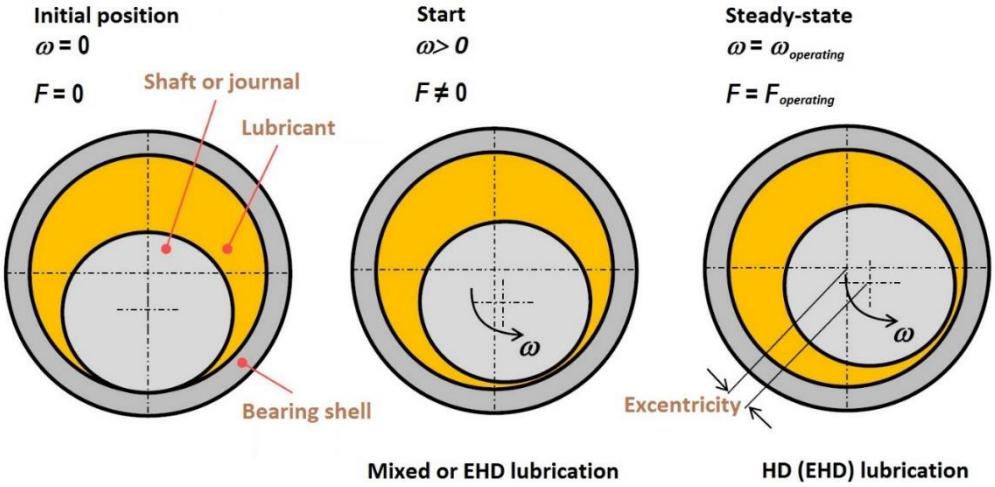

Figure 20 Journal bearing operating regimes [25]

4 ELASTO-HYDRODYNAMICS (EHD)

Elasto-hydrodynamic lubrication (EHL) is a form of hydrodynamic lubrication, where the elastic deformations of engaging bodies and the dependence of viscosity and density of lubricant on pressure are considered.
In this section, the basic EHL with a Newtonian lubricant behavior is introduced. Newtonian lubricant means that the dependence between the shear stress τ and the shear rate v/h is linear [15]:

$$\tau = \eta \frac{v}{h} \tag{2}$$

For the description of EHD problematics a complex set of equations is necessary to be introduced:

- Reynolds equation,
- pressure-viscosity relation,
- pressure-density dependence,
- contact pressure determination and
- force equilibrium equation.

4.1 REYNOLDS EQUATION

The characterization of real fluid behavior consists of many factors and variables, which make a description highly difficult. It is too complicated to be easily described by exact mathematical equations, hence several simplifying assumptions were made. For the derivation of the Reynolds equation these are the following [15]:

- body forces are neglected,
- pressure is constant through the lubricant film,
- no slip at the boundaries (surface velocity is equal to lubricant speed),
- the lubricant behaves as a Newtonian fluid,
- the lubricant flow is laminar,
- fluid inertia is neglected,
- the lubricant viscosity is constant through the lubricant film and
- the lubricant density is constant.

The Reynolds differential equation, derived by Osborne Reynolds in 1886 from the Navier-Stokes and mass conservation equations, for describing the fluid pressure distribution in a narrow-shaped gap has a form of [16]:

$$\frac{\partial}{\partial x}\left(\frac{\rho h^3}{\eta}\frac{\partial p}{\partial x}\right)+\frac{\partial}{\partial y}\left(\frac{\rho h^3}{\eta}\frac{\partial p}{\partial y}\right)=6U\frac{\partial(\rho h)}{\partial x}+12\frac{\partial(\rho h)}{\partial t}, \tag{3}$$

where

$$U=\frac{U_1+U_2}{2}, \tag{4}$$

where ρ is the lubricant density, h is the nominal lubricant film thickness, η is dynamic viscosity of lubricant, p is the hydrodynamic pressure in the oil film, U_1 and U_2 are the tangential velocities of surface 1 and 2, respectively, x is the Cartesian coordinate in the tangential direction of the motion, y is the Cartesian coordinate in the axial direction and t denotes the time.

4.2 MODIFIED REYNOLDS EQUATION

The basic Reynolds equation was revised by researchers Patir and Chang, and was extended by so-called flow factors, so it can be applied to lubricant pressure calculation with the impact of rough surface structures [11]. The developed formula describes the connection between the hydrodynamic lubrication and the mixed lubrication regime, and can be written in the form [9]:

$$\frac{\partial}{\partial x}\left(\phi_x\frac{\rho h^3}{12\eta}\frac{\partial p}{\partial x}\right)+\frac{\partial}{\partial y}\left(\phi_y\frac{\rho h^3}{12\eta}\frac{\partial p}{\partial y}\right)=\frac{U_1+U_2}{2}\frac{\partial(\rho h_T)}{\partial x}+\frac{U_1-U_2}{2}\sigma\frac{\partial(\rho\phi_s)}{\partial x}+\frac{\partial(\rho h_T)}{\partial t}, \tag{5}$$

where

$$\sigma=\sqrt{\sigma_1^2+\sigma_2^2}, \tag{6}$$

where ϕ_x, ϕ_y and ϕ_s are the flow factors, h_T is the local oil film thickness and σ is the standard deviation of combined surfaces roughness.

The local lubricant film thickness h_T is the sum of the nominal lubricant film height h and the amplitudes of rough surface irregularities δ_{R1} and δ_{R2} [11]:

$$h_T=h+\delta_{R1}+\delta_{R2} \tag{7}$$

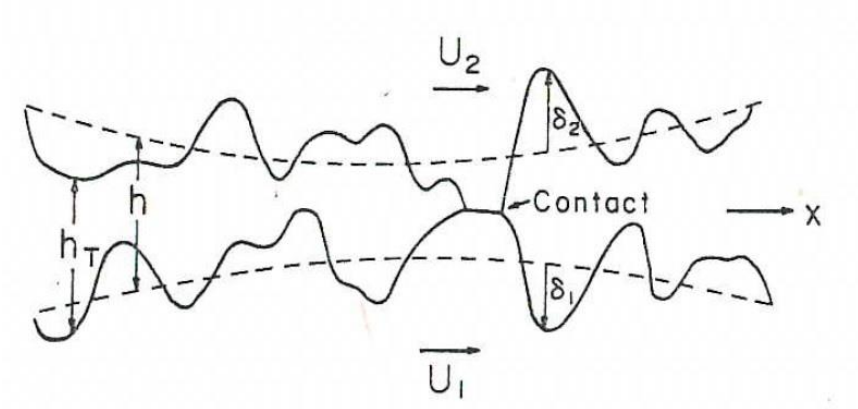

Figure 21 Local lubricant film thickness [11]

Pressure flow factors

The equations for the calculation of pressure flow factors are different for isotropic and non-isotropic surface structures. In case of isotropic surface equation (8) is used [11]:

$$\phi_{x(y)} = 1 - 0.9e^{-0.56(h/\sigma)}. \tag{8}$$

For non-isotropic surfaces the pressure flow factors are described with the following equations [11]:

$$\phi_x = 1 - Ce^{-r'(h/\sigma)} \text{ for } \gamma \le 1, \tag{9}$$

$$\phi_x = 1 + C\left(h/\sigma\right)^{-r'} \text{ for } \gamma > 1. \tag{10}$$

C and *r* are parameters for pressure flow factor calculation, its values are shown in reference [11] as function of γ. Parameter γ denotes the Peklenik number which is the characteristic number for the directional orientation of rough surfaces [11].
At this point it must be noted, that isotropic surfaces do not exist in real. A product of every machining process is a rough surface with directional dependency of $\gamma \neq 1$.

For pressure flow factor in *y* direction of surface is valid [11]:

$$\phi_y\left(h/\sigma, \gamma\right) = \phi_x\left(h/\sigma, 1/\gamma\right) \tag{11}$$

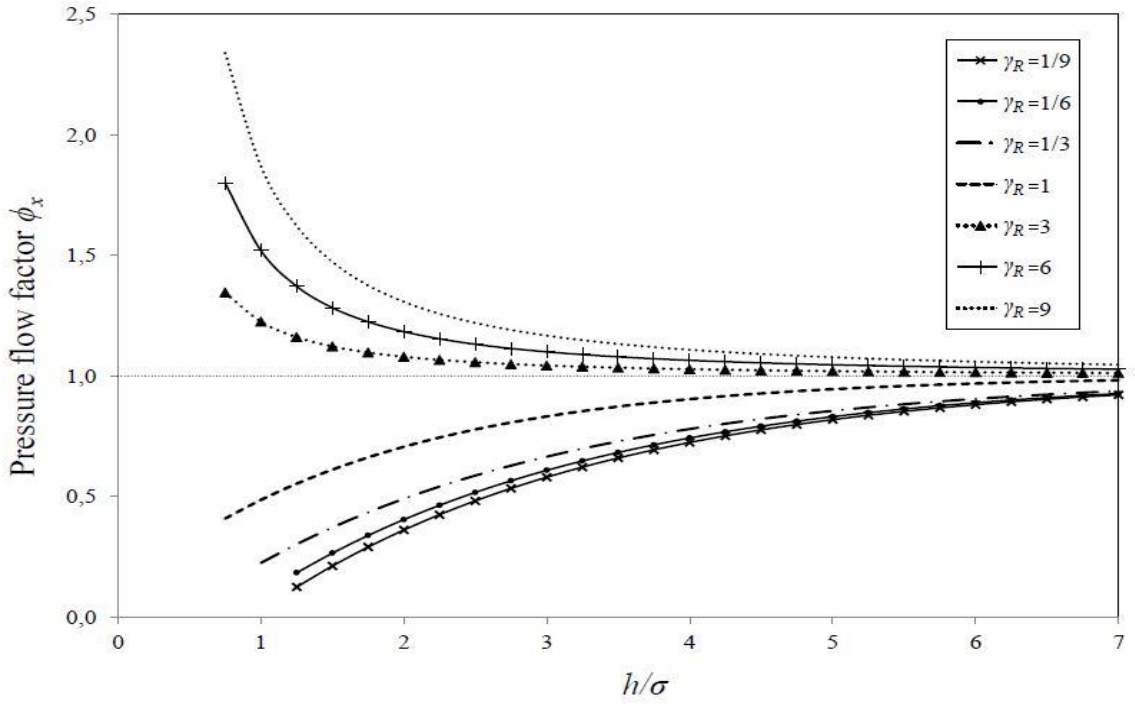

Figure 22 Pressure flow factor [9]

Shear flow factor

According to the research work of Patir and Cheng the shear flow factor can also easily be calculated using the following expressions [12]:

$$\phi_s = A_1 \cdot (h/\sigma)^{\alpha_1} e^{-\alpha_2 \cdot (h/\sigma) + \alpha_3 \cdot (h/\sigma)^2} \text{ for } h/\sigma \leq 5 \tag{12}$$

and

$$\phi_s = A_2 \cdot e^{-0.25 \cdot (h/\sigma)} \text{ for } h/\sigma > 5. \tag{13}$$

A_1, A_2, α_1, α_2 and α_3 are parameters for shear flow factor calculation, its values are shown in reference [12] as a function of γ.

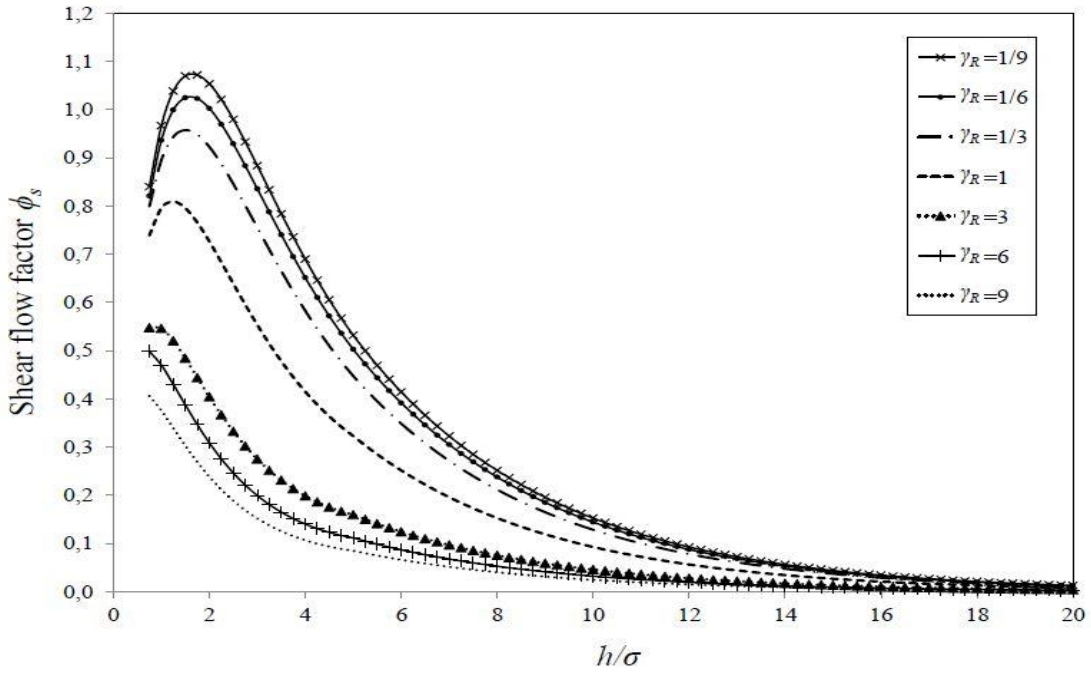

Figure 23 Shear flow factor[9]

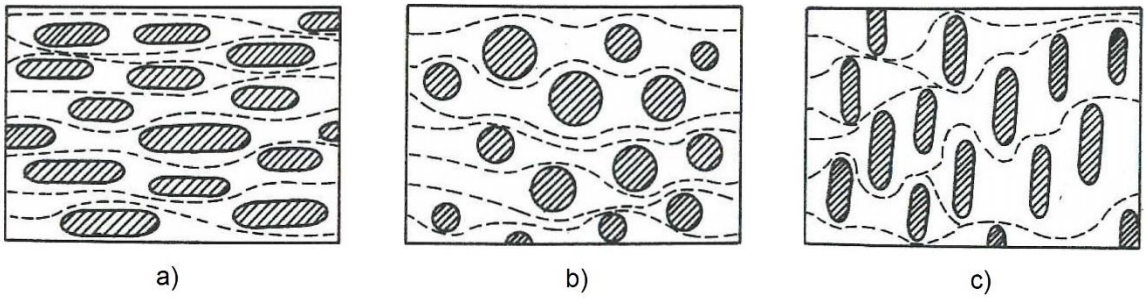

Figure 24 Typical contact areas for a) longitudinally, b) isotropic and c) transversely oriented surfaces [11]

4.3 PRESSURE DEPENDENCE OF VISCOSITY

The simplest relation which describes the dependence of viscosity on pressure was introduced in 1893 by Carl Barus [2]:

$$\eta(p) = \eta_0 e^{\alpha p}, \tag{14}$$

where η_0 stands for the viscosity at atmospheric pressure, α represents the pressure-viscosity coefficient. However, this relation is applicable only for approximation of variety of viscosity only in a narrow range of load [15].

For more accurate calculation Roelands has proposed a relation for isothermal conditions [13]:

$$\eta(p) = \eta_0 \exp\left(\left(\ln(\eta_0) + 9,67 \right) \left(-1 + \left(1 + \frac{p}{p_0} \right)^z \right) \right), \tag{15}$$

where z is the pressure-viscosity index with typical value of around 0.6 and p_0 has a constant value of $1.96 \cdot 10^8$ Pa.
Roelands' relation properly defines the relationship between pressure and viscosity up to 1 GPa, whereby the relation of Barus delivers proper values only up to 0.1 GPa [15].

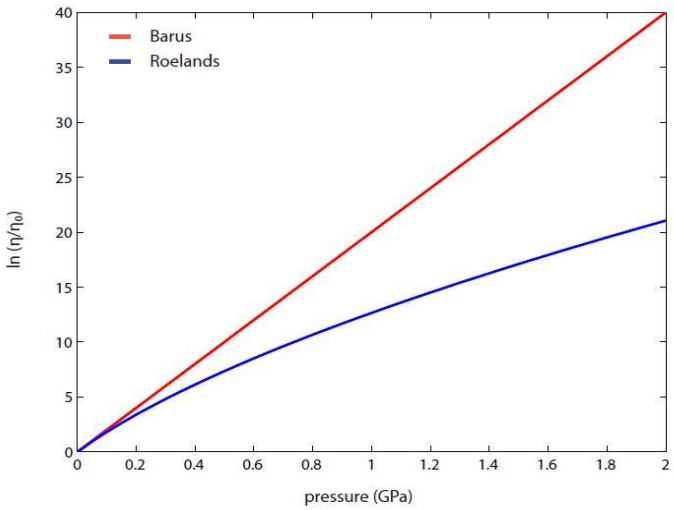

Figure 25 Pressure dependence of viscosity by Barus and Roelands [4]

4.4 PRESSURE DEPENDENCE OF DENSITY

The value of density of fluids also varies with pressure. Dowson and Higginson published an appropriate relation for the calculation of density under pressure as follows:

$$\rho(p) = \rho_0 \frac{5,9 \cdot 10^8 + 1,34p}{5,9 \cdot 10^8 + p}, \tag{16}$$

where ρ_0 is the lubricant density at atmospheric pressure. If one examines the equation, it can be ascertained, that the maximum value of the density can be reached at $p \to \infty$, equaling to $1,34 \cdot \rho_0$, also illustrated in Figure 26.

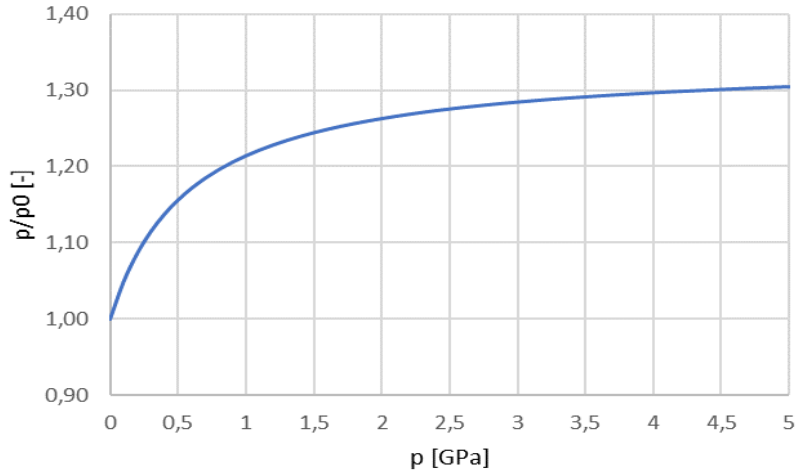

Figure 26 Pressure dependency of density

4.5 CONTACT PRESSURE DETERMINATION

In journal bearings of IC engines under adverse conditions mixed or boundary lubrication regime may occur, which features direct contact between surfaces of moving parts. In these cases, the load acting on the bearing is partially or fully carried by contacts of asperities. For determination of the contact pressure several approaches exist, for example the theory of Hertz or Greenwood and Tripp. These well-known theories, however, only consider elastic deformations.

4.5.1 HERTZ'S CONTACT THEORY

In 1881 Heinrich Hertz published his theory and formulae for the determination of contact stress. Hertzian contact stress is derived from the analytical equations of elasticity. It gives the contact pressure as a function of the normal contact force, the radii of curvature of both bodies and the Young's modulus of bodies in contact. Hertz's theory assumes, that the materials of the solids in contact are homogeneous, the contact stress is only caused by the normal force, the contact area is very small in comparison with the dimensions of the contacting bodies, the surface roughness is negligible and the entities are at rest and equilibrium [15].
Formulae for the maximal and the average contact pressure are given in the following equations [15]:

$$p_{\max} = \frac{3W}{2\pi a^2}, \tag{18}$$

$$p_{average} = \frac{W}{\pi a^2}, \tag{19}$$

$$a = \left(\frac{3WR'}{E'}\right)^{1/3}, \tag{20}$$

$$\frac{1}{R'} = 2\left(\frac{1}{R_A} + \frac{1}{R_B}\right), \tag{21}$$

where W is a normal contact force [N], E' is the combined modulus of elasticity [Pa], R' is the reduced radius of curvature [m], R_A and R_B are the radii of the spheres respectively and a represents the radius of the contact area [m].

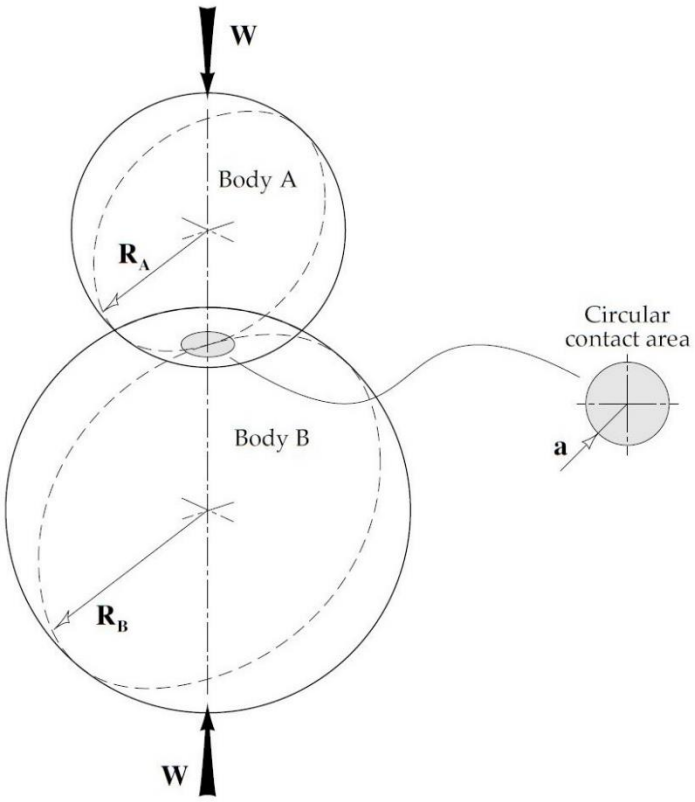

Figure 27 Geometry of the contact between two spheres[15]

4.5.2 CONTACT MODEL BY GREENWOOD AND TRIPP

The approach for the determination of the contact pressure was published by J. A. Greenwood and J. H. Tripp in 1970. The equation for contact pressure between two rough surfaces developed by them is formulated as follows [7]:

$$p_c(h) = \frac{8\pi}{5}(\eta_r \beta \sigma) K F_{5/2}\left(\frac{h}{\sigma}\right), \tag{22}$$

$$K = \frac{2\sqrt{2}}{3}(\eta_r \beta \sigma) E' \sqrt{\frac{\sigma}{\beta}}, \tag{23}$$

$$\frac{1}{E'} = \frac{1-\nu_1^2}{E_1} + \frac{1-\nu_2^2}{E_2}, \tag{24}$$

where η_r is the surface density of roughness peaks, β is the average radius of curvature of rough surface asperities, $\nu_{1(2)}$ is the Poisson's constant, E' is the combined Young's modulus, $E_{1(2)}$ is the Young's modulus for each material of the contact pair and $F_{5/2}$ is the function of contact pressure increase. σ is the combined RMS of both surfaces and is defined above in equation (6). The dependence of the $F_{5/2}$ function on the h/σ ratio is given in a table in the article [7].

4.6 Force Equilibrium Equation

For steady state conditions the integral of the pressures over the observed area S must be equal to the carried load [17]:

$$W = \iint_S p(x,y)\,dxdy\,. \tag{25}$$

4.7 Slide Bearing Dynamics

In computation of slide bearing models a key role is played by the bearing dynamics. The dynamics of journal bearings are a highly complex physical problem, which is almost impossible to solve with basic mathematic formulae. For this reason, for the solution of bearing dynamics several software tools were developed. For the slide bearing analysis within the frame of this master's thesis the FEV Virtual Engine is used.

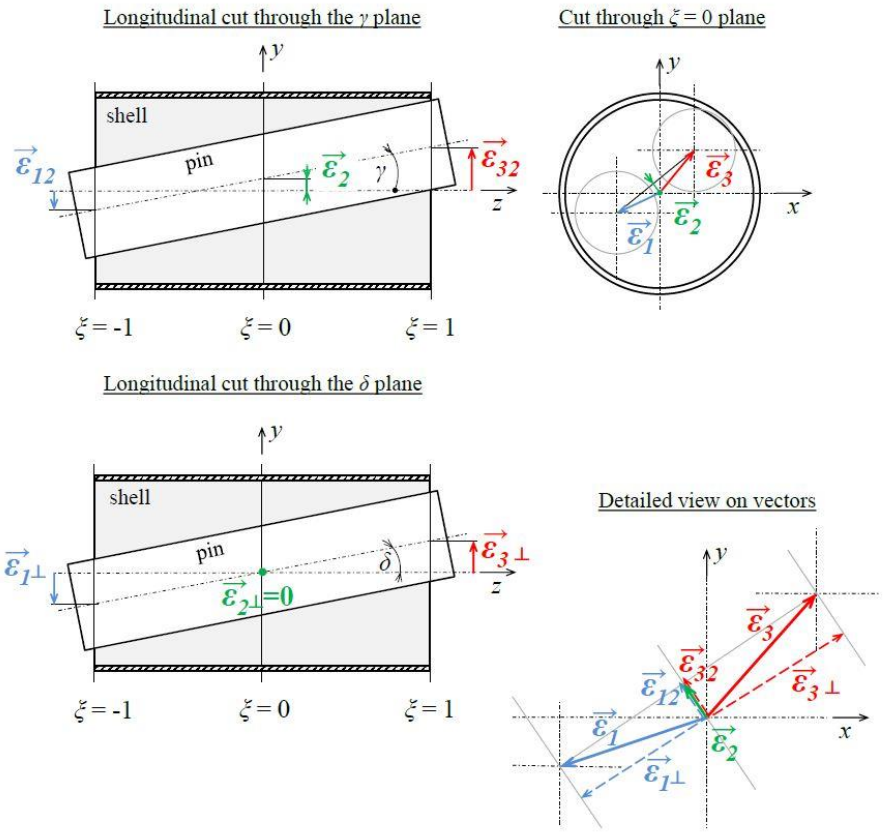

Figure 28 Bearing pin tilting [9]

For the bearing pin tilting, one of the most precise approaches describing this behavior is the Voncken-Maršálek [9] approach published in 2015. The Voncken-Maršálek approach is based on the approach of Novotný [10] published in 2004. This approach was developed for oil film gap investigation for hydrodynamic database generator for FEV Virtual Engine [9]. The Voncken-Maršálek approach considers realistic states of bearing pin tilting in two tilting planes shown in Figure 28: the plane of the narrowest oil film gap and the plane perpendicular to the mentioned one.

5 PREPARING THE CRANKTRAIN MODEL FOR THE BEARING ANALYSIS

The bearing analysis was provided with the FEV Virtual Engine software tool. The newest release of the VE, supplemented by a detailed EHD bearing module, allows an inclusion of real surface data in the simulation. The simplified cranktrain model was built up from the basics thru the following steps:

- creating a template,
- creating and customizing a subsystem,
- scanning the real bearing surface samples,
- setting up the EHD bearings and
- creating an assembly.

FEV Virtual Engine basically has two main interfaces: The Standard Interface and the Template Builder. The Standard Interface serves to adjust and analyze models, while the Template Builder is used for creating new templates with a unique topology for further analyses. In our case the simulations are focused on the main and one of the pin bearings, hence the cranktrain model contains only the main components of the cranktrain, like the pistons, connecting rods, crankshaft, torsional damper, flywheel and the engine block.

5.1 CREATING A TEMPLATE

The creation of the simulation model was carried out by following the recommendations written in the VE manual. Hence, the process flow of the building begins with the creation of the cranktrain template. The cranktrain template captures communicators, elements, parameter variables and the topological data of the cranktrain for the later subsystem.

5.1.1 COMMUNICATORS

Communicators are key elements that ensures the exchange of information between subsystems, templates and the testrig in the assembly. There are two types of communicators, enabling the two-direction data transfer: input and output communicators. An input communicator requests information from testrigs or other subsystems, while an input communicator can receive data only from one output communicator. An output communicator provides information to testrigs or other subsystems, whereby it can send data to multiple input communicators.

5.1.2 ENGINE GLOBAL DATASET

In the next step, it is necessary to define the engine global dataset. This contains the main parameters of the built engine model, such as the number of banks and cylinders, stroke, bore

diameter, but also the bank, cylinder and crank layout. In this dataset the axial cylinder distance, effective length of the connecting rods and the dimensions of the piston pin are also defined. The engine global dataset can be modified later in the Standard Interface with a reduced range of options. For the slide bearing analyses an inline three-cylinder spark ignition engine was modelled with basic parameters listed in Table 1.

Table 1 Parameters of the modelled engine

Engine Type	**Škoda 1.0 MPI**
Configuration	Inline 3
Valvetrain	DOHC 12V
Displacement	999 cm^3
Bore	74.5 mm
Stroke	76.4 mm
Axial Cylinder Distance	83 mm
Main Bearing Diameter	42 mm
Main Bearing Width	17 mm
Pin Bearing Diameter	42 mm
Pin Bearing Width	16.2 mm

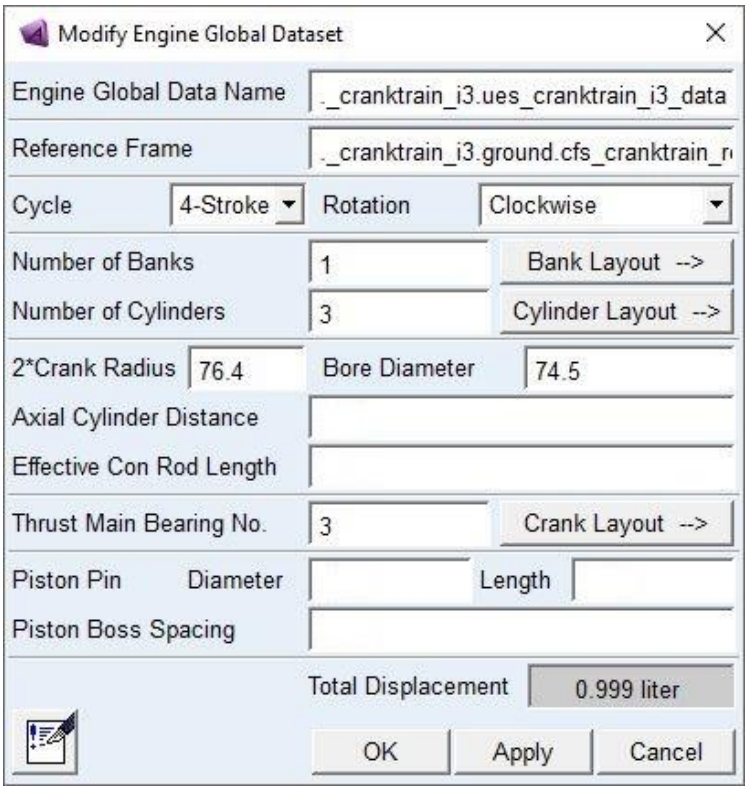

Figure 29 Engine Global Dataset dialog box

5.1.3 CRANKTRAIN PARTS

The engine parts in VE Template Builder Interface can be created in two ways: manually or by using the Cranktrain Wizard. The creators of VE recommend the building of the cranktrain template at least once manually, to understand the attachments and the function of the components. Running the Cranktrain Wizard VE generates the parts chosen by the user and all necessary attachments and construction frames automatically.
If one later wants to replace the crankshaft with a flexible one, at this point it is important to set the correct number of the shaft sections in the Cranktrain Wizard dialog box. VE places attachment points in each shaft section, which later must match the interface nodes in the FEM model. The process of replacement is described thereinafter. The final template in this work was created with the Cranktrain Wizard.

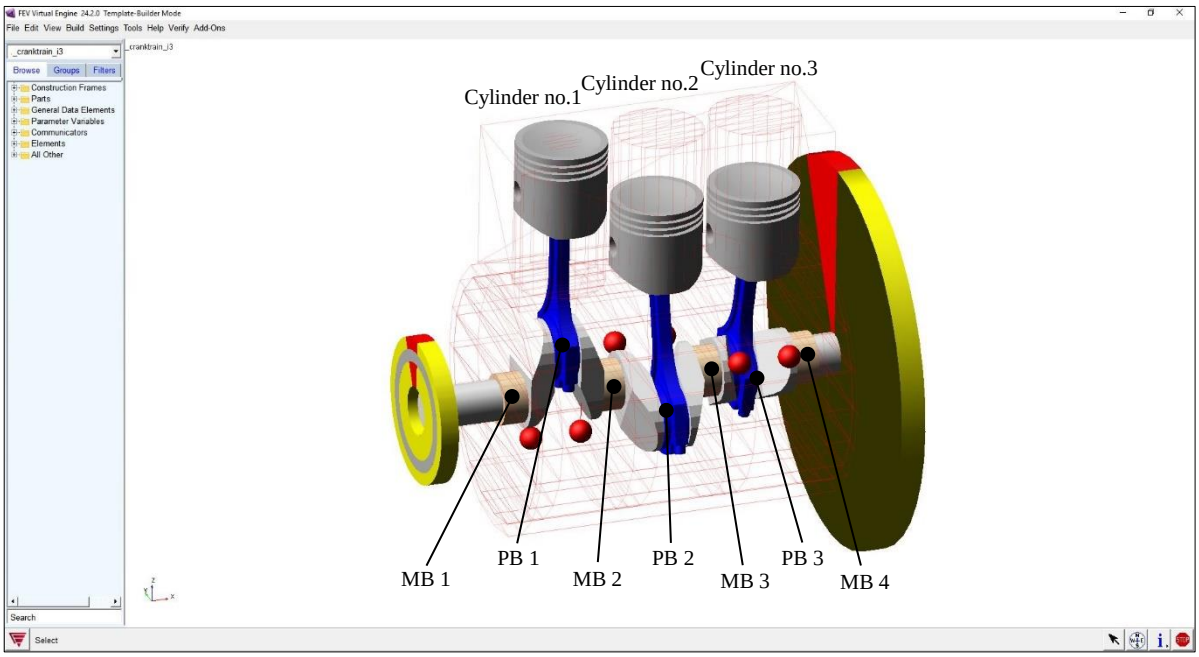

Figure 30 View of the template with visualized bearings' and cylinders' layout at 0° crank angle position

5.2 CUSTOMIZING A SUBSYSTEM

Subsystems are the central components of the VE modelling structure. They are based on templates, which define the topology and default data for the subsystem. In subsystems the user can edit the respective parameters for the parts and environment elements. At this point the model contains only rigid parts.

5.2.1 PARTS

Since in the engine model only the main and one of the pin bearings will be analyzed, the engine parts connecting to these bearings must be replaced by flexible ones. These are the connecting rod of cylinder number 1, crankshaft and the engine block. The reason for replacing only one pin bearing with EHD bearing is time effectivity. Adding one EHD pin bearing multiplies the

time needed for the calculation. The other engine parts remain rigid with modified inertia properties acquired from the CAD data.

Replacement of the rigid parts

For the replacement of the selected rigid elements by flexible ones is necessary to reduce the CAD models into FE models, run a modal reduction and generate a modal neutral file (*.mnf), which is the only way to import flexible bodies in VE. For this purpose, these files were provided by Škoda Auto for the further simulations.
The created modal neutral file must be equipped with interface nodes at the same positions where the attachment markers are placed in the model. Interface nodes are load distributing elements (RBE3 elements in MSC Nastran), which are an art of interpolation constraint element, which transfer loads to a single node [29].
Another notable aspect is the correct orientation and positioning of the model prepared for importing. The standard orientation in VE compared to the global coordinate system is rotated by 90 degrees around each axis. Thus, the *x* axis points upwards (in opposite direction of gravity), the *y* axis points to the engine sides and the *z* axis is the axis of rotation and points to the flywheel.

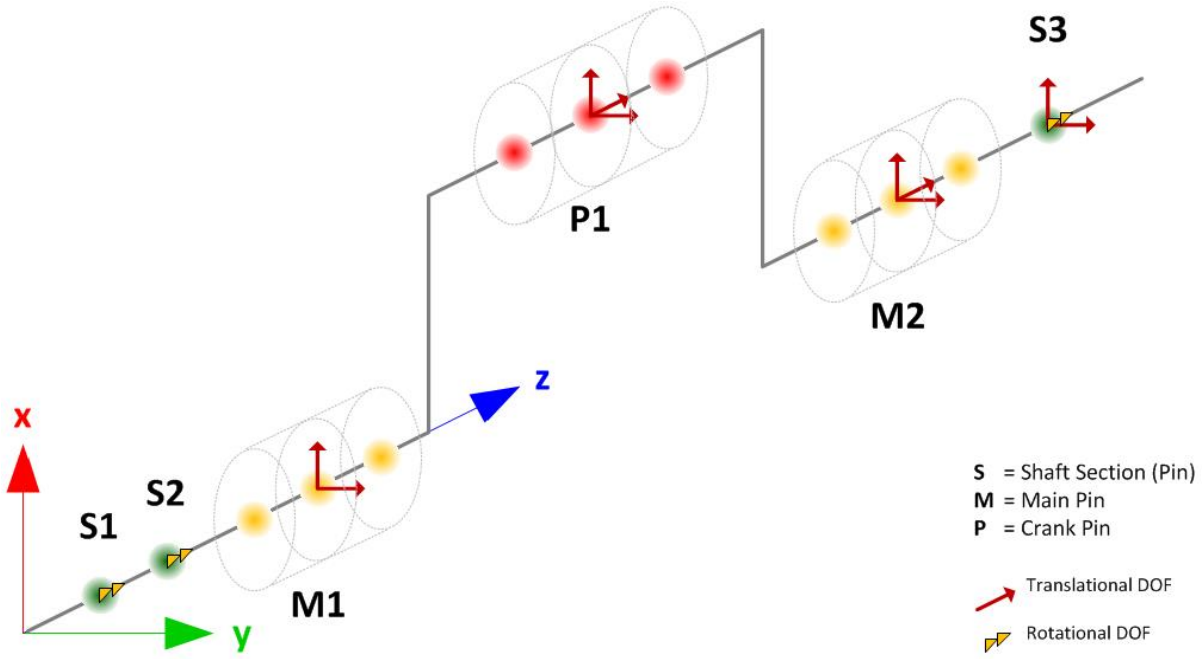

Figure 31 Standard orientation of the crankshaft with visible attachment nodes and DOFs of bearings and shaft sections [29]

For the correct replacement of the crankshaft's shaft sections and bearings, prepared for further analysis using HD or EHD bearing models, the model must contain [29]:

- at least three nodes equidistantly placed along the *z* axis for each main bearing,
- at least three nodes equidistantly placed along the mid axis of the pin bearing,
- one node placed along the *z* axis for each shaft section,
- the node in the middle of each bearing must support at least one translational DOF in directions of the axes *x* and *y*,
- the middle node of the thrust bearing must support a translational DOF in the *z* direction too,
- the nodes of the shaft sections must support at least one rotational DOF,
- the shaft section connecting to the flywheel must also support translational DOF in directions *x* and *y*.

As mentioned therefore, the correct number of the shaft sections must be set in the engine template, because at this point VE attaches the FE model to the part connection locations. The FE model of the crankshaft used in this work contains five attachment nodes in the main bearing journals and five attachment nodes in the pin bearing of the first cylinder. The pin bearings of the second and third cylinder will not be replaced by EHD bearings, hence, one attachment node is sufficient in these bearings.

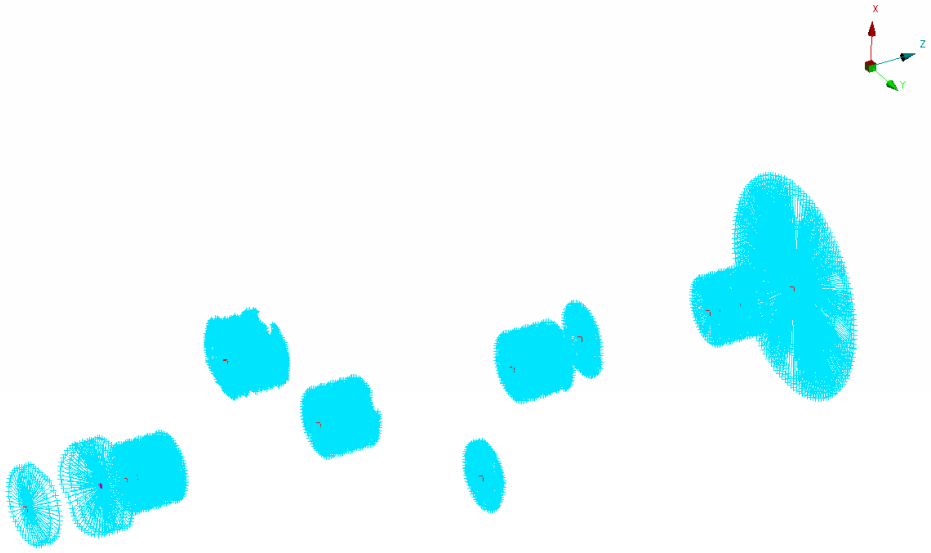

Figure 32 Attachment nodes placed on the FE model of the crankshaft

To check the correct connection of flexible body with VE model, one can generate a pre-report before the replacement. If the points are not placed at the exact same position, VE generates a

massless dummy part between these points, which ensures the proper usage of the crankshaft, but can lead to inaccuracies or biased results of simulations.

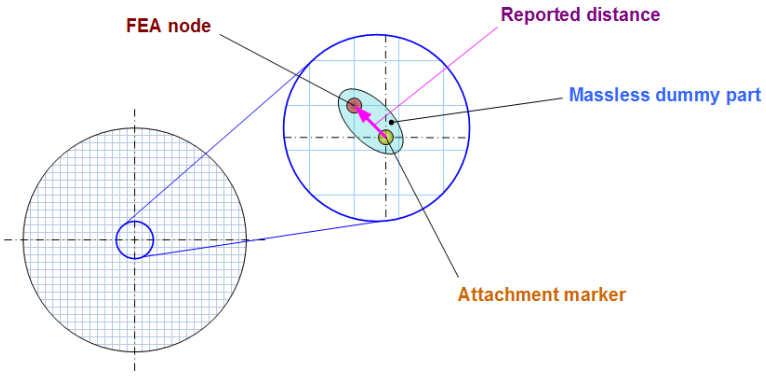

Figure 33 Connection of attachment points by dummy part [29]

In the case of engine block for the proper replacement RBE3 elements should be placed for each bearing, gas force and piston-liner connector. In Figure 34 are shown the placed attachment elements in FE model used for simulations.

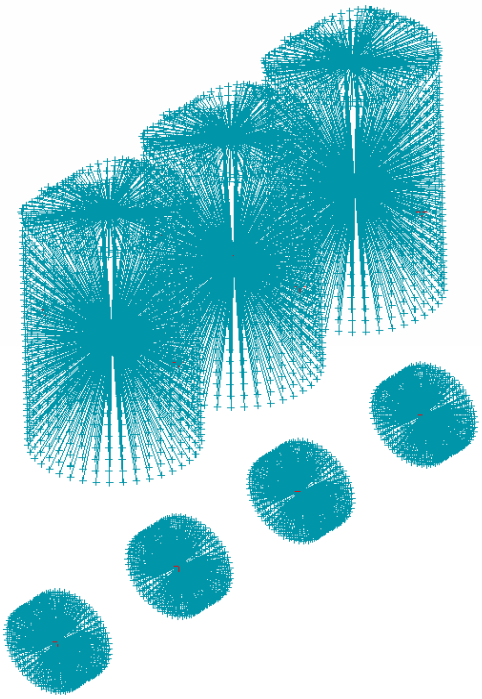

Figure 34 Positioning of attachment elements in the engine block

It is also important, that the FE model contains twelve nodes distributed in three planes for each bearing, as shown in Figure 35.

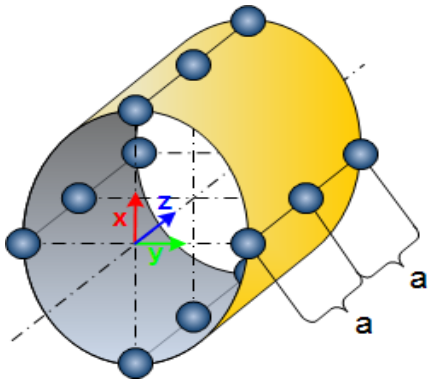

Figure 35 Distribution of nodes on the main bearing of the engine block [29]

Details of the FE models

Before reducing the CAD models to FE models for further bearing analyses, one must be aware of the fact, that VE evaluates the bearing results on the bearing shells. Therefore, the models used only for bearing analysis can be meshed with relatively coarse structure, with increased density of the mesh on the bearing shells.
The FE models were generated using the pre-processor software tool ANSA. The main components of the engine model parts (connecting rod, crankshaft and engine block) were meshed with unstructured tetrahedral elements and the bearing shell parts of pin and main bearings with structured hexahedral elements.
The FE model of the engine block, used for simulations, contains, besides the crankcase, the cylinder head, cylinder head cover and oil pan, as shown in Figure 37.

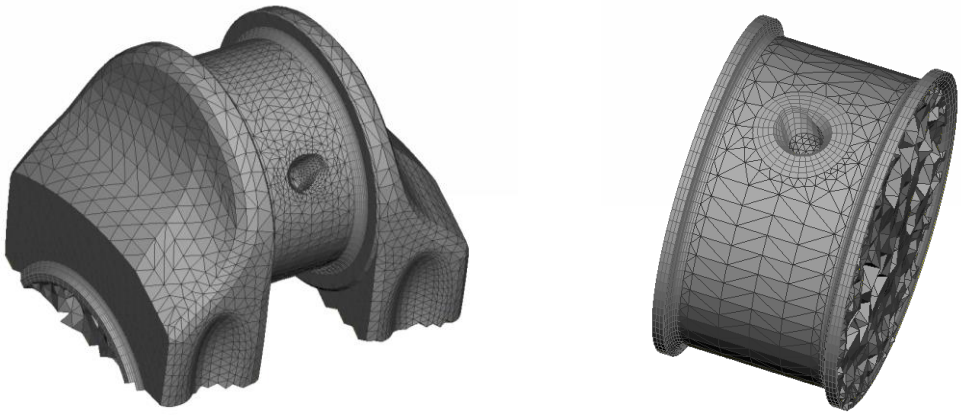

Figure 36 Pin and main bearing journals

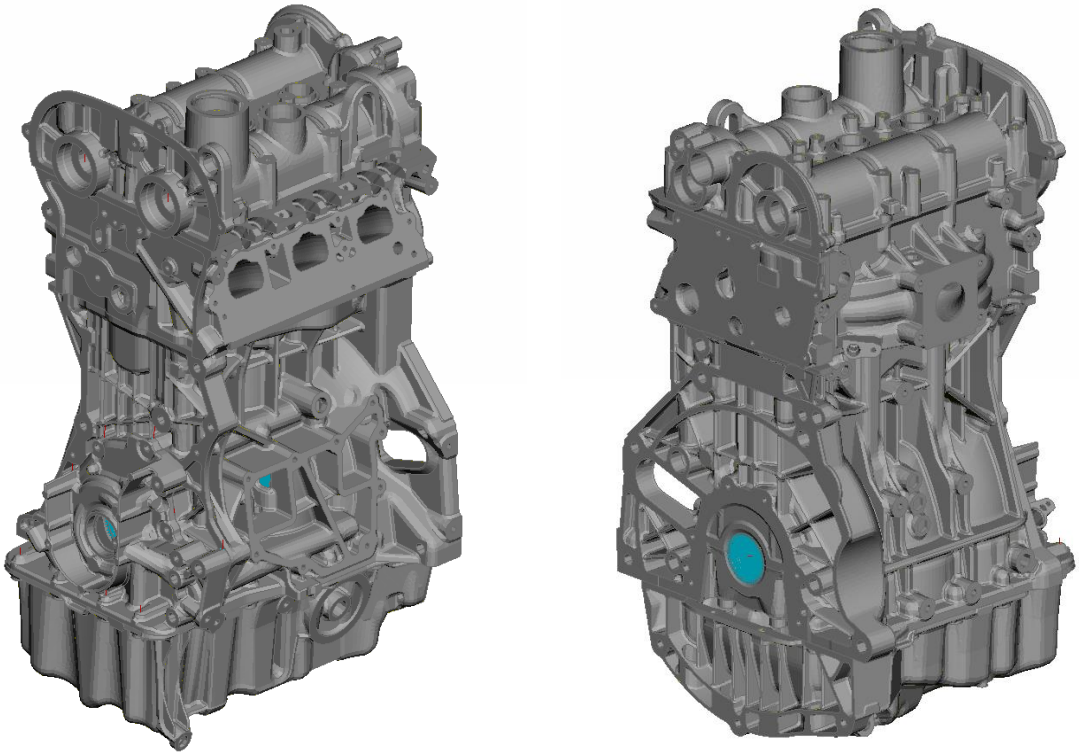

Figure 37 Front and back view of the engine block's FE model

The main bearing shells' mesh contains 528 grid points and these are organized to match the oil supply groove in the middle, as shown in Figure 38.

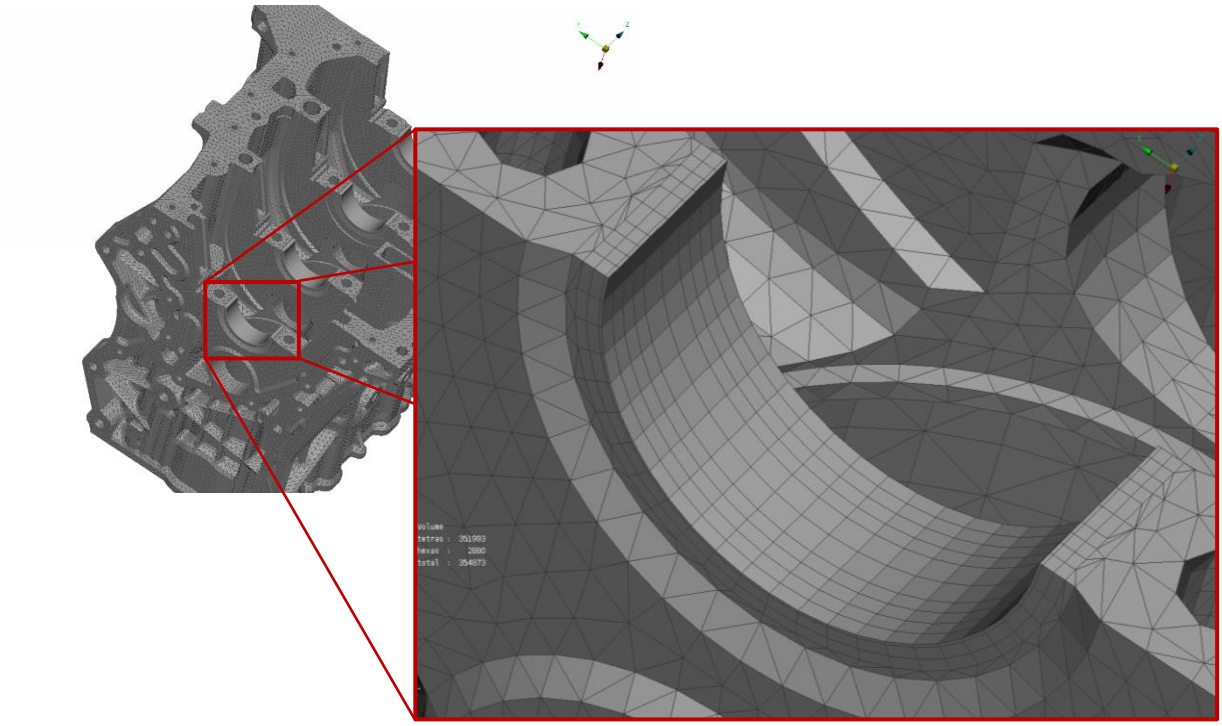

Figure 38 Detailed view of the main bearing shell's mesh

In Figure 38, Figure 39 and Figure 40 can be seen, that the bearing shells are divided into three layers, where the innermost layer represents the running layer and the material properties are set for them correspondingly.
The amount of the grid points of the main and pin bearing shells was set after consultations with experienced engineers at Škoda Auto, while a reliable computational time was a crucial aspect. For the pin bearing shell was set a mesh containing 936 grid points.

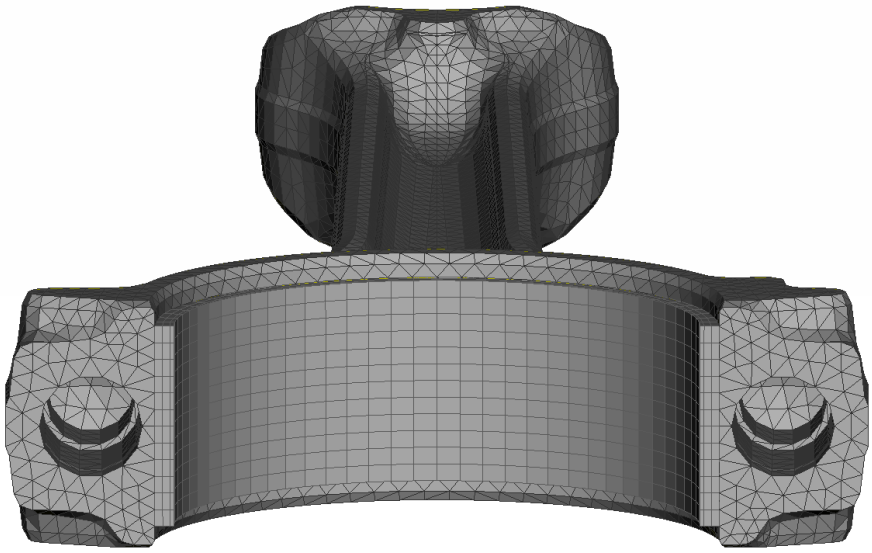

Figure 39 FE model of the connecting rod

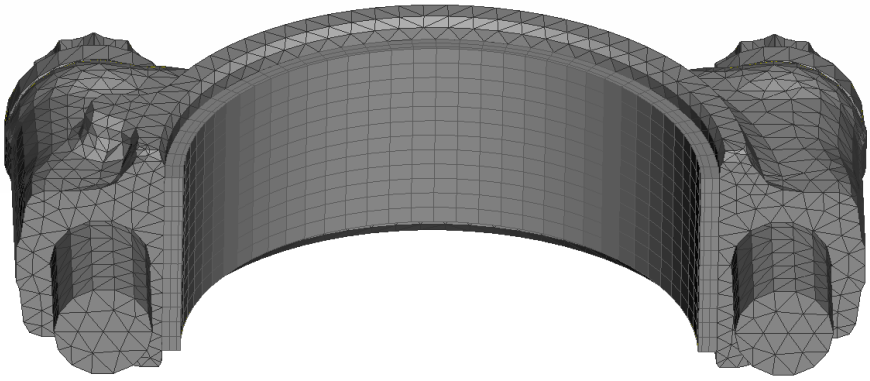

Figure 40 Connecting rod cap's FE model

5.2.2 ENVIRONMENT ELEMENTS

Using environment elements, the user can define several conditions at certain points of the system based on measurements or other simulations. The types of environment elements are: viscosity, pressure and temperature.

Gas force element
The resulting forces of the combustion process are represented by this element. These are stored in a property file depending on the crank angle for a range from 1000 to 6500 rpm for each cylinder separately.

Temperature element
As known, the temperature varies at the certain points of the engine depending on engine speed and load. With this variable the temperature is defined in the bearings and has an influence on the oil viscosity.

Pressure elements
In this work two pressure elements are placed, the oil supply pressures in main bearings and pin bearing. The oil supply pressure in the main bearings is map controlled by the engine control unit depending on the engine speed and load.
The oil supply of pin bearings is ensured by diagonal drillings in the crankshaft. These drillings run from the main bearing to the crankpins through the crankshaft web. The overlapping of the drilling at the main bearing pin with the oil supply groove on the main bearing shell ensures the oil flow. While the cranktrain rotates, the centrifugal force caused by the oil column in the drilling, raises the oil supply pressure at the pin bearing. When the drilling is not overlapped with the groove, the supply pressure is created only by the rest of the oil in the drilling. This variation of the supply pressure at the pin bearing must be defined in the model. Hence there is no prepared macro in the VE for the definition of the pressure depending on the crank angle and engine speed, it is necessary to create one. The pressure data was generated in prepared table in Microsoft Excel. This data was stored in a 3D spline in VE and defined as a state variable.

Oil viscosity element
This variable contains the dynamic viscosity properties of the specific oil depending on the temperature. In this work oil with SAE viscosity grade 0W20 was used.

All input data used in this work were gained by measurements provided by Škoda Auto.

5.2.3 EHD BEARING SETUP

At this point the existing constraint bearings are replaced by EHD bearings. Virtual Engine allows a complex definition of bearing design parameters for further analyses in EHD bearing model. Besides standard bearing dimensions the following parameters can be defined by user in this model:

- shell contour,
- journal contour,
- oil supply groove measurements,

- crush relief measurements and
- rough surface data.

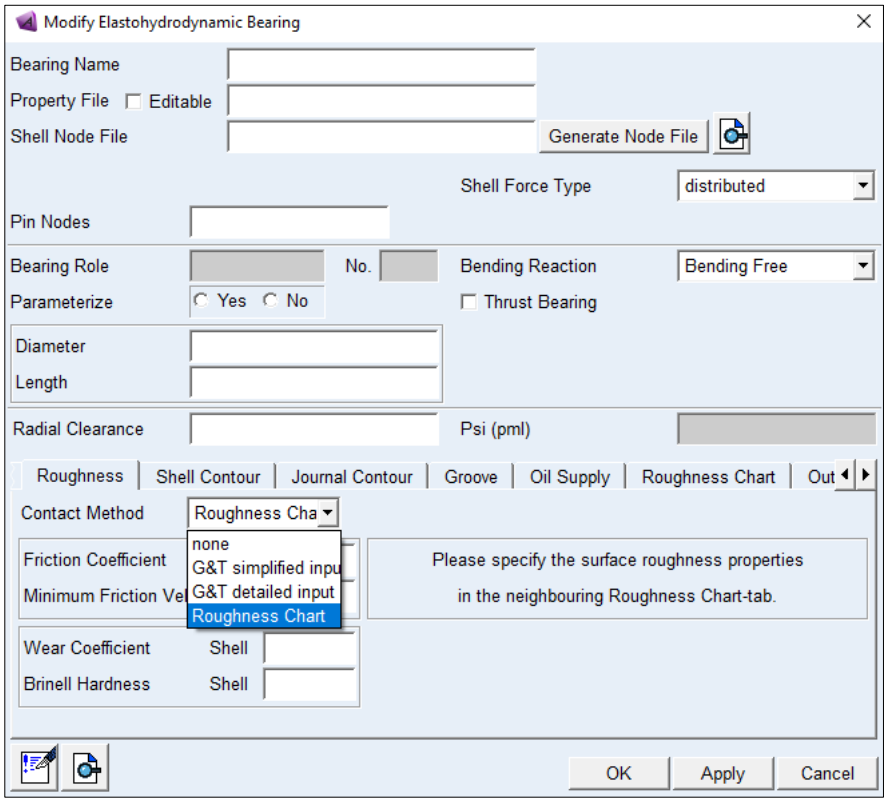

Figure 41 EHD bearing dialog box

As shown in Figure 41 for the adjustment of each above-mentioned parameter one tab in this dialog box serves. Shell and journal contour must be defined externally in property files. These must contain the radial offset values that will be applied to the shell or the journal in dependence of angular and axial position. The parameters set here were obtained from technical drawings of the crankshaft and bearing shells provided by Škoda Auto.
In tab roughness chart, one can set roughness data gained by measurements of real bearing surfaces. In the next chapter the process flow of surface profile measurement and further data preparation for the involvement in this model is described.

5.3 SURFACE PROFILE MEASUREMENT

The surface roughness measurement was carried out on an optical profilometer Contour GT-X from an American manufacturer BRUKER. This fully automated precise microscope uses white light interferometry to provide a complete 3D surface profile of the scanned sample. The basic data of the profilometer are listed in Appendix A.
For the measurements samples of unworn bearing journals of three crankshafts and bearing shells of three different designs were supplied by Škoda Auto. Four samples of each crankshaft

and two sample bearing shells of each design were measured. All shell and journal samples have been scanned at three different spots. Each scanned area measures 0.2352 × 0.2352 mm.

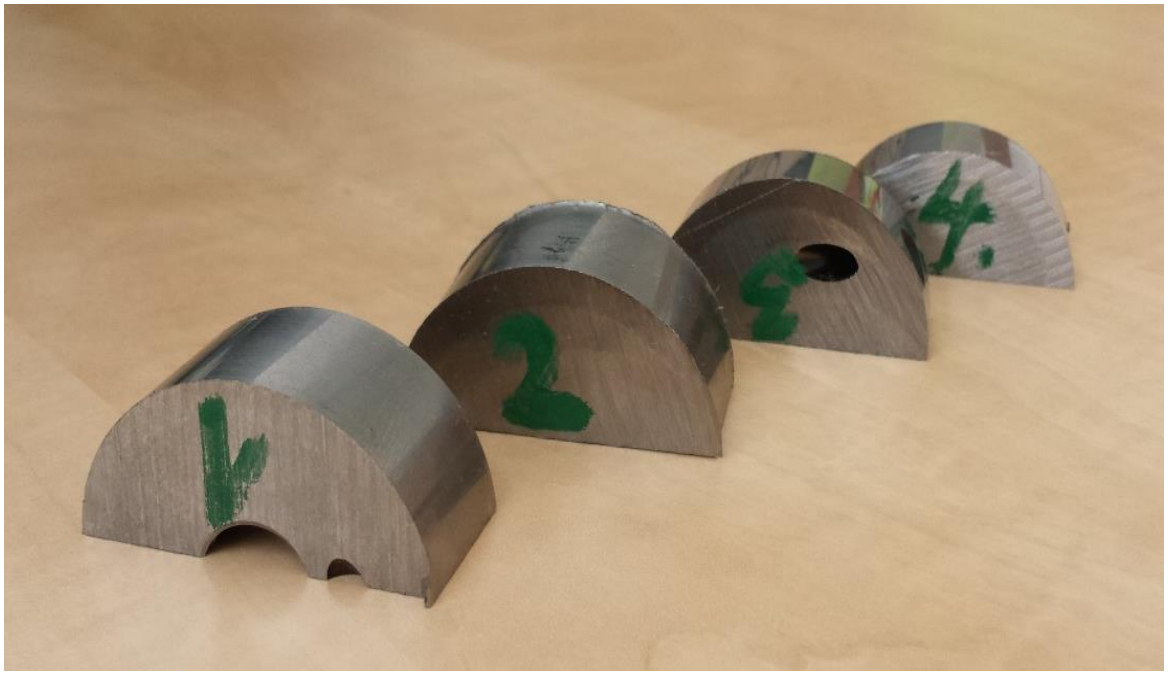

Figure 42 Samples of crankshaft bearing journals

Figure 43 Bearing shells prepared for the measurements

The output data files of the scanning process contain matrices each with 480 × 480 cells, where the asperity height values measured from the mean plane are stored. Sample images of a scanned bearing journal, pin bearing shell, main bearing shell with and without polymer coating are shown in Figure 44, Figure 45, Figure 46 and Figure 47, respectively.

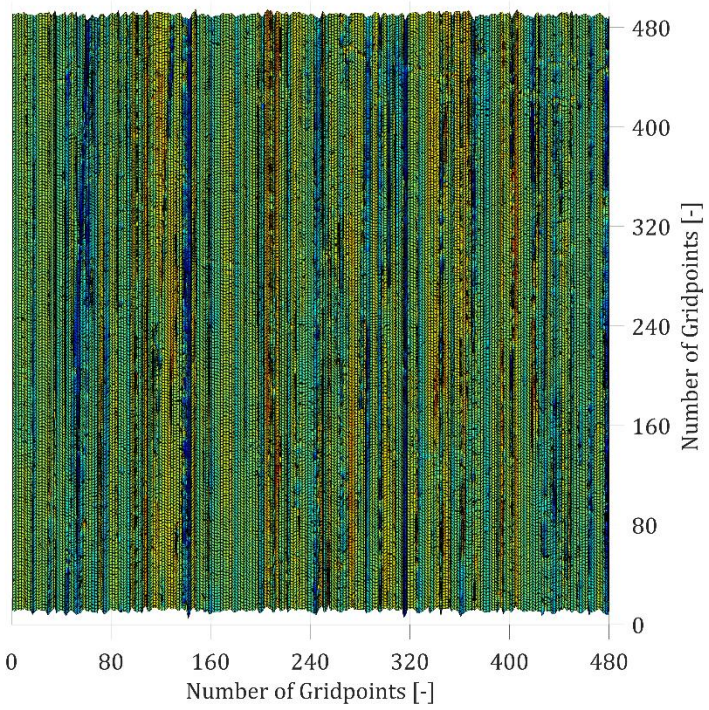

Figure 44 Surface topography of main bearing journal

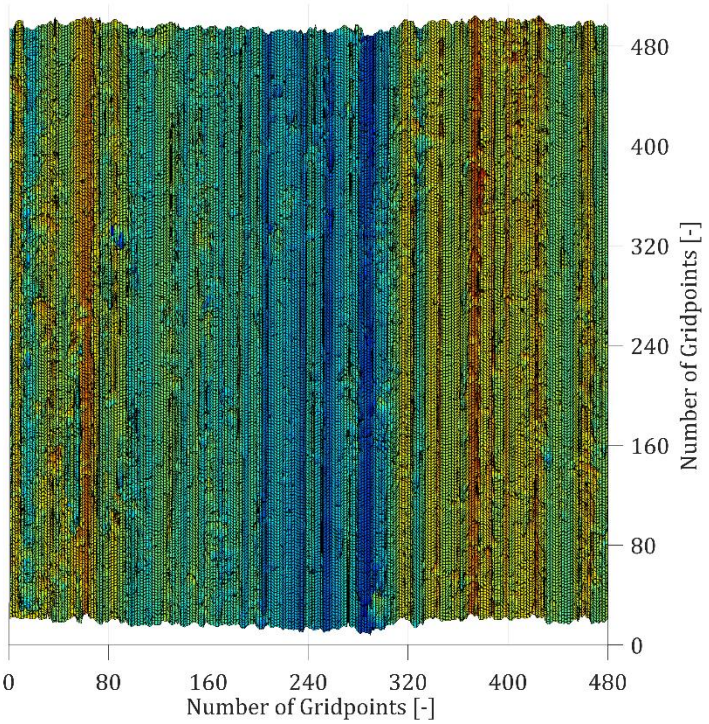

Figure 45 Surface topography of pin bearing shell

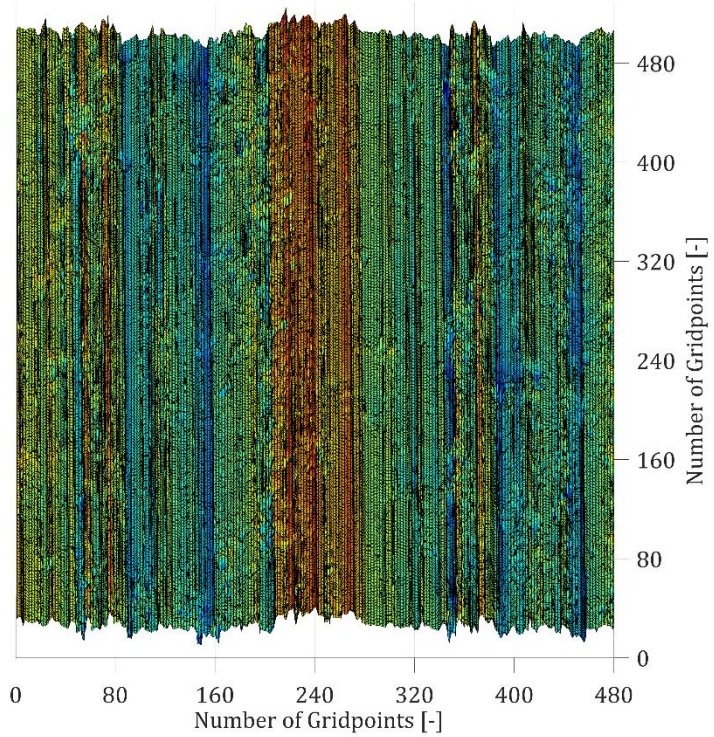

Figure 46 Surface topography of main bearing shell

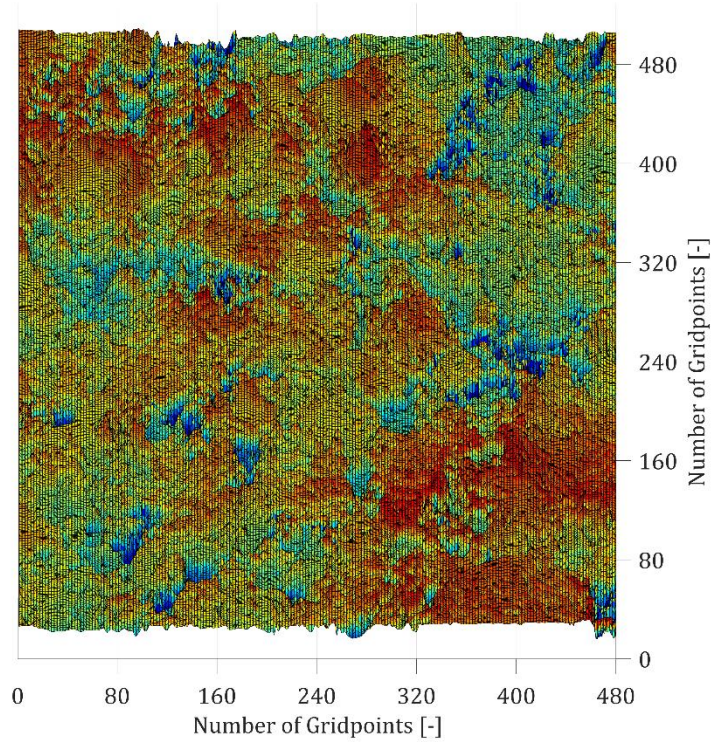

Figure 47 Surface topography of polymer coated main bearing shell

The scanning of part samples was followed by analyzing the gathered information and selecting the proper samples for inclusion in simulations.
After listing and comparing the root mean square values of asperity heights of the measured areas it could be ascertained that the average roughness of two crankshafts of three are practically equal (difference below 4%). Therefore, for the bearing analyses surfaces of the "best" (crankshaft no. 1) and the "worst" (crankshaft no. 2) crankshafts were chosen. The difference between the RMS roughness values of these is over 17%. However, all samples fulfill the quality criteria of the manufacturer.

5.4 GENERATING THE INPUT FILES

The inclusion of the impact of surface roughness into the hydrodynamics is realized by a specific roughness-chart-file (*.ffa). This file is generated by Virtual Engine by using the Flow Factor Calculation add-on. In addition to the files providing the surface topology, for the flow factor calculation process the user must specify the dynamic viscosity of the lubricant, shear velocity (tangential velocity of the bearing), ambient pressure and the material properties of the bearing journal and shell, respectively. Furthermore, the user can decide between three approaches for the contact pressure calculation. In this work, the contact theory of Greenwood and Tripp was utilized.

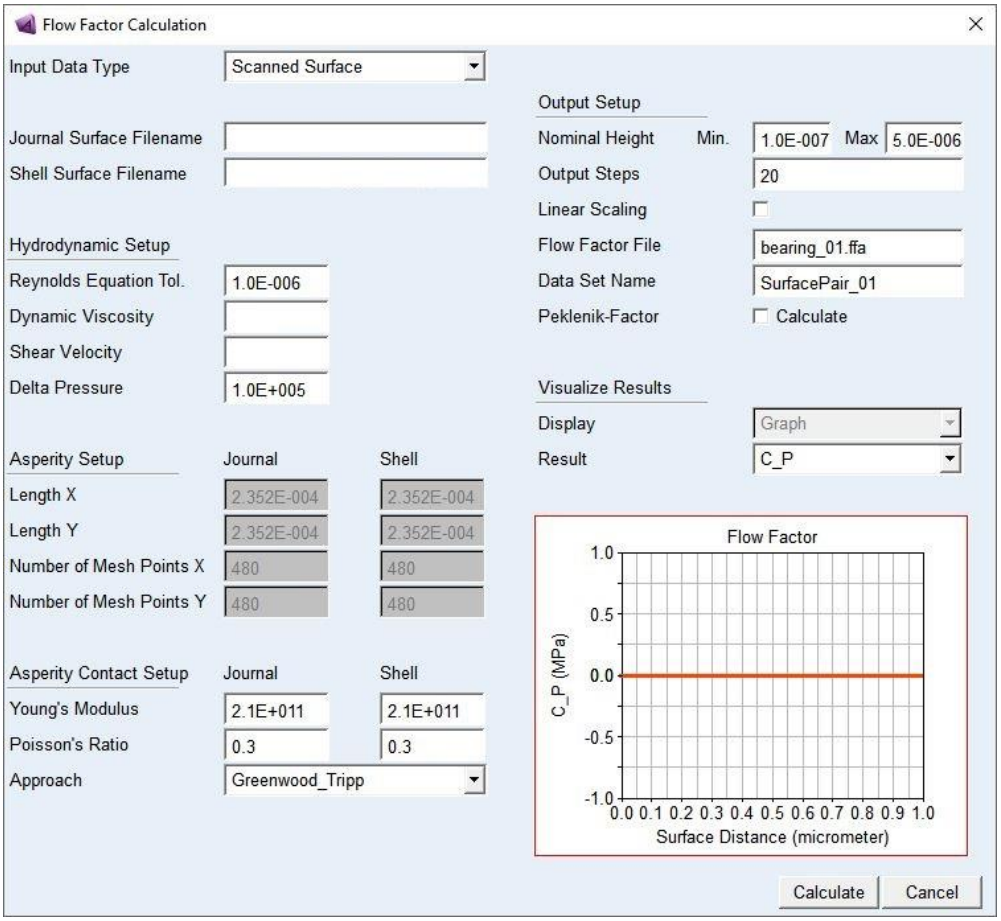

Figure 48 GUI of the Flow Factor Calculation add-on

To gain a more accurate result, which suitably characterizes the chosen bearing and journal pair, the values of flow factors and contact pressure have been generated for nine pair of sampled spots. Thereafter, these have been averaged, and as an example their charts for the pair of the first main bearing journal of crankshaft no. 1 and main bearing shell are shown in Figure 49, Figure 50, Figure 51 and Figure 52, respectively.

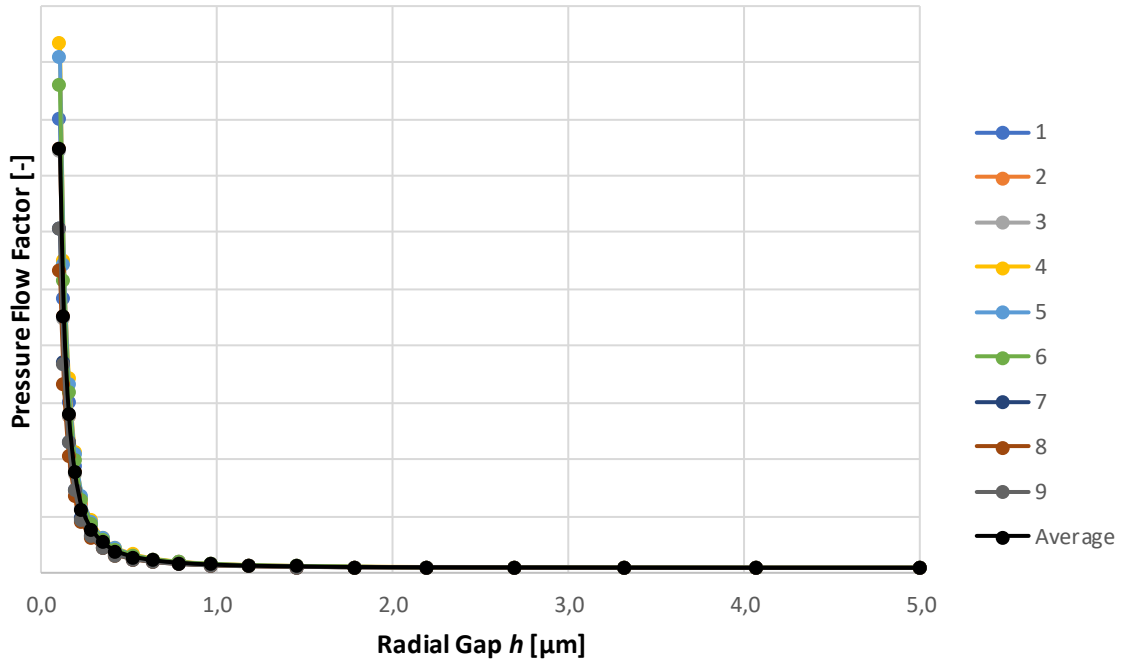

Figure 49 Pressure Flow Factor in tangential direction

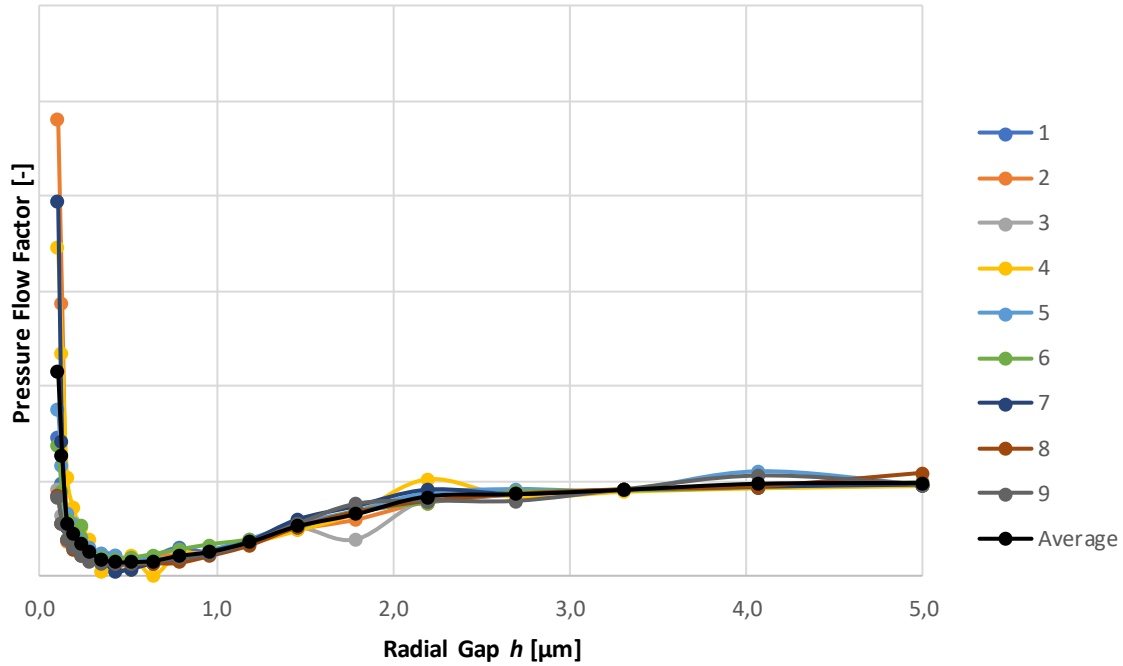

Figure 50 Pressure Flow Factor in axial direction

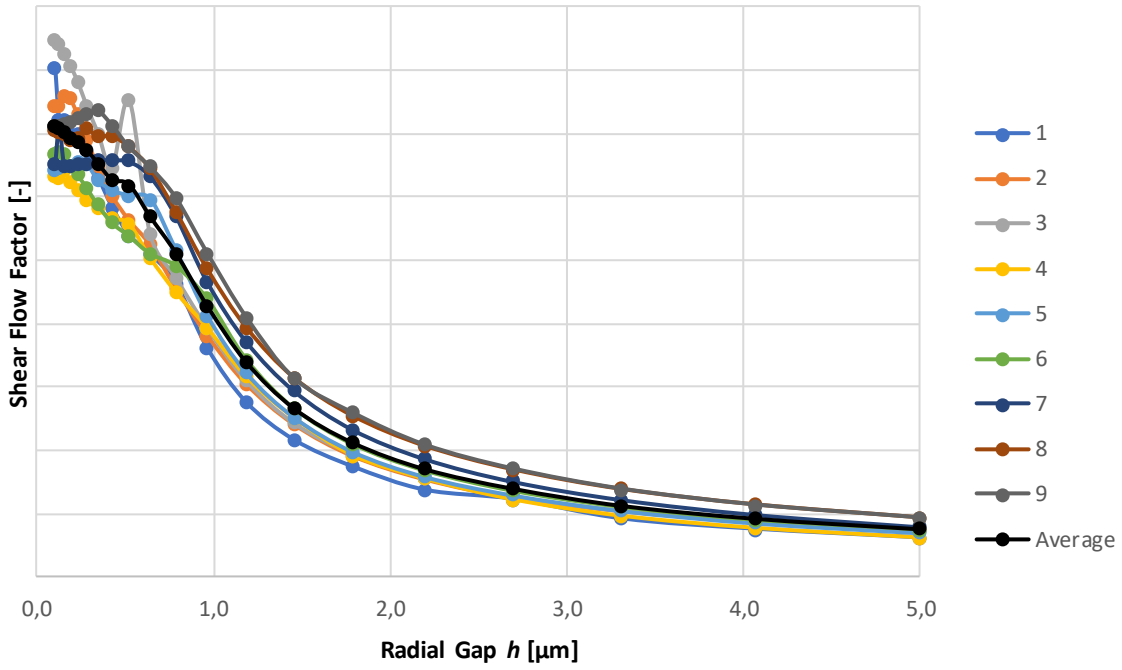

Figure 51 Shear Flow Factor

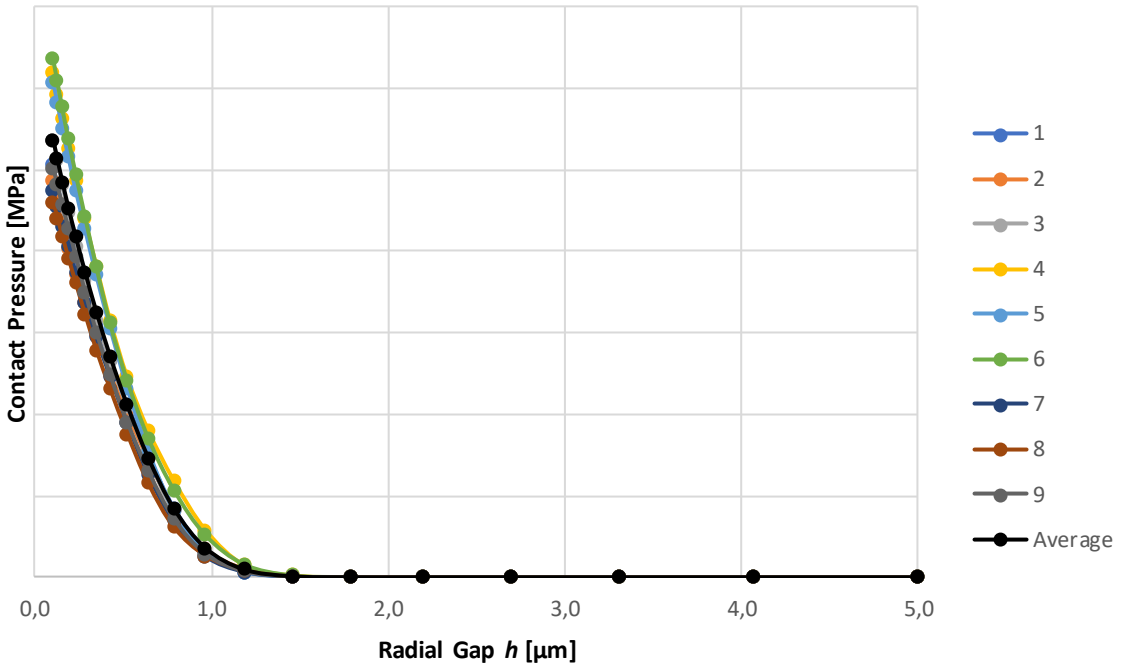

Figure 52 Contact Pressure

By applying these parameters to all five EHD bearings defined in the model, the cranktrain subsystem is set completely.

5.5 CREATING A CRANKTRAIN ASSEMBLY

Running a steady-state analysis in MBS software tool Virtual Engine is only allowed on assemblies. Assemblies represent a collection of subsystems with a test rig. An assembly must be created even then, when there is only one subsystem included, because the assembly connects the subsystem with the test rig. A test rig applies, among others the engine speed to the cranktrain [29].

5.6 SETTING UP THE ANALYSES

Steady-state analyses were provided in four operating points (OP) to match a few critic and regular conditions of the engine working cycle. These operating points are as follows:

- 2000 rpm, full load (OP 1),
- 2200 rpm, 2.75 bar IMEP (OP 2),
- 6500 rpm, full load (OP 3),
- 6500 rpm, without load (OP 4).

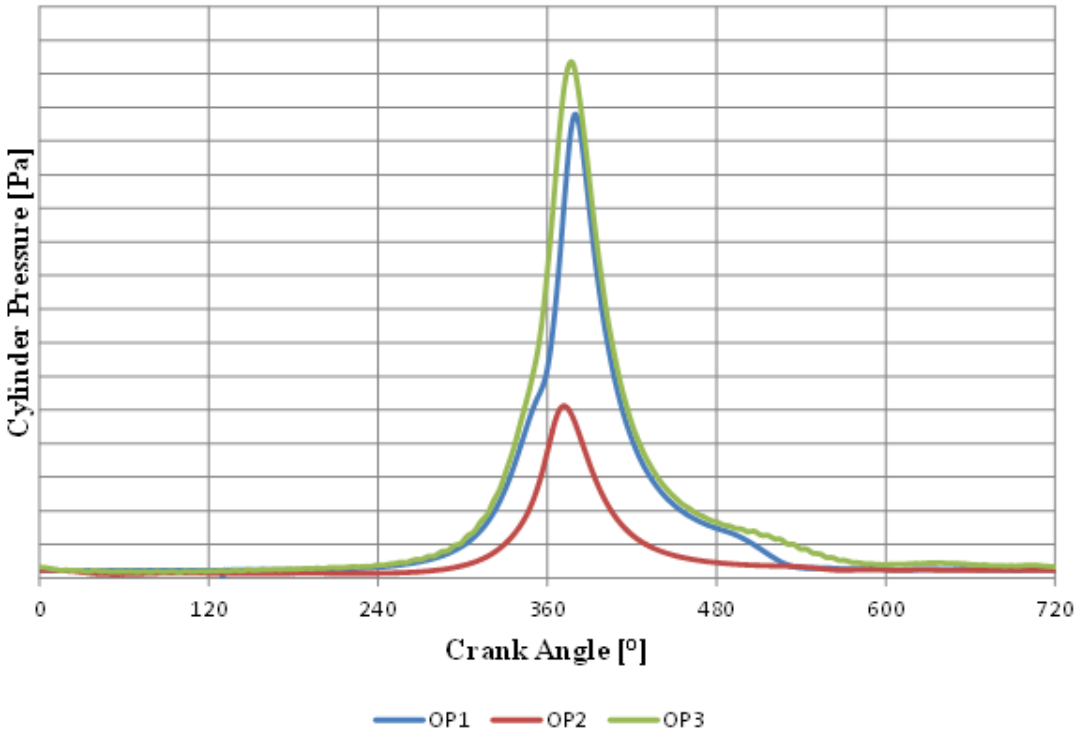

Figure 53 Cylinder pressure curves of analysed operating points

All four simulations were performed once with roughness properties of the crankshaft no. 1 and once with the properties of the crankshaft no. 2. Only the surface profiles of the bearing pins were replaced. The bearing shell parameters are the same for all simulations to ensure a proper comparability.

According to recommendations of the creators of VE about solver settings to use with the EHD bearing model, for the analyses the settings listed in Table 2 were set.

Table 2 Solver and analyes settings

Integrator	**HHT**
Error Tolerance	1×10^{-8}
Initial Step Size	1×10^{-8}
Maximum Iteration Step Size	5×10^{-6} (1×10^{-6}) *
Number of Simulated Steps	2880
Number of Cycles	2 (4 Revolutions)

*After running some trial simulations several biased values were in almost all result variables, that were compensated by decreasing the maximum step size value to 1×10^{-6}.

6 RESULTS OF THE ANALYSES

In the elasto-hydrodynamic bearing model of VE the Reynolds differential equation is solved iteratively at every time step for the present state of the bearing and the present boundary conditions. The output of the VE elasto-hydrodynamic bearing analysis consists of the following parameters [29]:

- axial displacement, velocity and forces (for thrust bearings only),
- eccentricity displacements in both radial direction,
- minimal gap,
- both radial forces,
- friction torque due to the hydrodynamic friction in the bearing,
- friction power loss due to the hydrodynamic friction in the bearing,
- friction torque due to the asperity contact friction in the bearing,
- friction power loss due to the asperity contact friction in the bearing,
- maximum oil film pressure,
- minimum oil film thickness,
- oil flow and
- velocities.

Within the framework of this master's thesis slide bearings were investigated in terms of tribology. Thus, the parameters, like hydrodynamic friction power, asperity contact power and the ratio of minimum oil film thickness (MOFT) to combined RMS (σ) were evaluated, and are visualized in Appendix B.

6.1 RESULTS AT OP 1

This operating point was chosen because of its low engine speed (2000RPM) and relatively high load. At this OP, the friction in journal bearings is not that high, however the contact friction on the main bearing no.1 (the furthest bearing from the flywheel) is considerably greater than on other bearings (shown in Figure 54). This end of the crankshaft can move more freely and is more influenced by the forces from cylinder no.1. This phenomenon could be eliminated by building a more complex model, including the clutch and the transmission. By building a model of that complexity would supply more realistic results, but several times longer calculation times. However, the model of the current grade of complexity is sufficient to match the goals of this work: to compare the difference of tribological characteristics of two crankshafts with different roughness profiles.
Unfortunately, the exact values of results are the confidential property of Škoda Auto, thus cannot be published. Therefore, the friction power loss on each bearing of CS2 (the "worse" crankshaft) is compared to the friction power loss of CS1 (the "better" crankshaft – taken as

baseline), and the results are shown as percental proportions from the baseline values, listed in Table 3.

Table 3 Friction power distribution on slide bearings at OP 1

	MB 1	MB 2	MB 3	MB 4	PB	All bearings
HD Friction Power CS1	100,00	100,00	100,00	100,00	100,00	100,00
HD Friction Power CS2	99,84	99,46	99,41	98,57	98,64	99,02
CT Friction Power CS1	100,00	100,00	100,00	100,00	100,00	100,00
CT Friction Power CS2	102,82	359,96	223,89	203,58	401,05	132,89
Total Friction Power CS1	100,00	100,00	100,00	100,00	100,00	100,00
Total Friction Power CS2	102,01	109,83	107,04	104,19	125,41	112,25

Therefore, can be concluded that the difference of surface roughness has almost no influence on the development of hydrodynamic friction, but the friction loss caused by asperity contact has increased by 32.89%, which results in a total increase of the friction power loss by 12.25%.

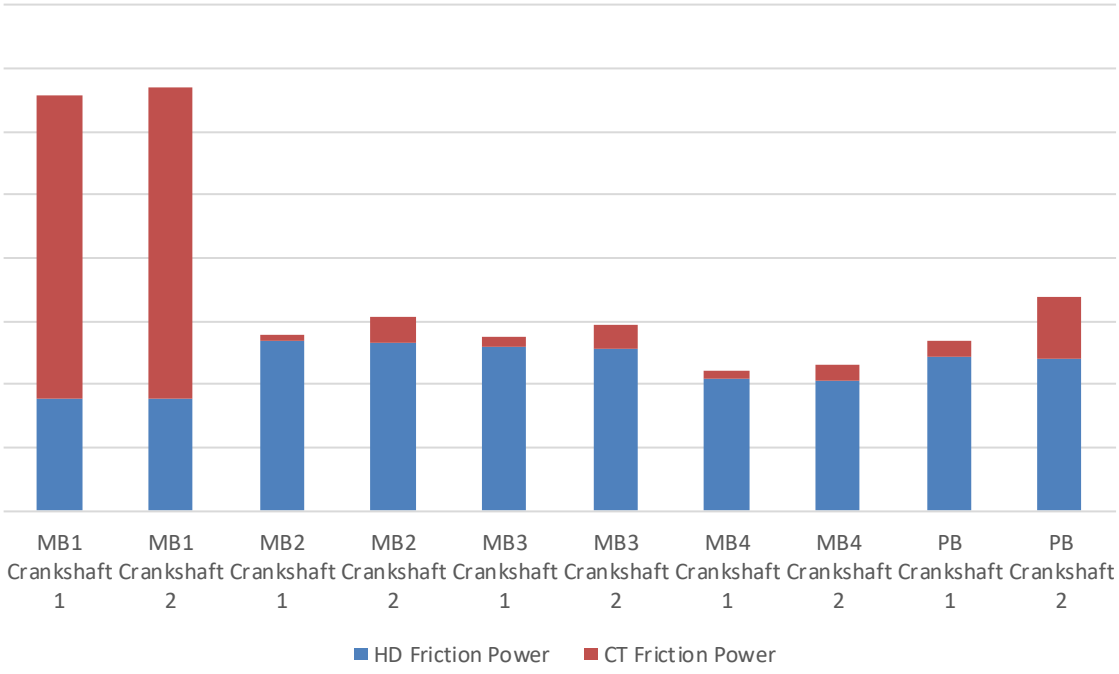

Figure 54 Friction power distribution at OP 1

6.2 RESULTS AT OP 2

This operating point represents a medium loaded, normal driving conditions at engine speed of 2200 RPM. At this point, as well as at OP 1, the most friction loss occurs on the main bearing, whereas the contact friction power is present in the highest portion. Except from main bearing no.1, almost no contact friction appears on the bearings. Another interesting thing can be noticed that the hydrodynamic friction is lower in every single bearing on the CS2, where the

surface roughness is significantly higher. However, this difference in HD friction power is negligible, hence, the sum for all bearings does not exceed 2%.

Table 4 Friction power distribution on slide bearings at OP 2

	MB1	MB2	MB3	MB4	PB	All bearings
HD Friction Power CS1	100,00	100,00	100,00	100,00	100,00	100,00
HD Friction Power CS2	99,72	98,40	98,66	99,91	98,65	98,91
CT Friction Power CS1	100,00	100,00	100,00	100,00	100,00	100,00
CT Friction Power CS2	107,24	1268,3	889,73	95,55	659,30	118,12
Total Friction Power CS1	100,00	100,00	100,00	100,00	100,00	100,00
Total Friction Power CS2	101,58	98,41	98,67	99,91	100,33	99,96

At this point can be concluded, that at this OP the difference in roughness values of the CS1 and CS2 has no major influence on the distribution of friction power loss.

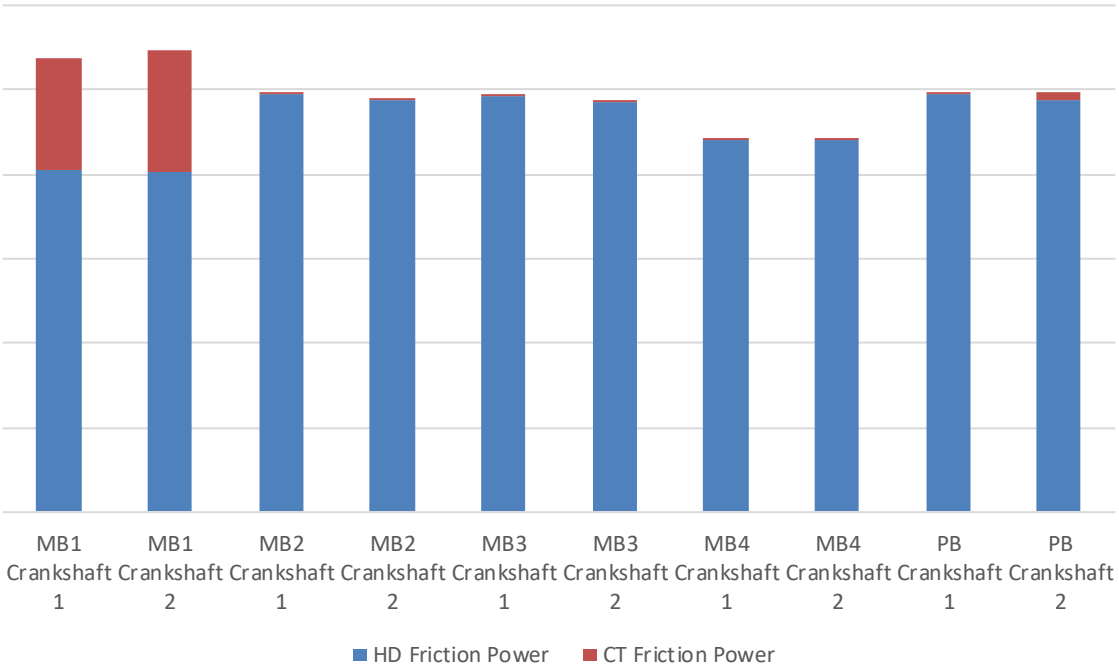

Figure 55 Friction power distribution at OP 2

6.3 RESULTS AT OP 3

With this operating point, the wide-open throttle position at maximum engine speed is simulated, since at this OP the engine parts must carry the highest load. This statement is perfectly confirmed by the comparison of the HD friction power and the contact friction power on the bearings at OP 1 and OP 3, which's percental values are listed in Table 5. Another representative comparison is shown in Figure 56 and Figure 57, where the friction power distributions on the pin bearing at OP 1 and OP 3 are demonstrated, respectively.

Table 5 Friction power difference between OP1 and OP3 of CS1

	MB1 CS1	MB2 CS1	MB3 CS1	MB4 CS1	PB CS1
HD Friction Power	494,18	424,11	437,67	528,63	681,73
CT Friction Power	559,58	578,62	1725,91	20216,58	9991,08

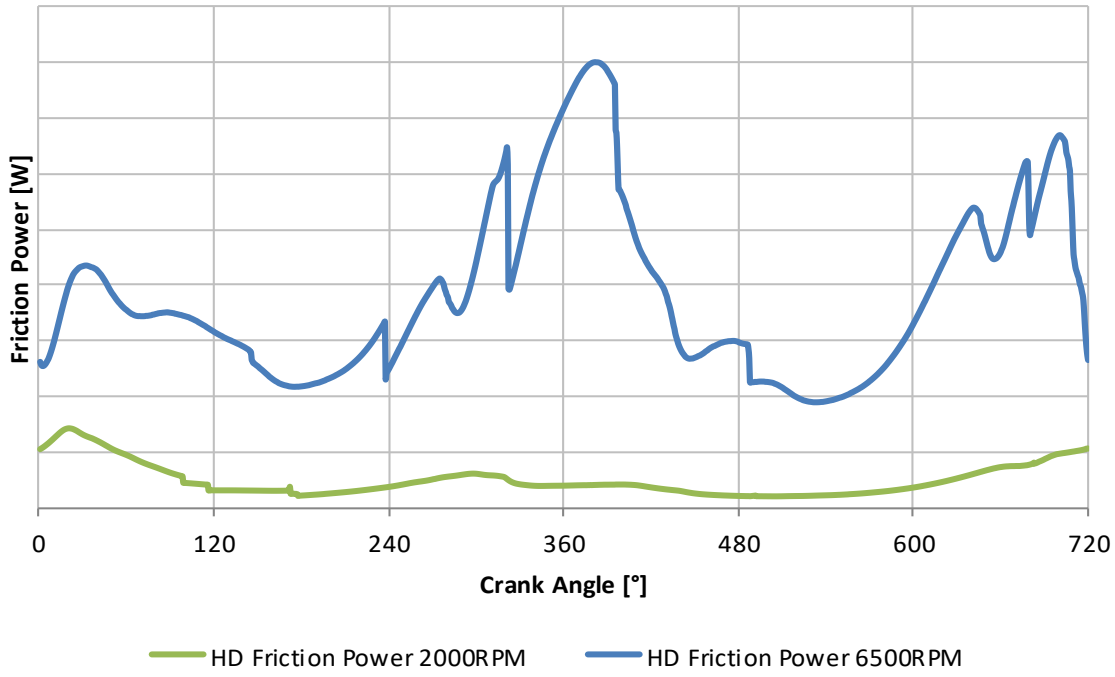

Figure 56 HD friction power distribution on the PB of CS1 at 2000RPM and 6500RPM

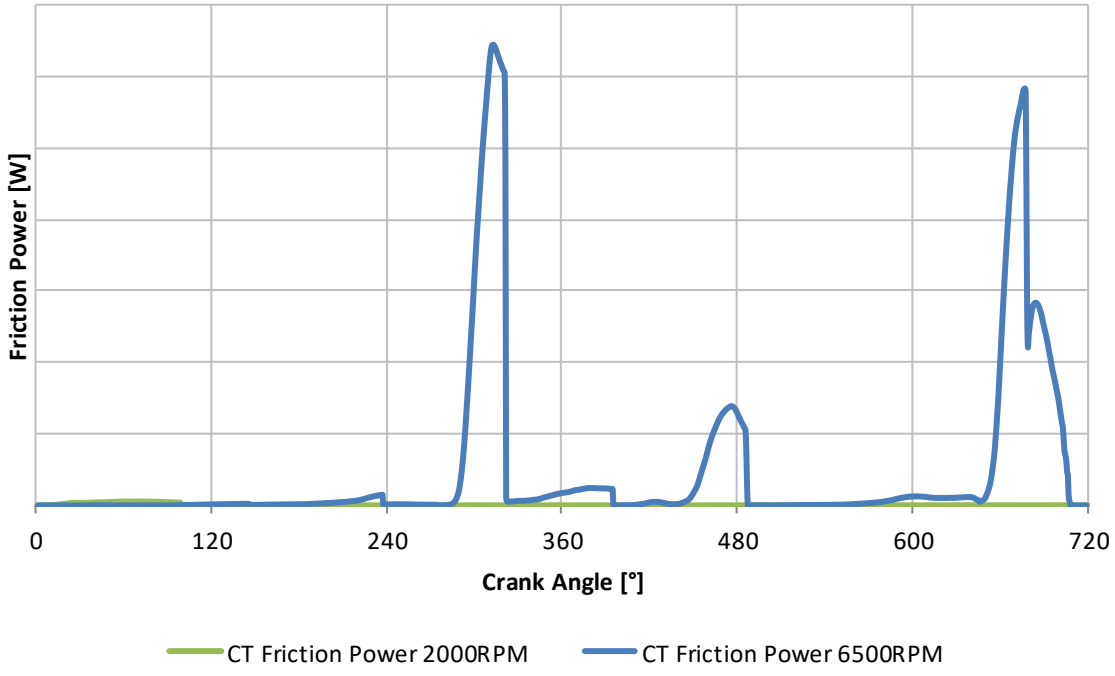

Figure 57 Contact friction power distribution on the PB of CS1 at 2000RPM and 6500RPM

Investigating the percentage of differences of friction power loss, it can be denoted that the HD friction power decreased slightly again, but the growth of the contact friction power is massive (see Table 6 and Figure 58). For the drop of the HD friction power the increased amount of the contact between the surface asperities of the bearings is responsible, which also carry an increased amount of load.

Table 6 Friction power distribution on slide bearings at OP 3

	MB1	MB2	MB3	MB4	PB	All Bearings
HD Friction Power CS1	100,00	100,00	100,00	100,00	100,00	100,00
HD Friction Power CS2	99,73	98,24	97,95	97,31	100,90	99,64
CT Friction Power CS1	100,00	100,00	100,00	100,00	100,00	100,00
CT Friction Power CS2	102,38	251,47	167,98	112,21	152,73	129,76
Total Friction Power CS1	100,00	100,00	100,00	100,00	100,00	100,00
Total Friction Power CS2	101,72	106,05	110,65	106,94	129,74	118,50

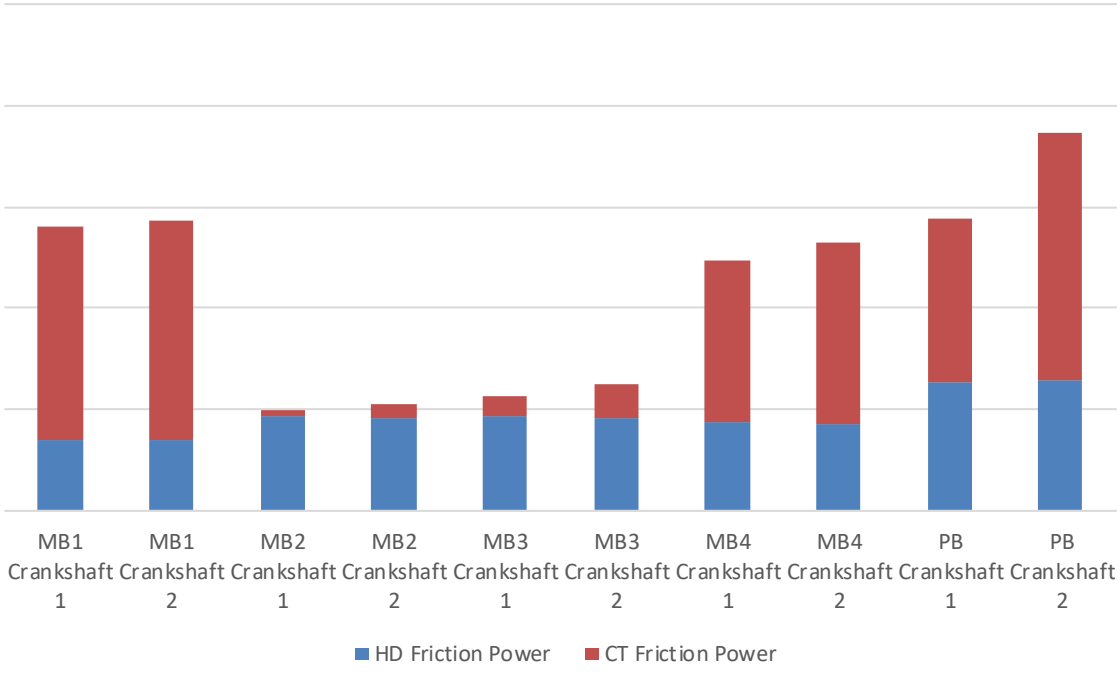

Figure 58 Friction power distribution at OP 3

Looking at the curves of relations of MOFT to RMS asperity height on main bearing 4, shown in Figure B.28, is remarkable, that at crank angle position around 160° negative values occur. Obviously, that state cannot be found in real, thus it needs a detailed investigation.
To find an exact position on the bearing surface, where negative values occur, the radial gap height has been visualized in a 3D plot. The sought points took place on the rear edge of the lower bearing shell at the edge of the crush relief and is highlighted in the Figure 59.

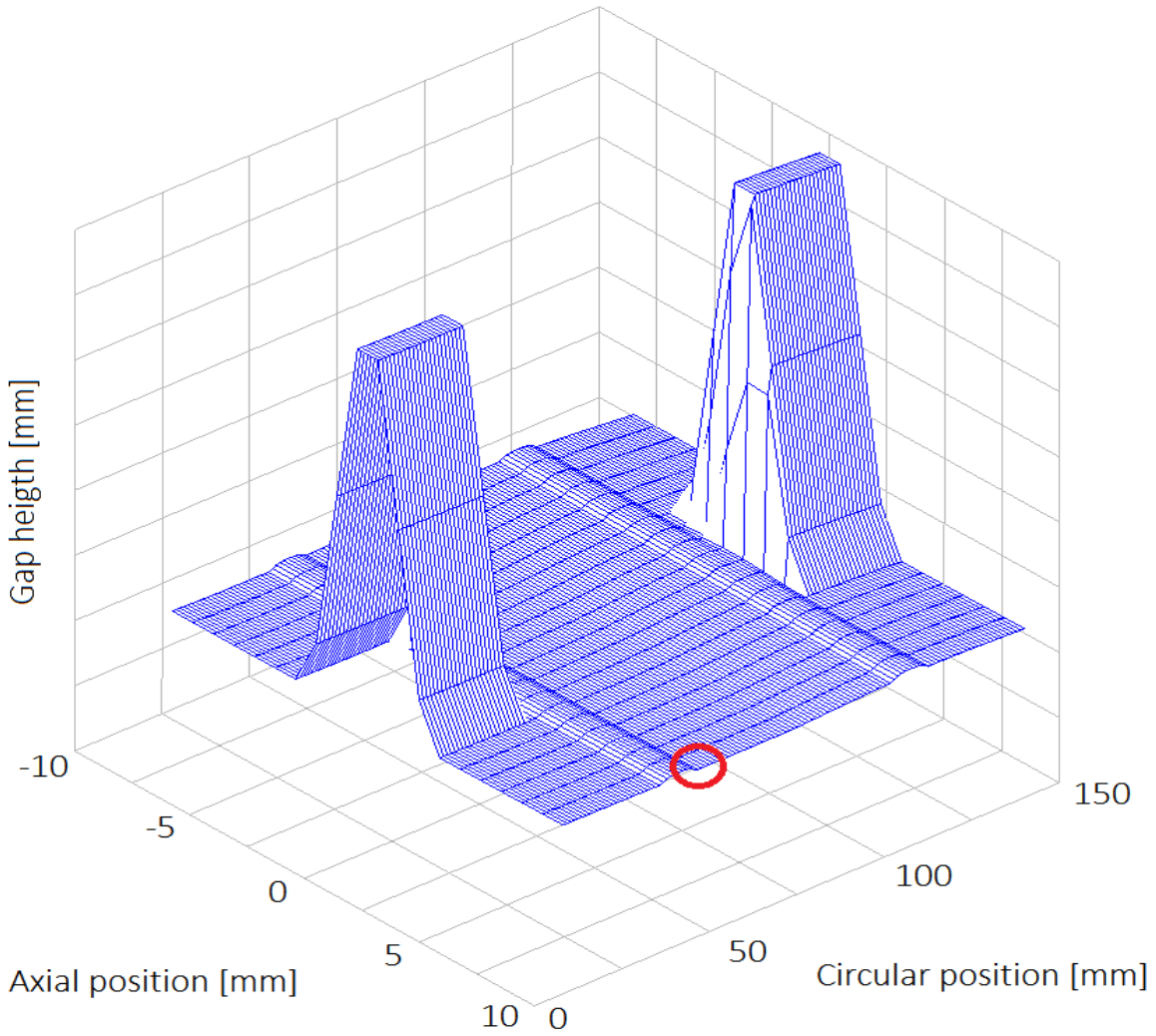

Figure 59 Radial gap height of main bearing 4 at crank angle position 160°

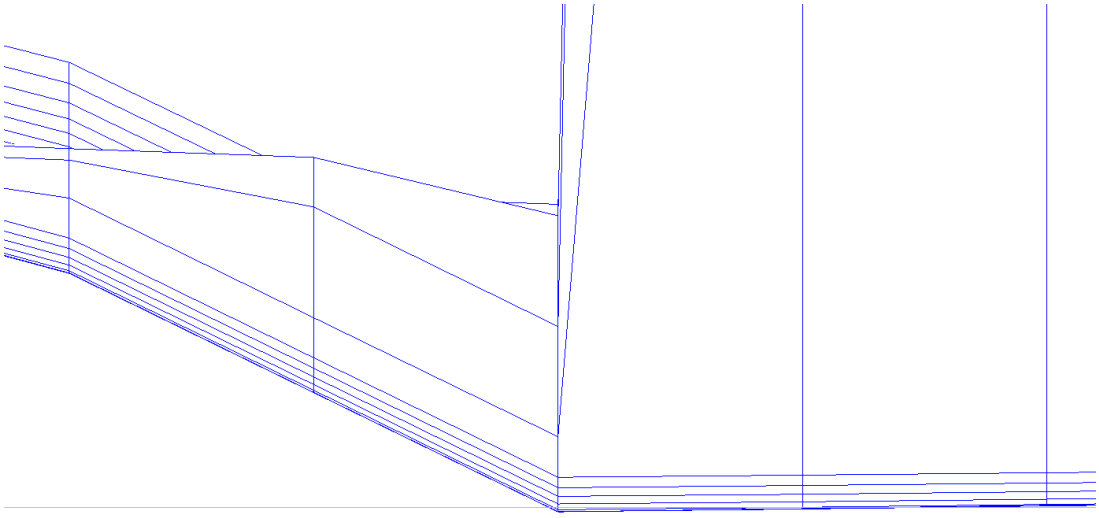

Figure 60 Detailed view of the affected area

In Figure 60 it can be seen, that only two grid points are affected, which grid points are not equal to the grid point set in the FE model. The presence of these negative values of MOFT can be originated by more factors acting simultaneously amplifying themselves, like the simplicity of the cranktrain model, high engine speed at high load. These are responsible for the high tilting of the crankshaft, affecting a point contact, with which the simulation algorithm cannot deal with. However, the affected area is so small, it does not have a significant effect on the friction power evaluation.

6.4 RESULTS AT OP 4

With this operation point the conditions of the engine friction power measurement are simulated. The engine is motored at its maximum speed with no load, hence the engine parts are only loaded by the inertia forces of its masses. Unexpectedly, this OP resulted in the highest friction power values. This is caused by several circumstances: the model's simplicity, as mentioned above at OP 1, and the simulation of the no load condition. Therefore, the pressure in the cylinders equals to zero throughout the whole simulation cycle, causing the domination of the inertia forces with no damping through gas forces.

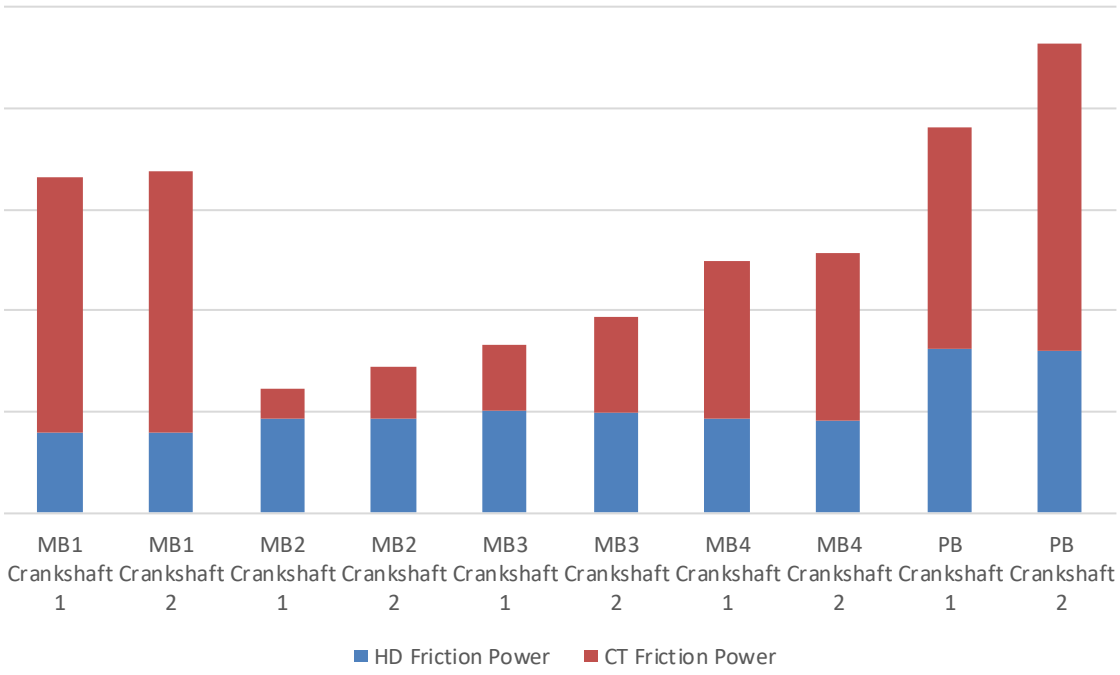

Figure 61 Friction power distribution at OP 4

Table 7 Friction power distribution on slide bearings at OP 4

	MB1	MB2	MB3	MB4	PB	All bearings
HD Friction Power CS1	100,00	100,00	100,00	100,00	100,00	100,00
HD Friction Power CS2	99,88	98,22	97,90	97,23	98,53	98,40
CT Friction Power CS1	100,00	100,00	100,00	100,00	100,00	100,00
CT Friction Power CS2	102,19	188,71	143,14	106,83	139,30	124,89
Total Friction Power CS1	100,00	100,00	100,00	100,00	100,00	100,00
Total Friction Power CS2	101,64	118,98	115,68	103,23	121,83	115,51

Analyzing the percentage of the distribution of the friction power between the two crankshafts, noticeable is again a massive difference in contact friction power of 24,89%. By this increment the total friction power of the bearings rose by 15,51%.

At this OP, similarly to OP 3, there are also noticeable negative values in the curves of the relations of the MOFT to the RMS asperity height at main bearing 4. This time, these have been identified exactly on the opposite position of that end of the bearing shell, as it was at OP 3, highlighted in Figure 62.

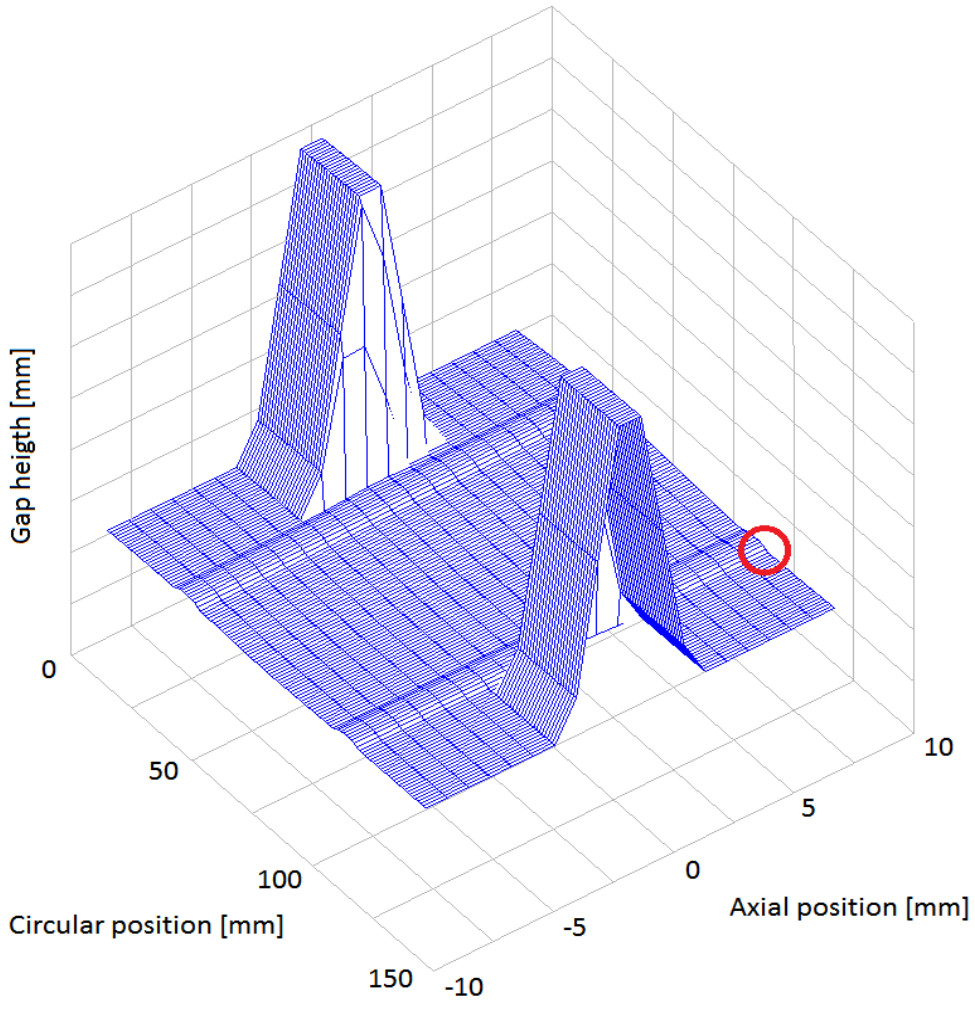

Figure 62 Radial gap height of main bearing 4 at crank angle position 60°

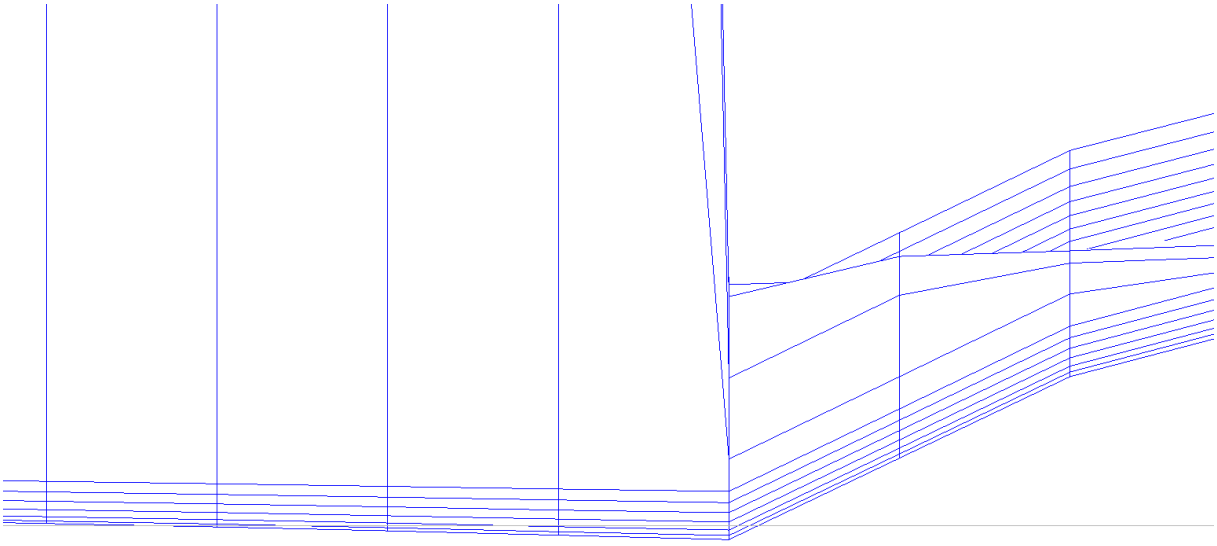

Figure 63 Detailed view of the investigated area

Here six grid points of the plotting mesh are below zero value, covering a total area of approximately 5 mm^2. These false values are resulted by the tilting of the crankshaft up to the boundaries. This extreme tilting of the crankshaft is caused by the sum of inertia forces of the piston assemblies, which's load cannot be carried by this tiny area. However, the statement made at OP 3 is valid here also, that this area is not big enough, to have a significant impact to power loss evaluation.
Under real conditions at this point would be discernible an elevated wear, till the shape of the bearing shell would not be sufficient to avoid direct surface to surface contact. On the other hand, this state would not be developing in real nor in a more complex simulation model.

CONCLUSIONS

Within this thesis, radial slide bearings of inline three-cylinder engine were analyzed at four operating points. In addition surface properties of two different crankshaft bearing journals were compared, where the difference of the RMS roughness differs by over 17%. By this disparity, significant increase of the contact friction power can be observed in the range of 18-33%, depending on the instantaneous operating conditions. At this point it must be highlighted, that the analyzed surface samples were all unworn. Hence, these values of friction power are characterizing the run-in phase of the engine. In the future, it would be worthy to gain data of 3D surface profile of bearing parts after the run-in phase, and analyze them the same way as it was done in this work.

The results of the analyses show, how much effect has the quality of the manufactured bearing surfaces on the friction loss. Especially in these days, when every percent plays a crucial role in the process of improving the engines' efficiency.

The built model contains only the main part of the cranktrain mechanism, so the influence of the clutch, transmission, valvetrain, oil pump etc. was not considered. Thereby, the model's complexity level is appropriate to investigate the influence of surface roughness on the magnitude of friction.

Hence can be concluded, that the defined goals of this master's thesis were successfully accomplished.

SUMMARY

The aim of this master's thesis was to perform a background research of current approaches for hydrodynamic slide bearing calculations, carry out a parametric study about influence of rough surface topography on tribological characteristics of slide bearings under various operating conditions and draw conclusions of the executed analyses.

The first and the second part of this master's thesis give a brief overview of the principle of operation of gasoline four-stroke internal combustion engines and slide bearings' construction. In the third chapter, terms such as tribology, friction and lubrication are explained, including the regimes of the lubrication and the prerequisites of formation of hydrodynamic lubrication.

The next part of this work is dedicated to the description of the elasto-hydrodynamics. The Reynolds equation is introduced in its original form and in advanced shape, supplemented by flow-factors by researchers Patir and Cheng. Further, the pressure dependence of viscosity and density is described. Another essential part of the EHD calculations, the determination of the contact pressure is introduced.

The following, fifth chapter is devoted to the description of the building process flow of the engine simulation model for the slide bearing analyses in FEV Virtual Engine, including the explanation of the function of the components used while building a model. In this chapter declared is also the measurement of the 3D rough surface topography of the journal and bearing shell samples, provided by Škoda Auto. The scanned surface profiles are included into the simulations, which's influence is investigated on the tribological characteristics of the slide bearings.

REFERENCES

[1] BARTZ, W.J. *Einführung in die Tribologie und Schmierungstechnik: Tribologie-Schmierstoffe-Anwendungen*. Renningen: Expert, 2010. ISBN 978-3-8169-2830-0.

[2] BARUS, C. *Isotherms, Isopiestics and Isometrics Relative to Viscosity*, American Journal of Science, Vol. 45, 1893, pp. 87-96.

[3] DRÁPAL, L. *Hnací ústrojí šestiválcového leteckého motoru* [online]. Brno, 2008. Master's thesis. Brno University of Technology.

[4] FICZA, I. *Effects of non-Newtonian lubricants on surface roughness in point contacts*. Brno, 2015. 154 p. PhD thesis. Brno University of Technology, Faculty of Mechanical Engineering, Institute of Machine and Industrial Design. Supervisor: prof. Ing. Martin Hartl, Ph.D.

[5] HAMROCK, B.J. and D. DOWSON. *Ball Bearing Lubrication, The Elastohydrodynamics of Elliptical Contacts*. John Willey & Sons. 1981.

[6] HEYWOOD, John B. *Internal combustion engine fundamentals*. 1. New York: McGraw-Hill, 1988.

[7] GREENWOOD, J. A. and J. H. TRIPP. The Contact of Two Nominally Flat Rough Surfaces. *Proceedings of the Institution of Mechanical Engineers*, 1970. ISSN 0020-3483. Available from: http://pme.sagepub.com/lookup/doi/10.1243/PIME_PROC_1970_185_069_02

[8] KOVAŘÍK, L., V. FERENCEY, R. SKALSKÝ, L. ČÁSTEK. *Konstrukce vozidlových spalovacích motorů*. 1. 1992. ISBN 80-206-0131-7.

[9] MARŠÁLEK, O. *Advanced Methods for the Solution of Journal Bearing Dynamics*. Dissertation. Brno: Brno University of Technology, Faculty of Mechanical Engineering. 2015.

[10] NOVOTNÝ, P. *Virtual Engine – A Tool for Powertrain Development*. Inaugural Dissertation. Brno: Brno University of Technology. 2009.

[11] PATIR, N. and H. CHENG. *An Average Flow Model for Determining Effects of three-Dimensional Roughness on Partial Hydrodynamic Lubrication*. ASME Journal of Lubrication Technology, Vol. 100, pp. 12-17. 1978.

[12] PATIR, N. and H. CHENG. *Application of Average Flow Model to Lubrication Between Rough Sliding Surfaces*. Journal of Lubrication Technology, vol. 101, issue 2. 1979.

[13] ROELANDS, C. J. A. *Correlational Aspect of Viscosity-Temperature-Pressure Relationships of Lubricating Oils*, PhD thesis, Delft University of Technology, The Netherlands, 1966.

[14] SKALSKÝ, R., J. BUKOVSKÝ. *Konstrukce pístových spalovacích motorů. část I. Dynamika, vyvažování a torzní kmity*. 1. 1971.

[15] STACHOWIAK, G. *Engineering tribology*. 4th ed. Oxford: Butterworth-Heinemann. 2014.

[16] WANNATONG, K. Simulation Algorithm for Piston Ring Dynamics. Simulation Modelling Practice and Theory. 2008. vol. 16, no. 1, p. 127-146. DOI 10.4271/2001-01-3368.

[17] WIJNANT, Y. H. *Contact Dynamics in the field of Elastohydrodynamic Lubrication*. Ph.D. Thesis, University Enschede, The Netherlands, 1998.

[18] *Engine Bearings*. Catalogue. Neuenstadt, 2016. MS Motorservise International GmbH a Rheinmetall Company.

[19] ACHIM, A., P. MICHEL, W. MAIK. *Kurbelwellenlager für Motoren mit Start-Stopp-System*. MTZ [online]. 2010, 71 (12), 4. Available from: https://www.researchgate.net/publication/257279075_Kurbelwellenlager_fur_Motoren_mit_Start-Stopp-System.

[20] KERESZTES, R. Zs. *Műszaki műanyag/acél csúszópárok tribológiai kutatása: polimer/acél fogfelületek súrlódása* [online]. Gödöllő, 2009. Available from: https://szie.hu//file/tti/archivum/Keresztes_Robert_phd.pdf. Dissertation. Szent István Universtiy.

[21] KOPIELOVICH, D. *Bearings in internal combustion engines* [online]. Available from: http://www.substech.com/dokuwiki/doku.php?id=bearings_in_internal_combustion_engines.

[22] KOPIELOVICH, D. *Engine bearing materials* [online]. Available from: http://kingbearings.com/files/Engine_Bearing_Materials.pdf

[23] *KS R30 Lead-free Steel-Aluminum Composite Material for Main Bearings and Conrod Bearings*. Kolbenschmidt Pierburg Group. St. Leon-Rot, 2016. Available from: http://cdn.rheinmetall-automotive.com/fileadmin/media/kspg/Broschueren/Poduktbroschueren/KS_Gleitlager/Metallische_Gleitlager/g_r30_e.pdf

[24] *KS X20T Lead-free Steel/Brass Composite with Sputter Coating Surface for Plain Bearings of Maximum Load Capacity*. Kolbenschmidt Pierburg Group. St. Leon-Rot, 2016. Available from: http://cdn.rheinmetall-automotive.com/fileadmin/media/kspg/Broschueren/Poduktbroschueren/KS_Gleitlager/Metallische_Gleitlager/g_x20t_e.pdf

[25] NOVOTNÝ, P. *Počítačové simulace v automobilovém průmyslu II.* Presentation. Brno: Brno University of Technology. 2016.

[26] *Basics of lubrication*. In: Society of tribologists and lubrication engineers [online]. Available from: http://www.stle.org/resources/lubelearn/lubrication/#top

[27] Bruker ContourGT-X. Bruker [online]. 2017. Available from: https://www.bruker.com

[28] *Encyclopedia Britannica*, Available from: https://media1.britannica.com/eb-media/16/97216-004-D655301C.jpg

[29] *FEV Virtual Engine* 24.2, Help version: 24.2.5971, 2016. FEV GmbH.

[30] *Interne Ausgaben für Forschung und Entwicklung im Automobilbau in Deutschland von 2011 bis 2015 (in Millionen Euro).* In: Statista [online]. Available from: https://de.statista.com/statistik/daten/studie/150648/umfrage/forschung-und-entwicklung-im-deutschen-automobilbau/

[31] *Lubrication systems for petrol engines* (automobile). In: What-when-how [online]. Available from: http://what-when-how.com/automobile/lubrication-systems-for-petrol-engines-automobile/

[32] *TheShortSpan* [online]. Available from: http://theshortspan.com/photo/friction/contactarea.png

[33] Yuriko Kondo, Tahahiro Koyoma and Shinya Sasaki. *Tribological Properties of Ionic Liquids, Ionic Liquids: New Aspects for the Future*, 2013. Dr. Jun-ichi Kadokawa (Ed.), InTech, DOI: 10.5772/52595. Available from: http://www.intechopen.com/books/ionic-liquids-new-aspects-for-the-future/tribological-properties-of-ionic-liquids.

LIST OF ABBREVIATIONS

3D	3-dimensional
BDC	Bottom dead center
CAD	Computer-aided design
CS	Crankshaft
CT	Contact
DOF	Degree of freedom
EHD	Elasto-hydrodynamic
EHL	Elasto-hydrodynamic lubrication
FEM	Finite element method
HD	Hydrodynamic
HHT	Hilber-Hughes-Taylor
ICE	Internal combustion engine
MB	Main bearing
MBS	Multibody system
MOFT	Minimum oil film thickness
OP	Operating point
PB	Pin bearing
RMS	Root mean square
RPM	Revolution per minute
TDC	Top dead center
VE	FEV Virtual Engine

LIST OF SYMBOLS

a	[m]	Radius of the contact area
D	[m]	Cylinder bore diameter
E'	[Pa]	Combined modulus of elasticity
E_1, E_2	[Pa]	Young's modulus
$F_{5/2}$	[-]	Function of contact pressure increase
F_p	[N]	Gas force
h	[m]	Oil film thickness
h_T	[m]	Local lubricant film thickness
p	[Pa]	Hydrodynamic pressure
p_0	[Pa]	Atmospheric pressure
$p_{average}$	[Pa]	Average contact pressure
p_c	[Pa]	Contact pressure
p_g	[Pa]	Pressure in the combustion chamber
p_{max}	[Pa]	Maximal contact pressure
R'	[m]	Reduced radius of curvature
R_A, R_B	[m]	Radii of spheres
t	[s]	Time
U_1, U_2	[m s^{-1}]	Tangential velocity of surface 1 and 2
V_c	[m^3]	Clearance volume
V_t	[m^3]	Maximum cylinder volume
W	[N]	Normal contact force
x, y		Cartesian coordinates along x and y axes
z	[-]	Pressure-viscosity index
α	[-]	Pressure-viscosity coefficient
β	[m]	Average radius of curvature of asperities

γ	[-]	Peklenik number
δ_1, δ_2	[m]	Amplitudes of rough surface irregularities
η	[kg m^{-1} s^{-1}]	Lubricant dynamic viscosity
η_0	[kg m^{-1} s^{-1}]	Dynamic viscosity at atmospheric pressure
η_r	[m^{-2}]	Surface density of asperity peaks
ν	[m^2 s^{-1}]	Kinematic viscosity
ν_1, ν_2	[-]	Poisson's constant of materials
ρ	[kg m^{-3}]	Lubricant density
ρ_0	[kg m^{-3}]	Lubricant density at atmospheric pressure
σ	[m]	Standard deviation of combined surface roughness
τ	[Pa]	Shear stress
ϕ_s	[-]	Shear flow factor
ϕ_x, ϕ_y	[-]	Pressure flow factors in x and y direction

APPENDIX A

Technical specifications of the BRUKER ContourGT-X optical profilometer [27]:

Max. Scan Range	**Up to 10 mm**
Vertical Resolution	0.05 nm (motor); 0.01 nm (PZT)
RMS Repeatability	0.01 nm (motor); 0.004 nm (PZT)
Lateral Resolution	0.38 μm min (Sparrow criterion); 0.13 μm (with AcuityXR™); 0.01 μm (with NanoLens™)
Step Height Accuracy	<0.75% for step heights 8 μm and greater
Step Height Repeatability	<0.1% 1 sigma repeatability
Max. Scan	114 μm/sec (with standard camera)
Sample Reflectivity	0.05%-100%
Max. Sample Slope	Up to 40° (shiny surfaces); Up to 87° (rough surfaces)
Sample Height	Up to 100 mm
Sample Weight	Up to 23 kg (50 lbs)
XY Sample Stage	200 mm (8 in.) automated (standard); 300 mm (12 in.) automated (optional); 0.5 μm encoders
Z Focusing	100 mm (4 in.) automated
Tip/Tilt Function	±6° automated, computer-controlled tip/tilt head
Optical Metrology Module	Patented dual-LED illumination; Single-objective adapter; Optional automated or manual turret
Objectives	Parfocal: 2.5x, 5x, 10x, 20x, 50x, 115x LWD: 1x, 1.5x, 2x, 5x, 10x TTM: 2x, 5x, 10x, 20x Bright field: 2.5x, 5x, 10x, 50x
Available Zoom Lenses	0.55x, 0.75x, 1x 1.5x, 2x auto-sensing modules
Camera	Standard monochrome: 640x480 High-resolution monochrome (option): 1392x1040 Color (option): 640x480
XY Automation	Automated stitching, scatter, and grid automation
Calibration	Via traceable step standards; Optional auto and continuous integral laser signal
System Footprint	852 mm (W) x 793 mm (D) x 1608 mm (H)
Weight	493 kg (1084 lbs)

APPENDIX B

Visualization of results at OP 1

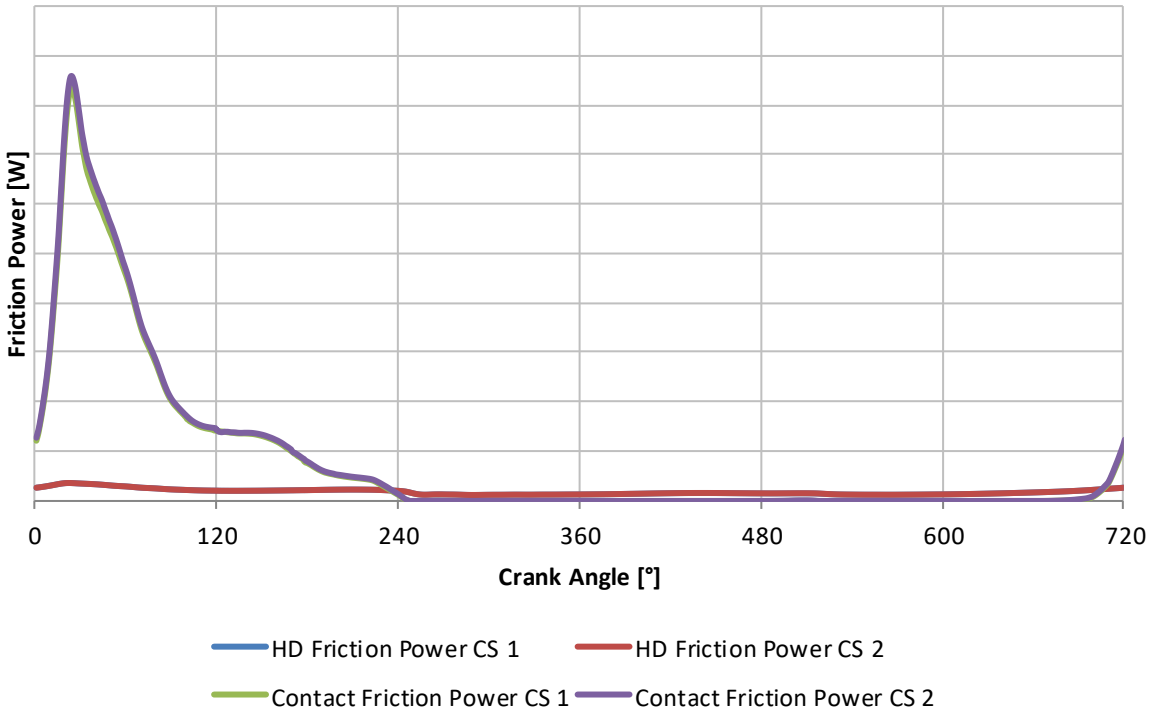

Figure B.1 Friction power of main bearing no.1 at OP 1

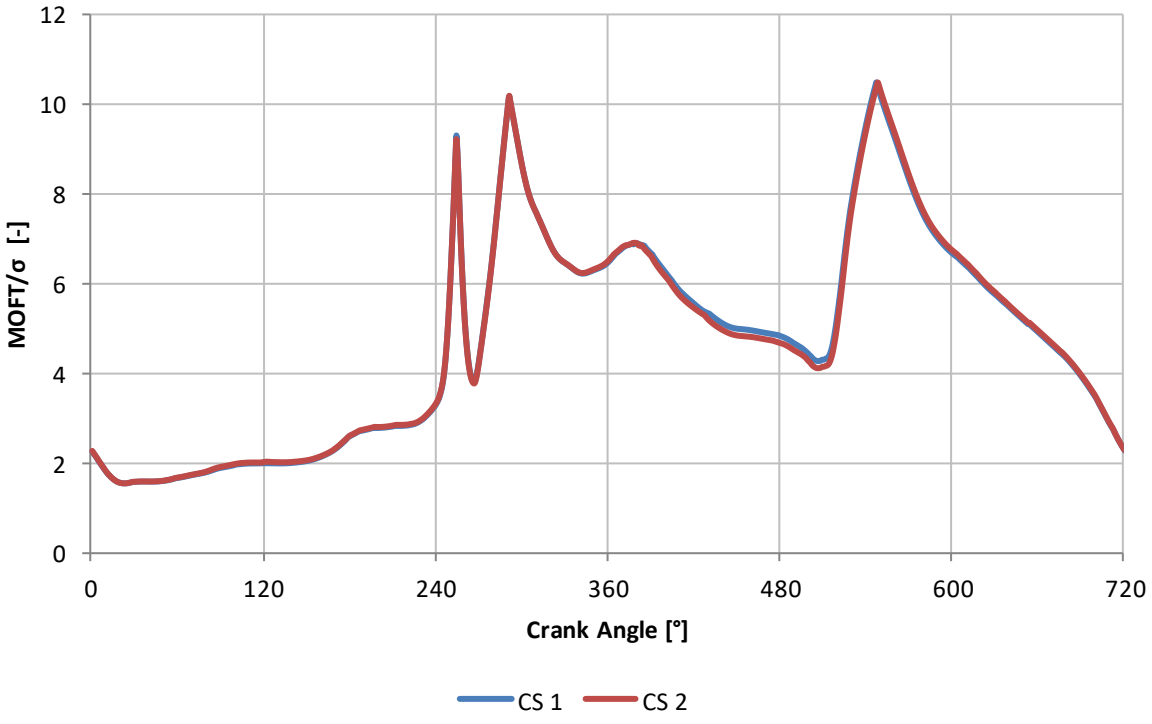

Figure B.2 Relation of the MOFT/σ of main bearing no.1 at OP 1

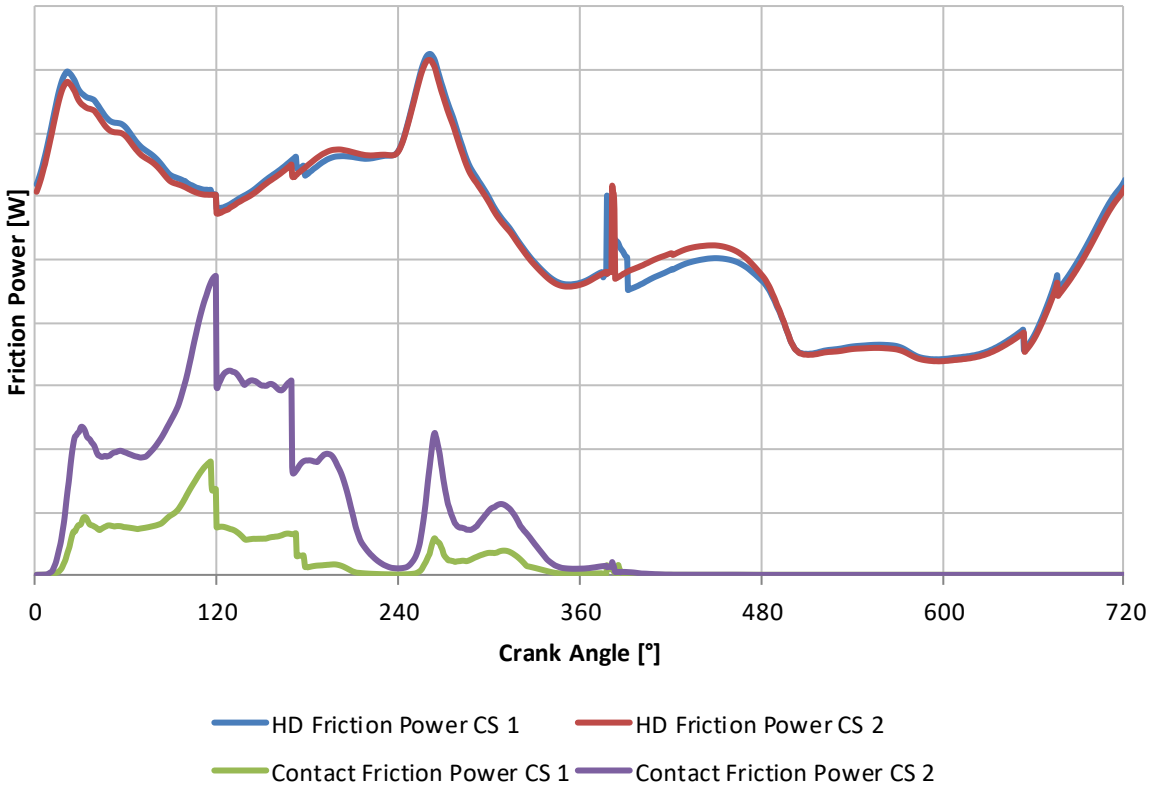

Figure B.3 Friction power of main bearing no.2 at OP 1

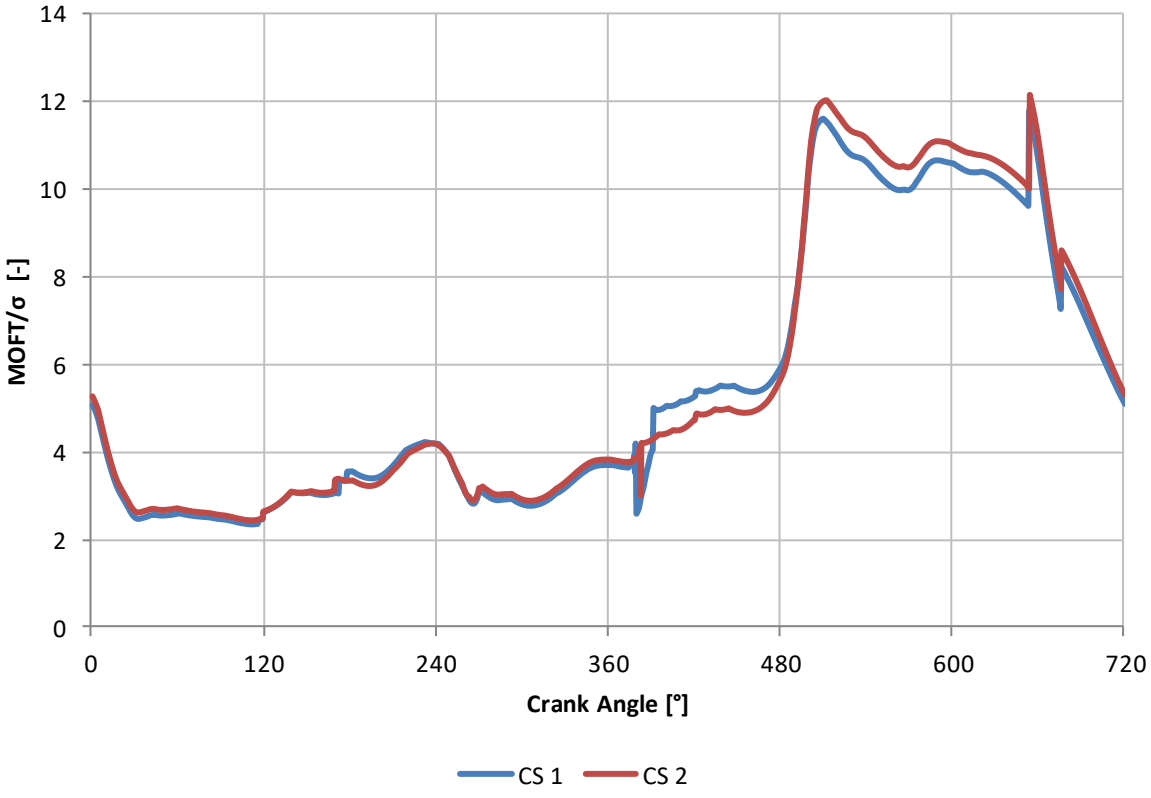

Figure B.4 Relation of the MOFT/σ of main bearing no.2 at OP 1

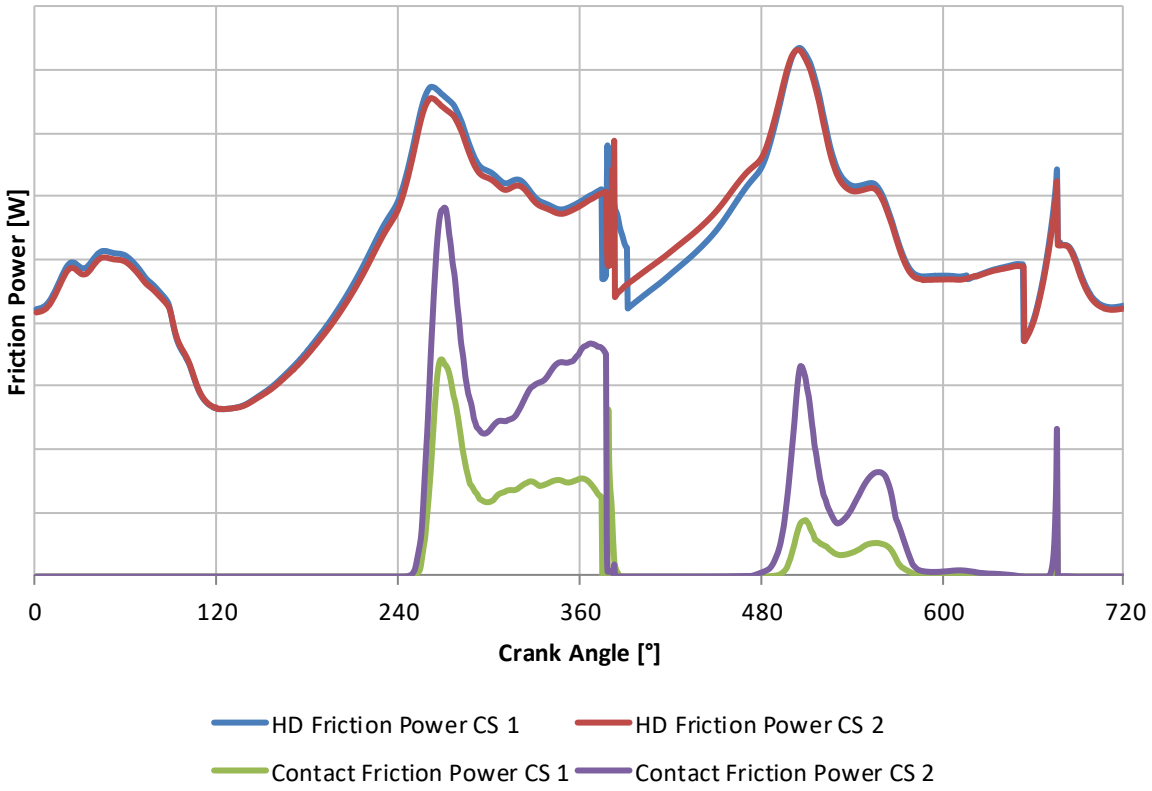

Figure B.5 Friction power of main bearing no.3 at OP 1

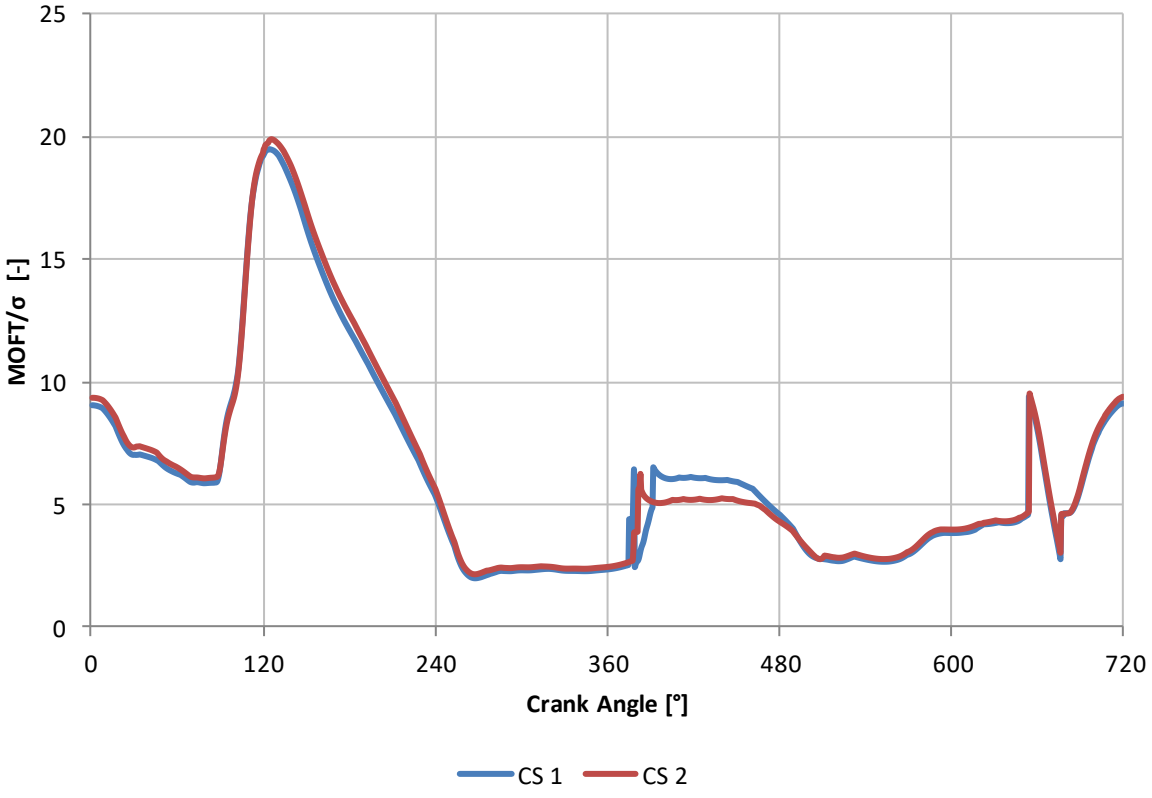

Figure B.6 Relation of the MOFT/σ of main bearing no.3 at OP 1

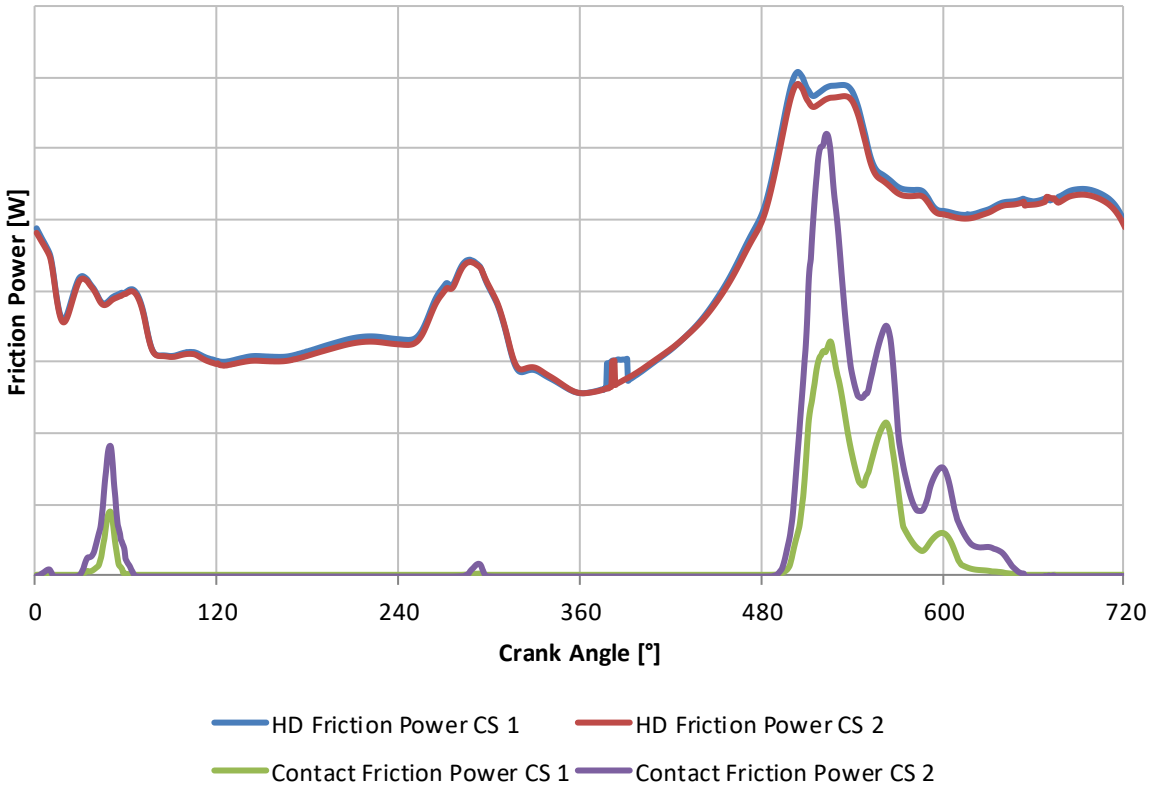

Figure B.7 Friction power of main bearing no.4 at OP 1

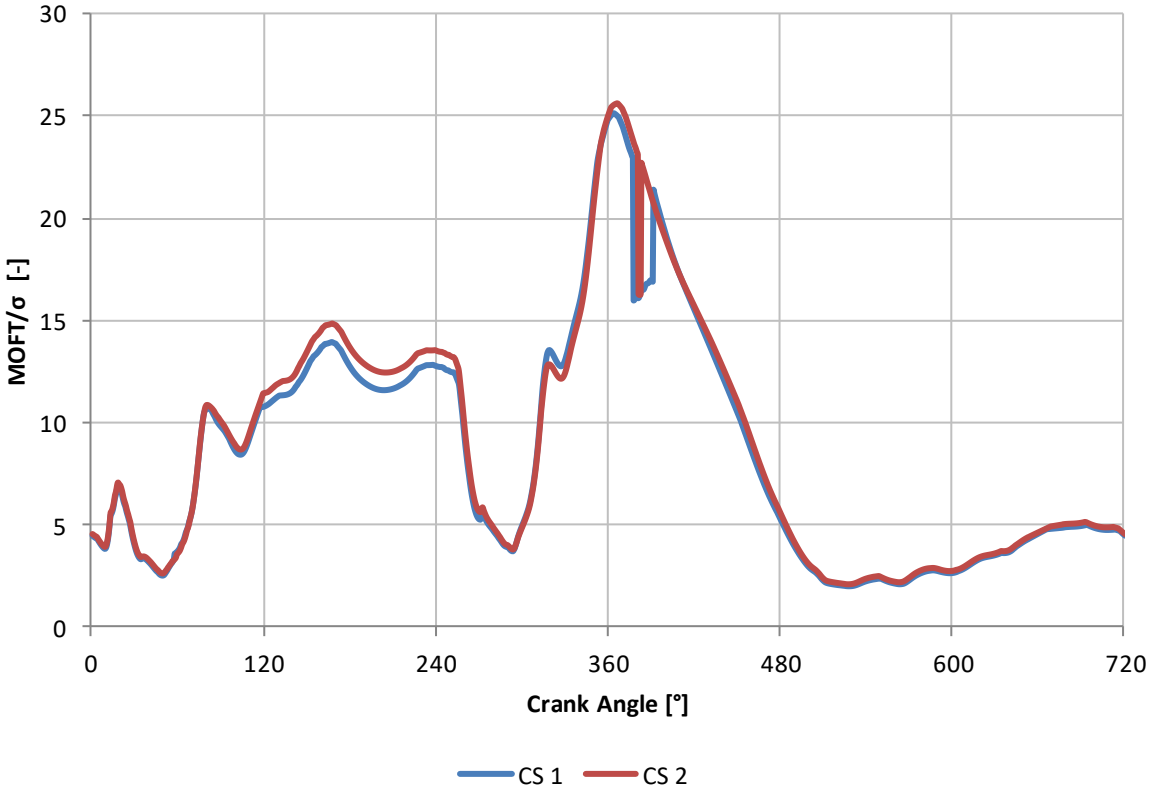

Figure B.8 Relation of the MOFT/σ of main bearing no.4 at OP 1

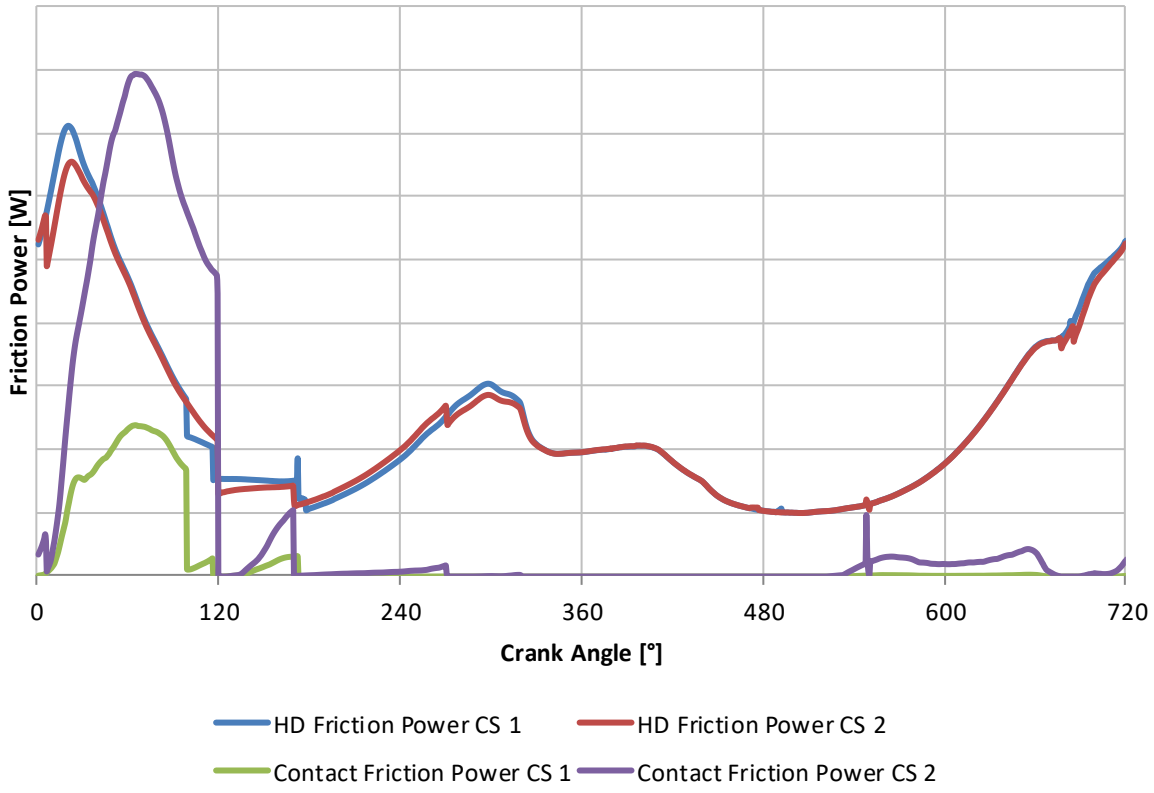

Figure B.9 Friction power of pin bearing at OP 1

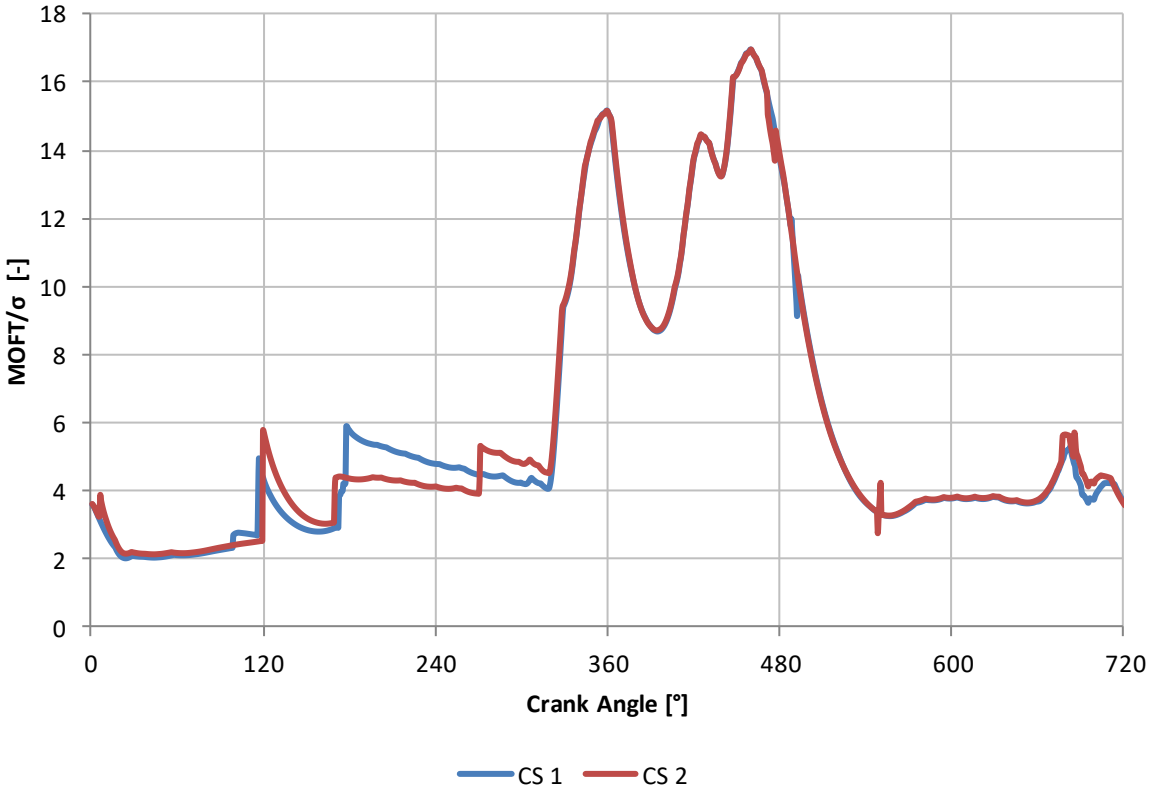

Figure B.10 Relation of the MOFT/σ of pin bearing at OP 1

Visualization of results at OP 2:

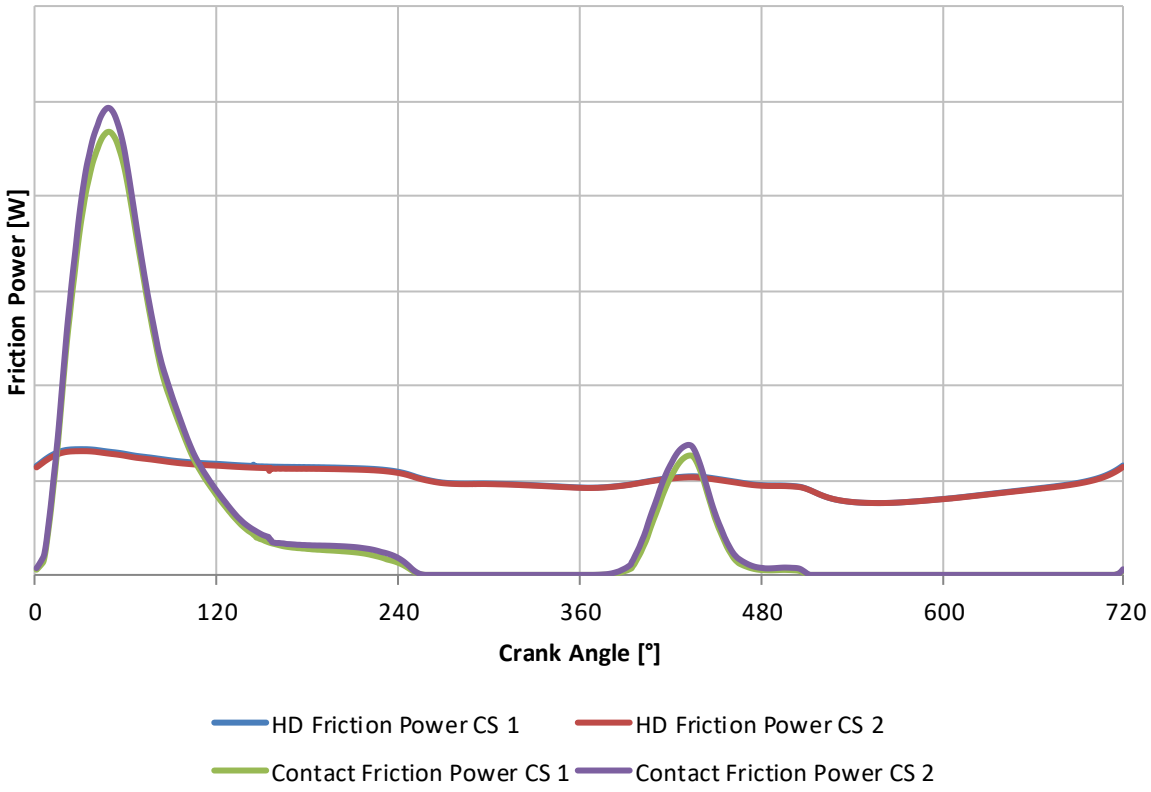

Figure B.11 Friction power of main bearing no.1 at OP 2

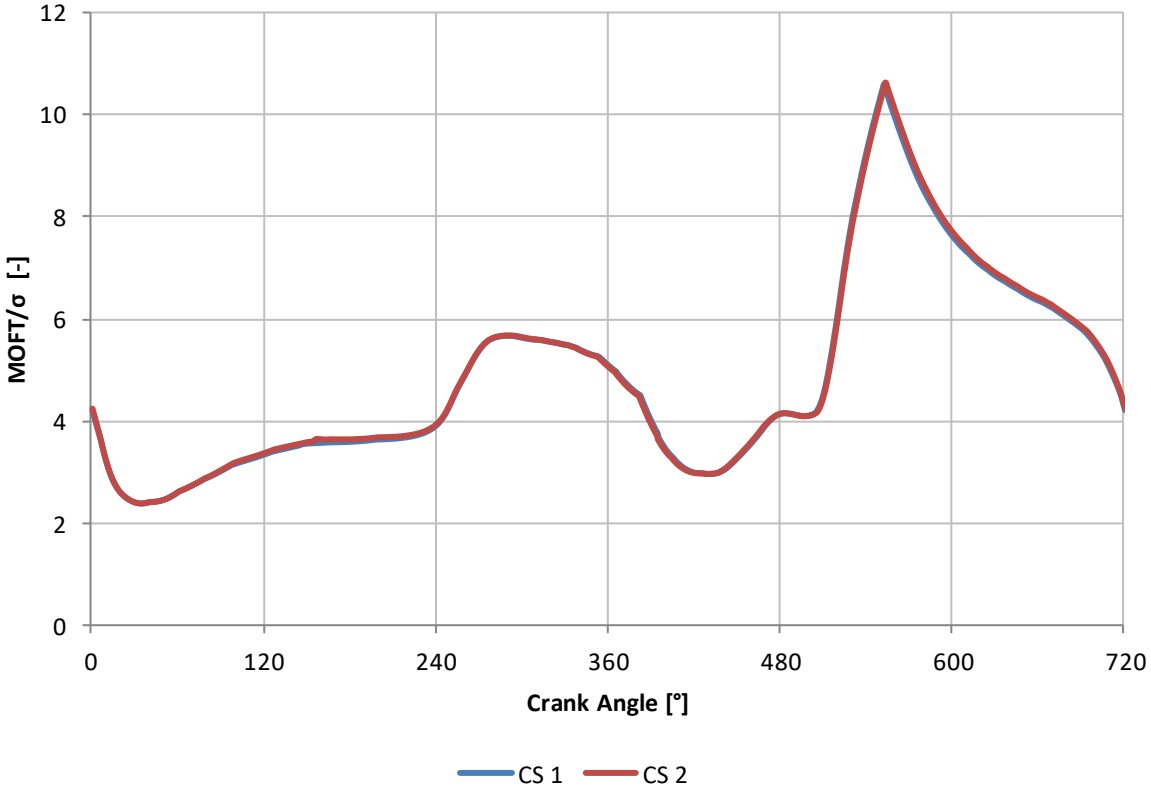

Figure B.12 Relation of the MOFT/σ of main bearing no.1 at OP 2

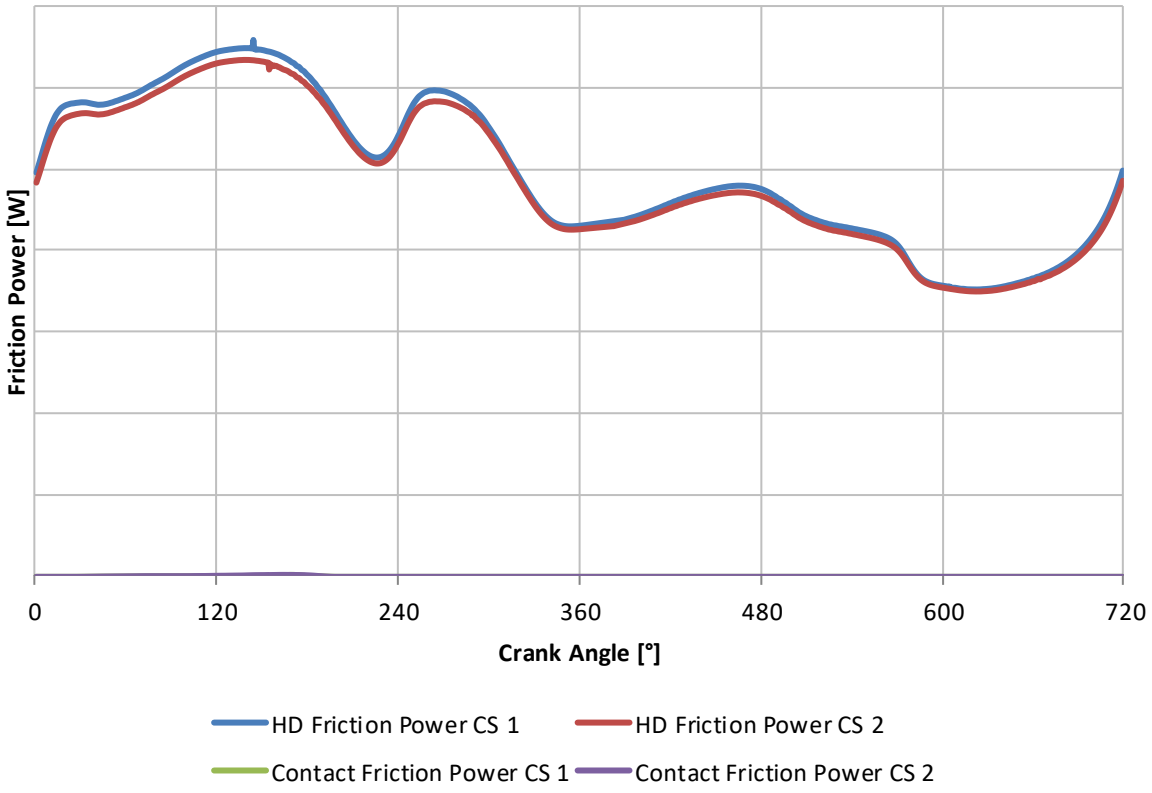

Figure B.13 Friction power of main bearing no.2 at OP 2

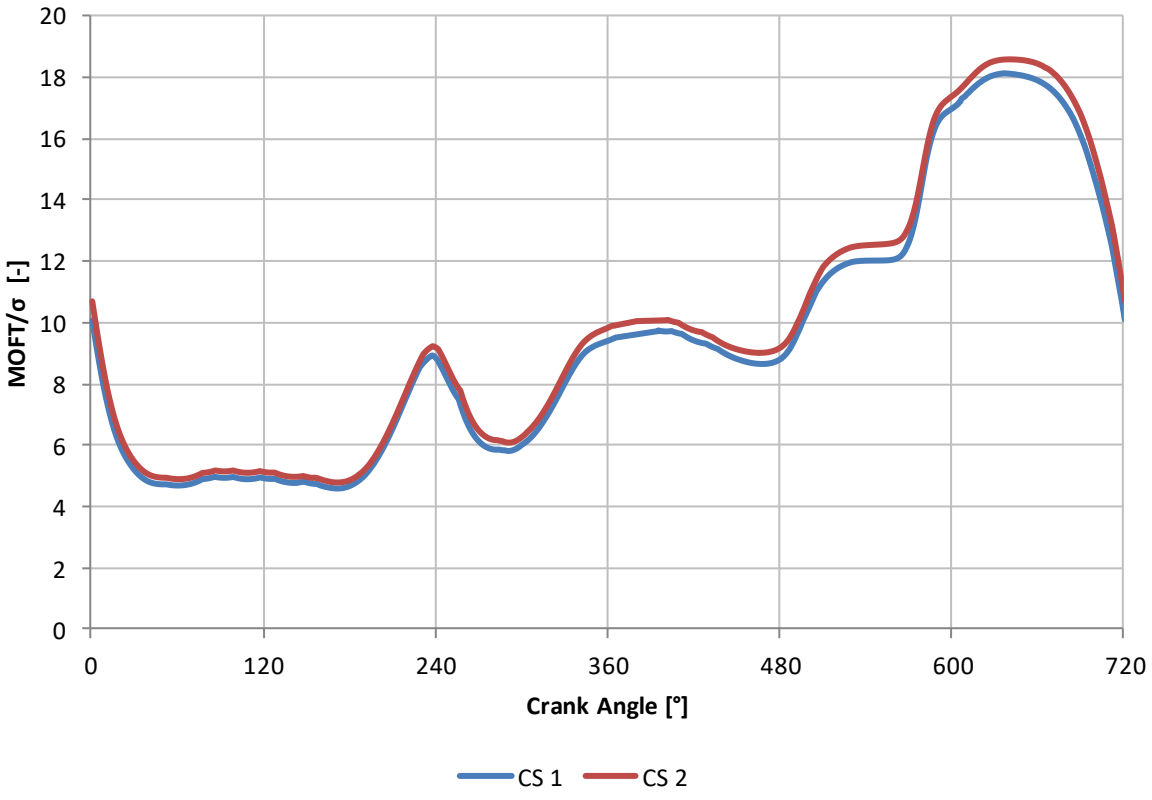

Figure B.14 Relation of the MOFT/σ of main bearing no.2 at OP 2

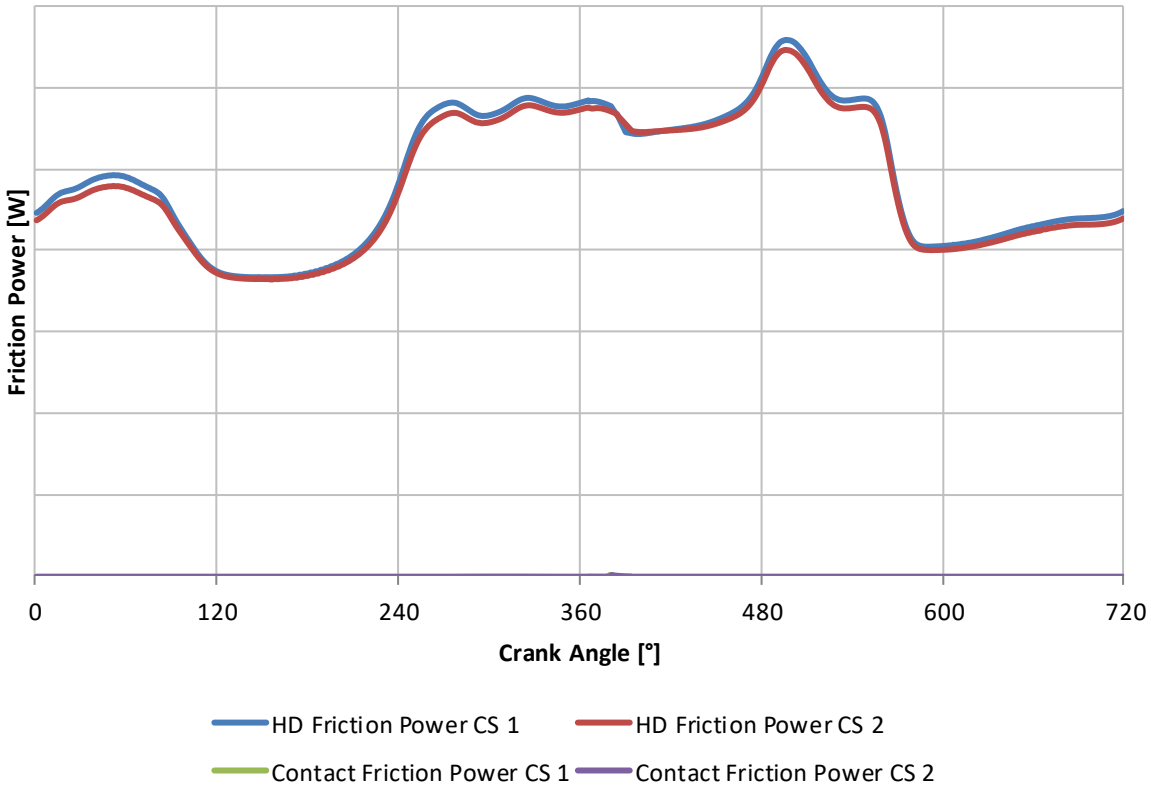

Figure B.15 Friction power of main bearing no.3 at OP 2

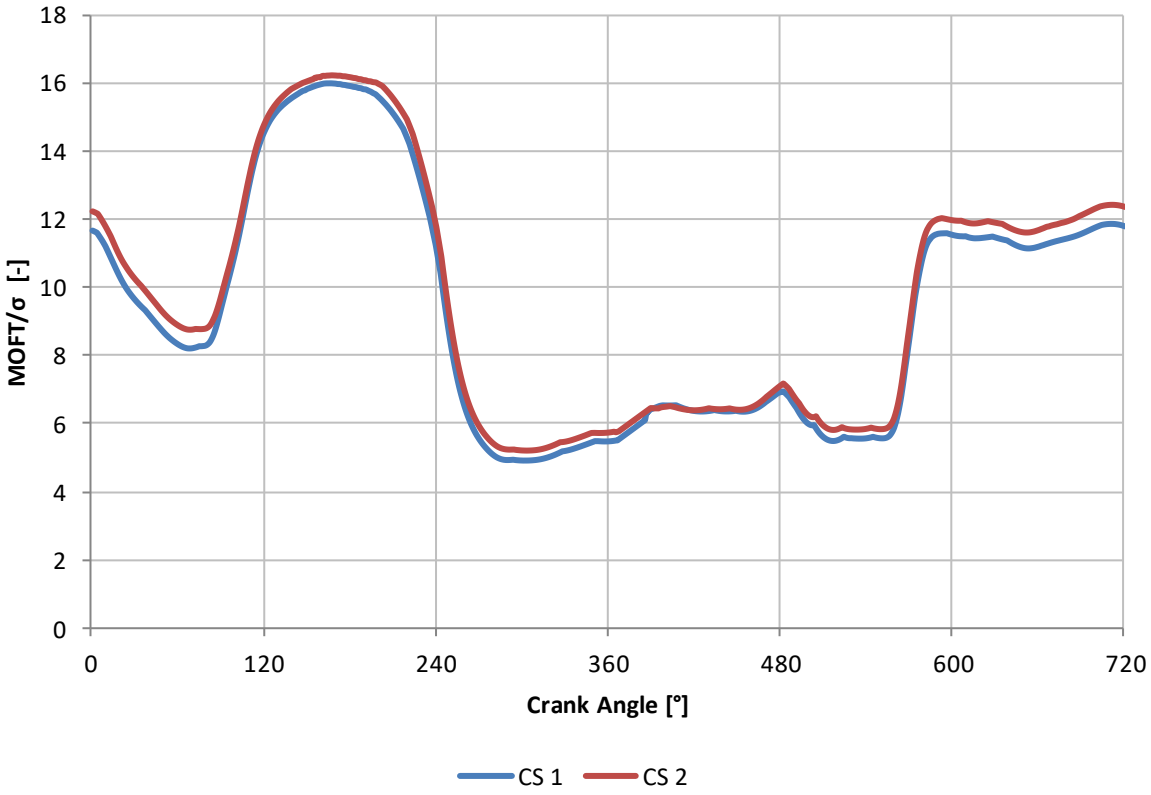

Figure B.16 Relation of the MOFT/σ of main bearing no.3 at OP 2

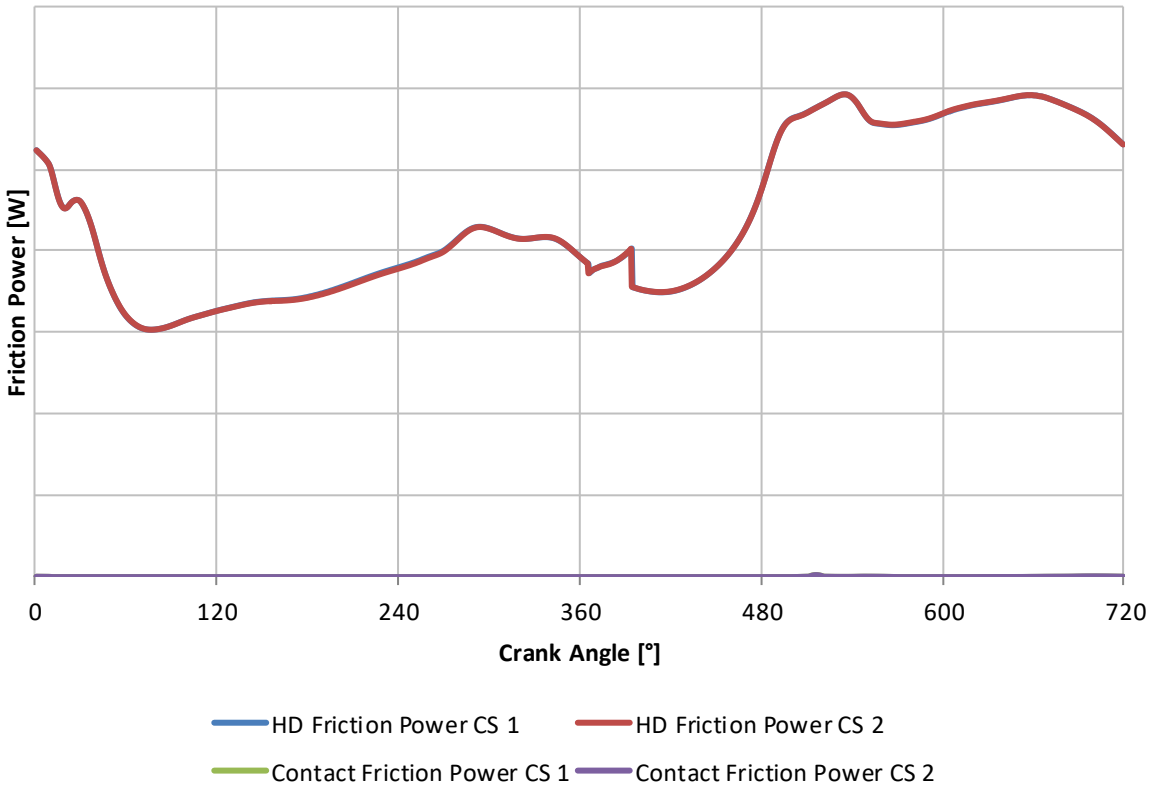

Figure B.17 Friction power of main bearing no.4 at OP 2

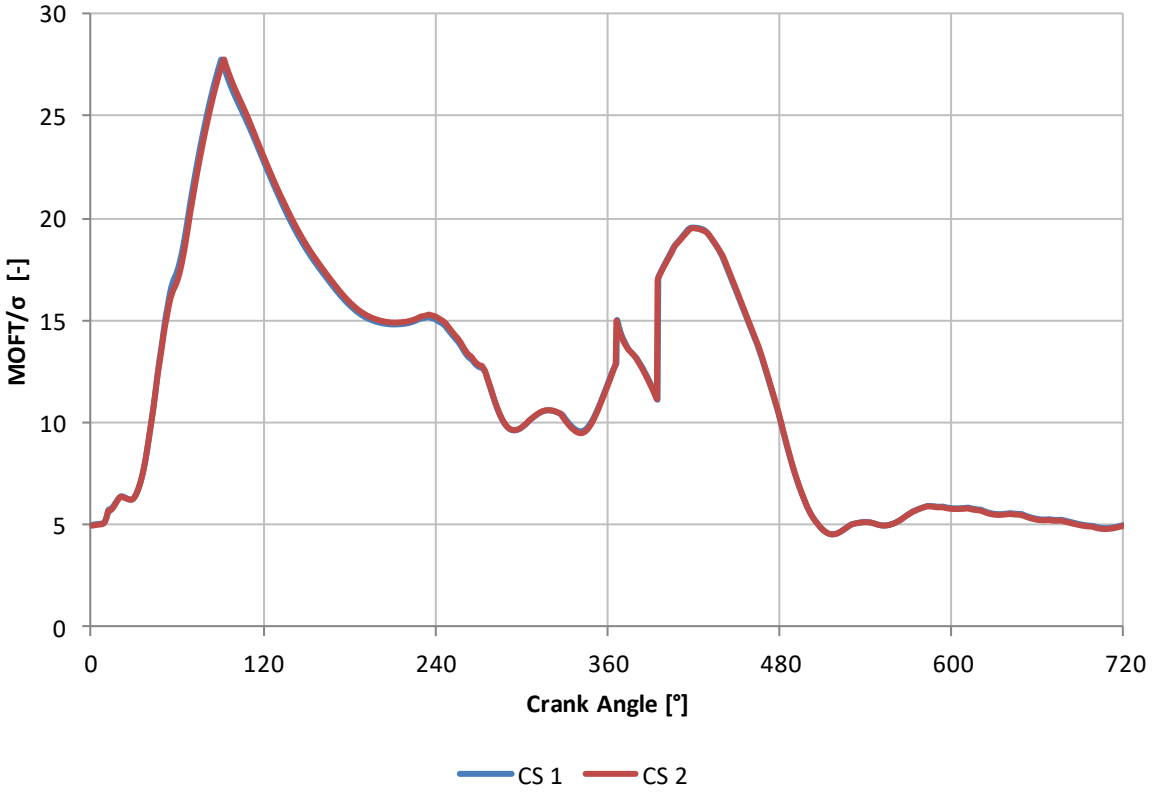

Figure B.18 Relation of the MOFT/σ of main bearing no.4 at OP 2

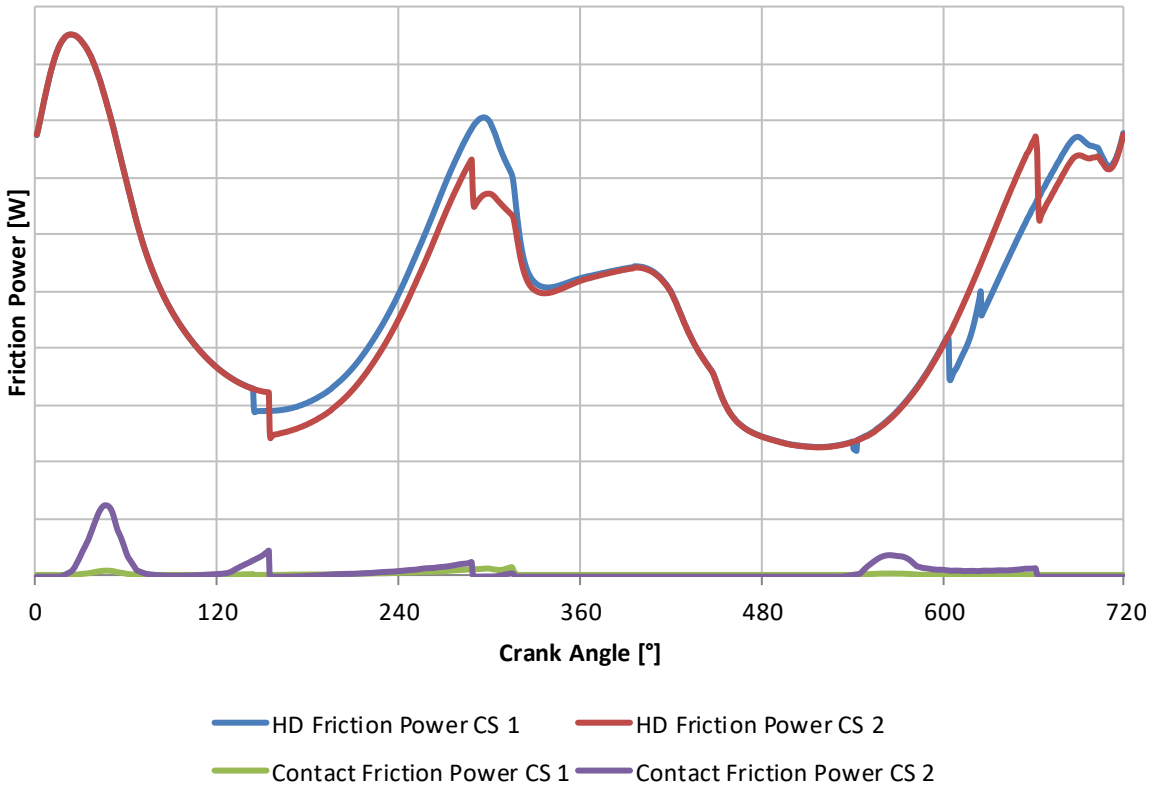

Figure B.19 Friction power of pin bearing at OP 2

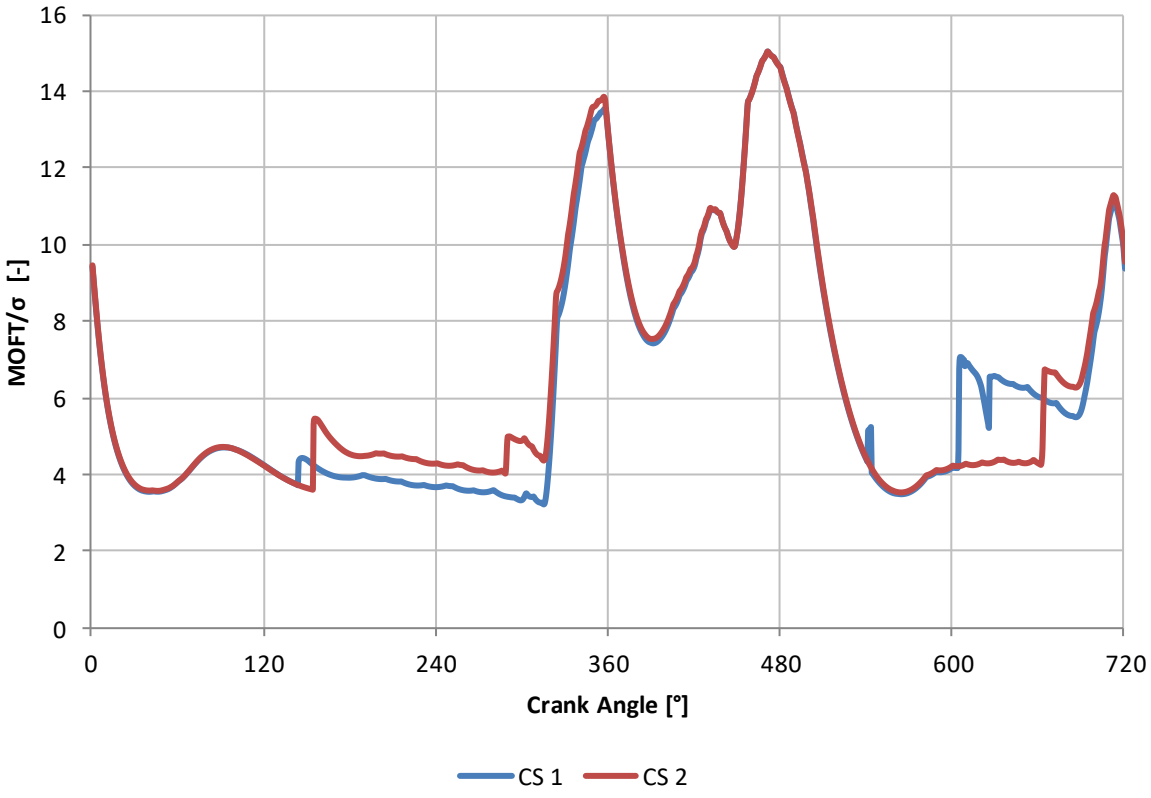

Figure B.20 Relation of the MOFT/σ of pin bearing at OP 2

Visualization of results at OP 3:

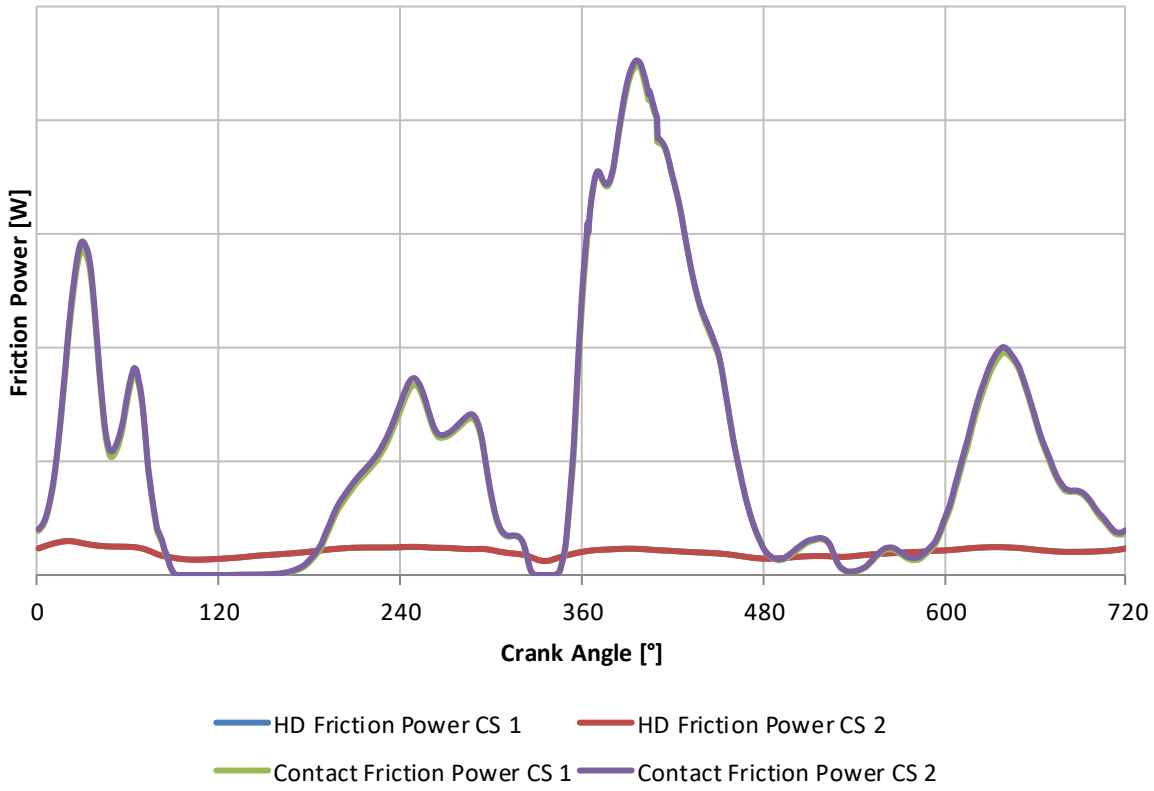

Figure B.21 Friction power of main bearing no.1 at OP 3

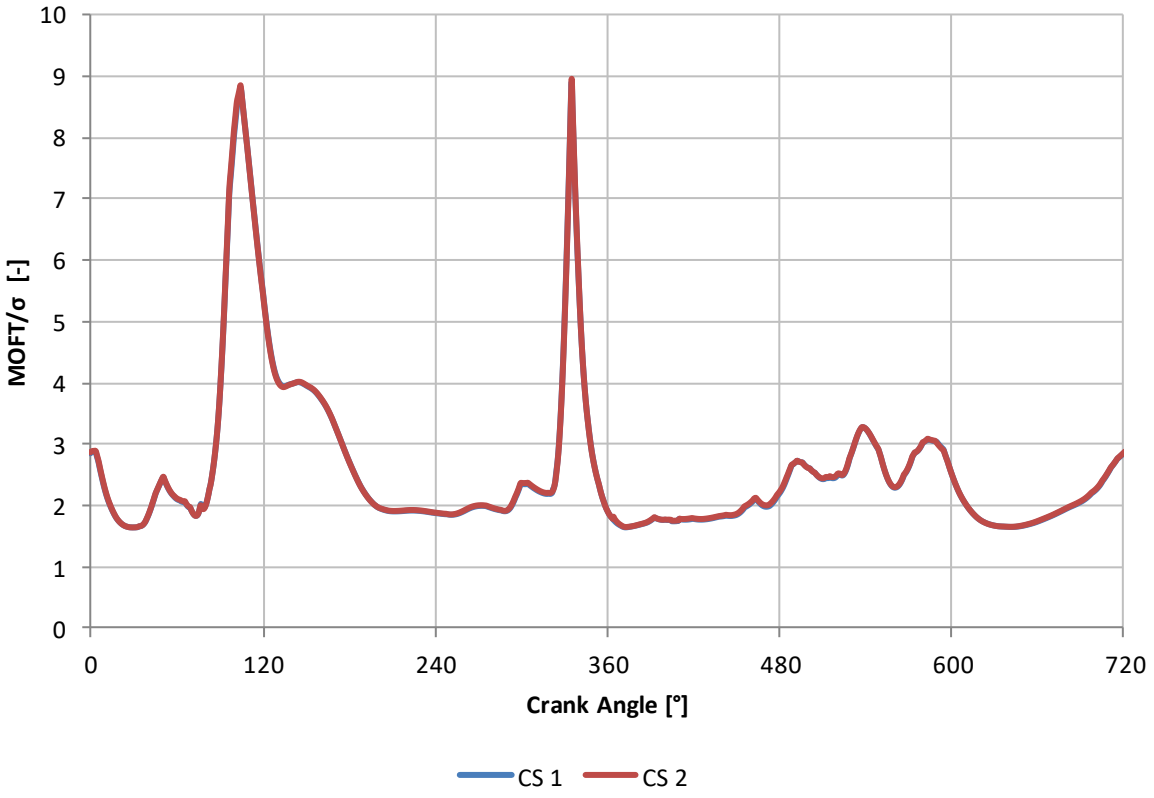

Figure B.22 Relation of the MOFT/σ of main bearing no.1 at OP 3

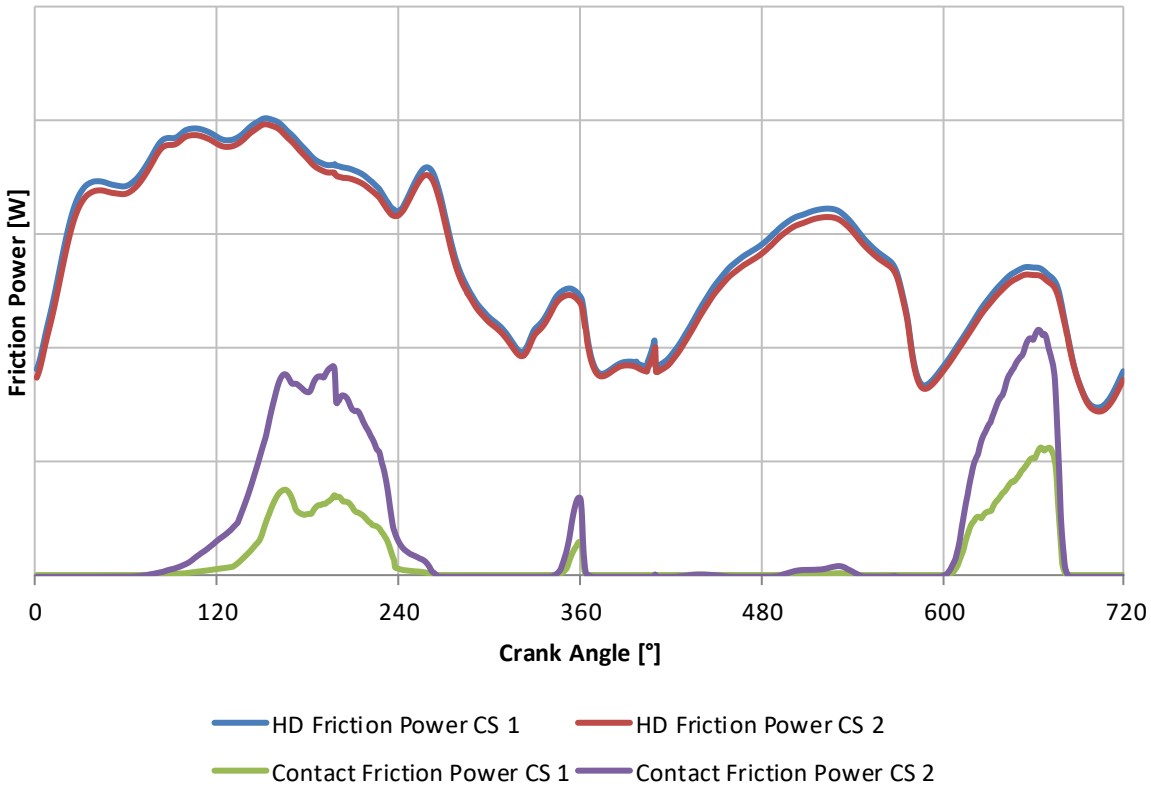

Figure B.23 Friction power of main bearing no.2 at OP 3

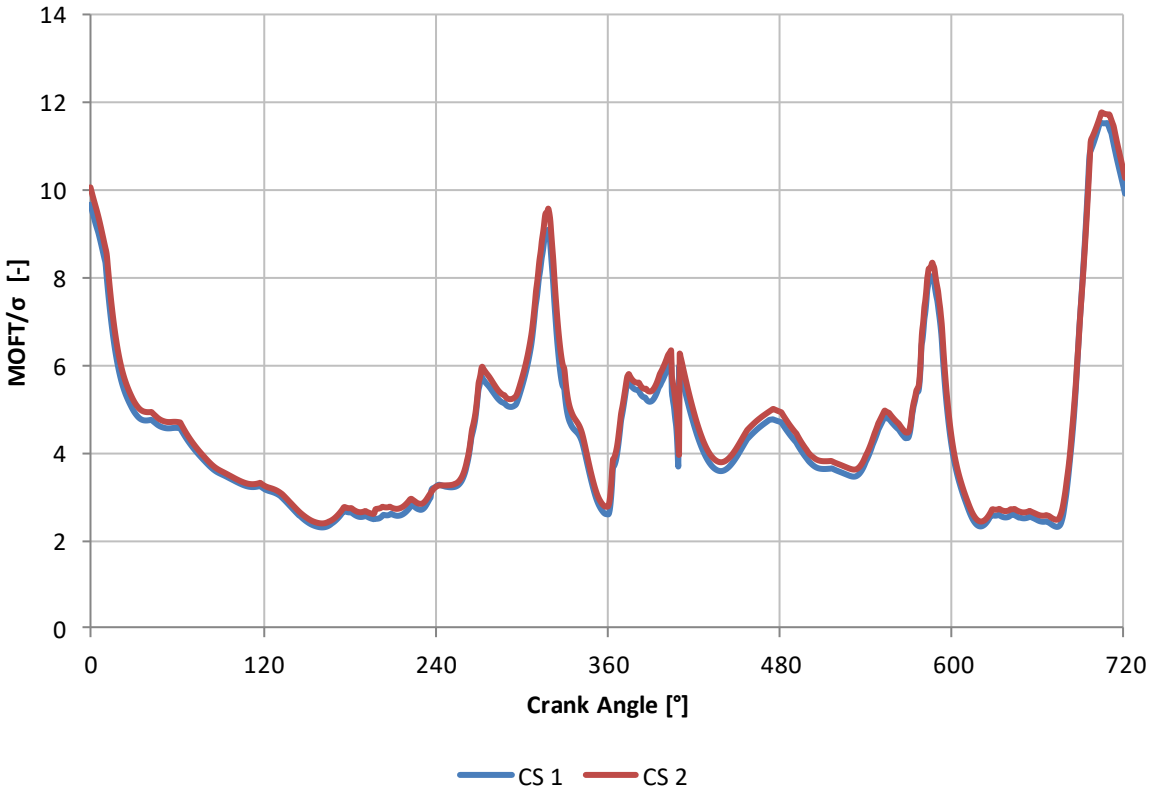

Figure B.24 Relation of the MOFT/σ of main bearing no.2 at OP 3

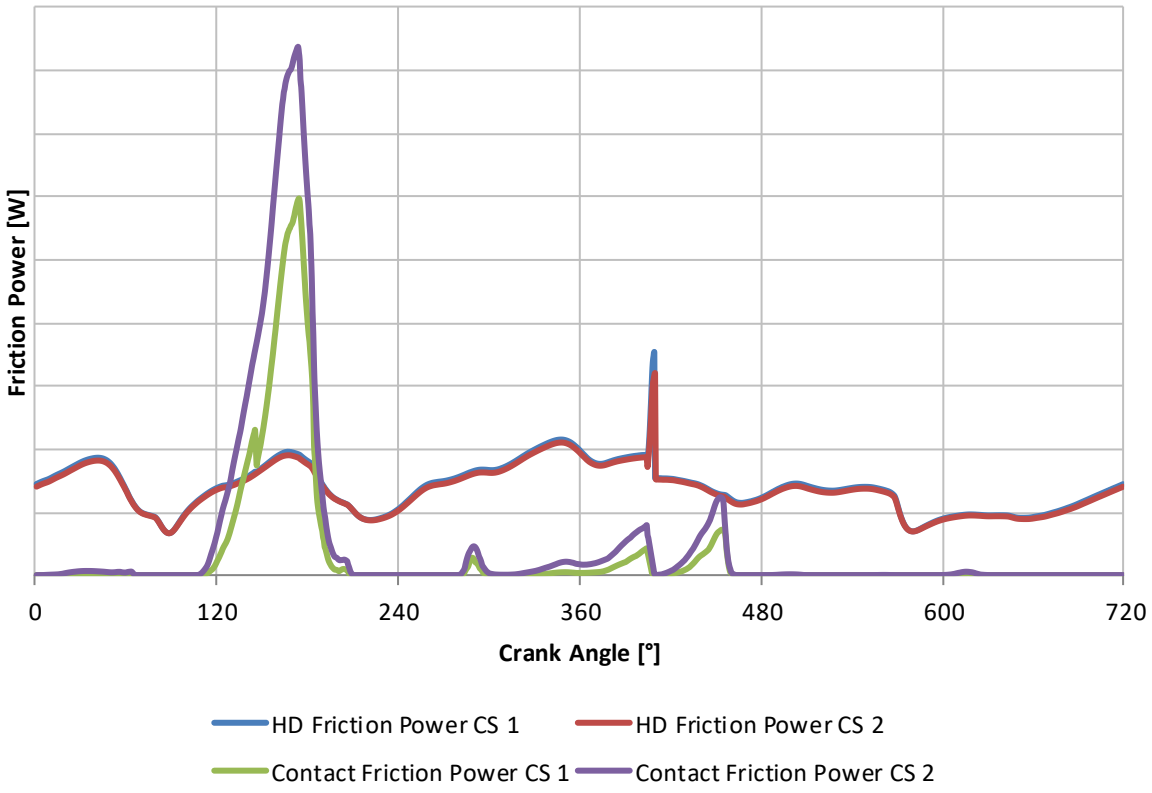

Figure B.25 Friction power of main bearing no.3 at OP 3

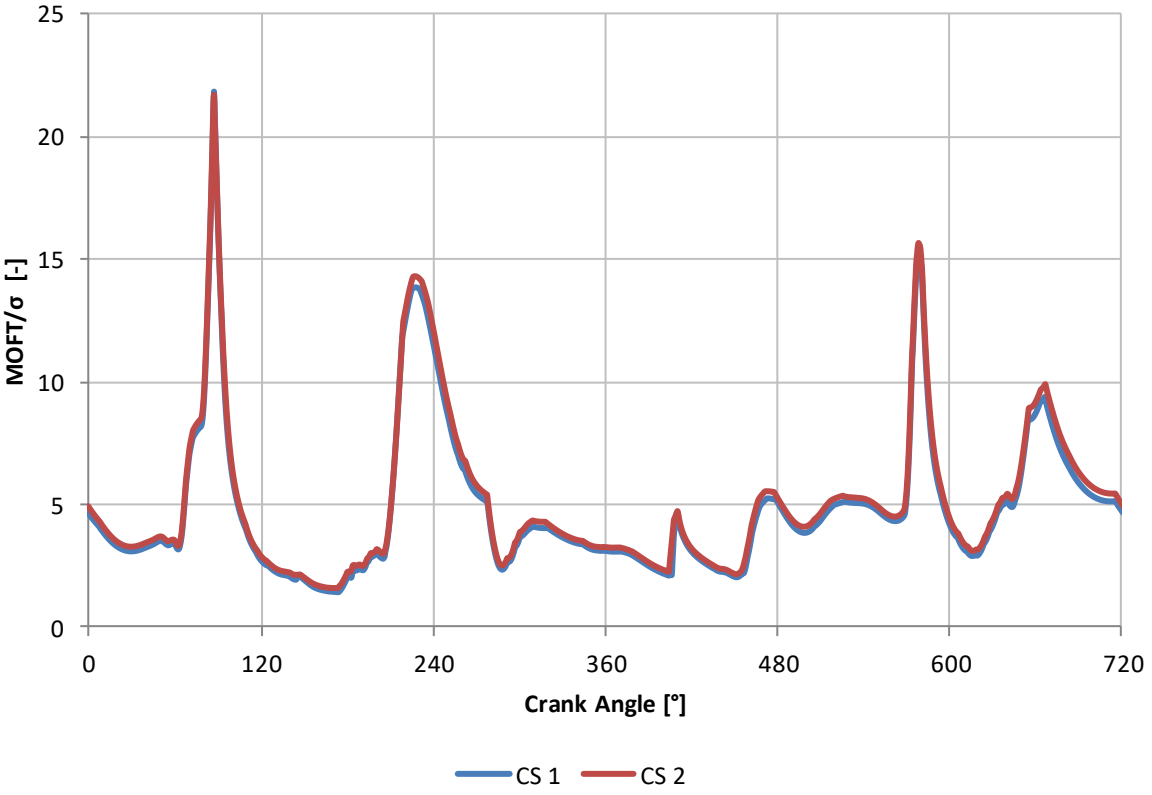

Figure B.26 Relation of the MOFT/σ of main bearing no.3 at OP 3

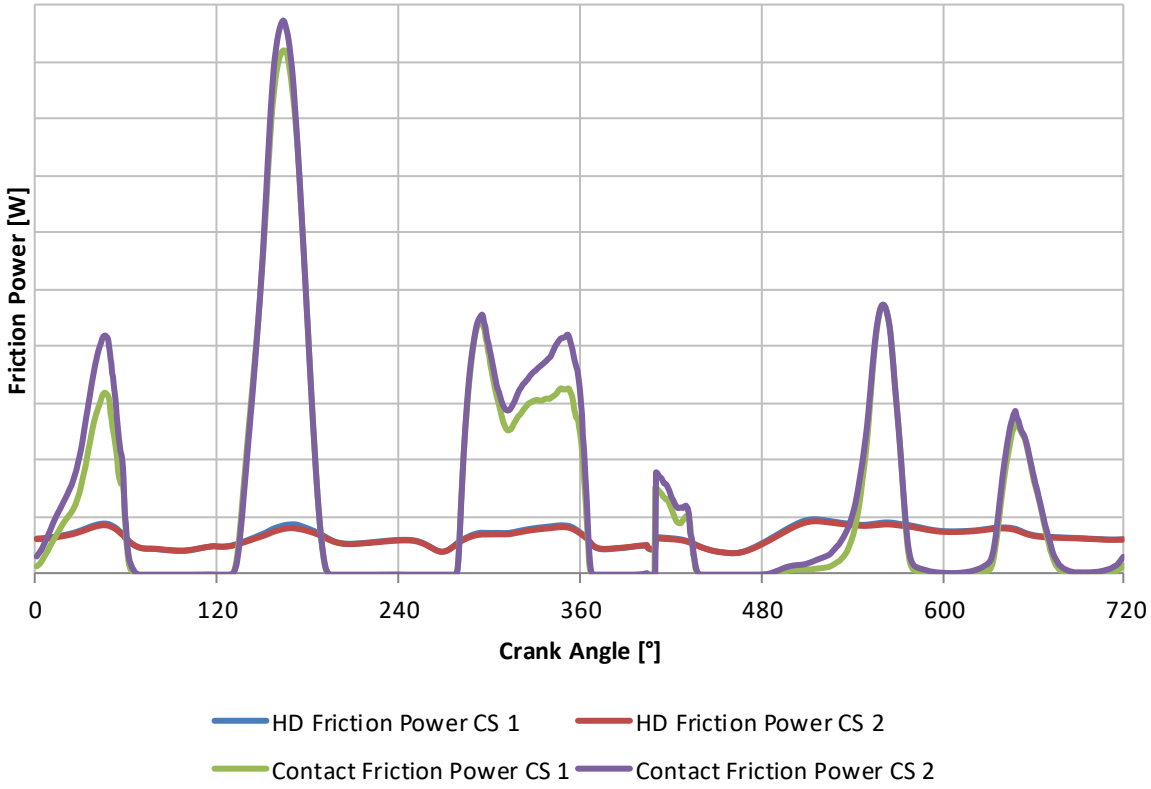

Figure B.27 Friction power of main bearing no.4 at OP 3

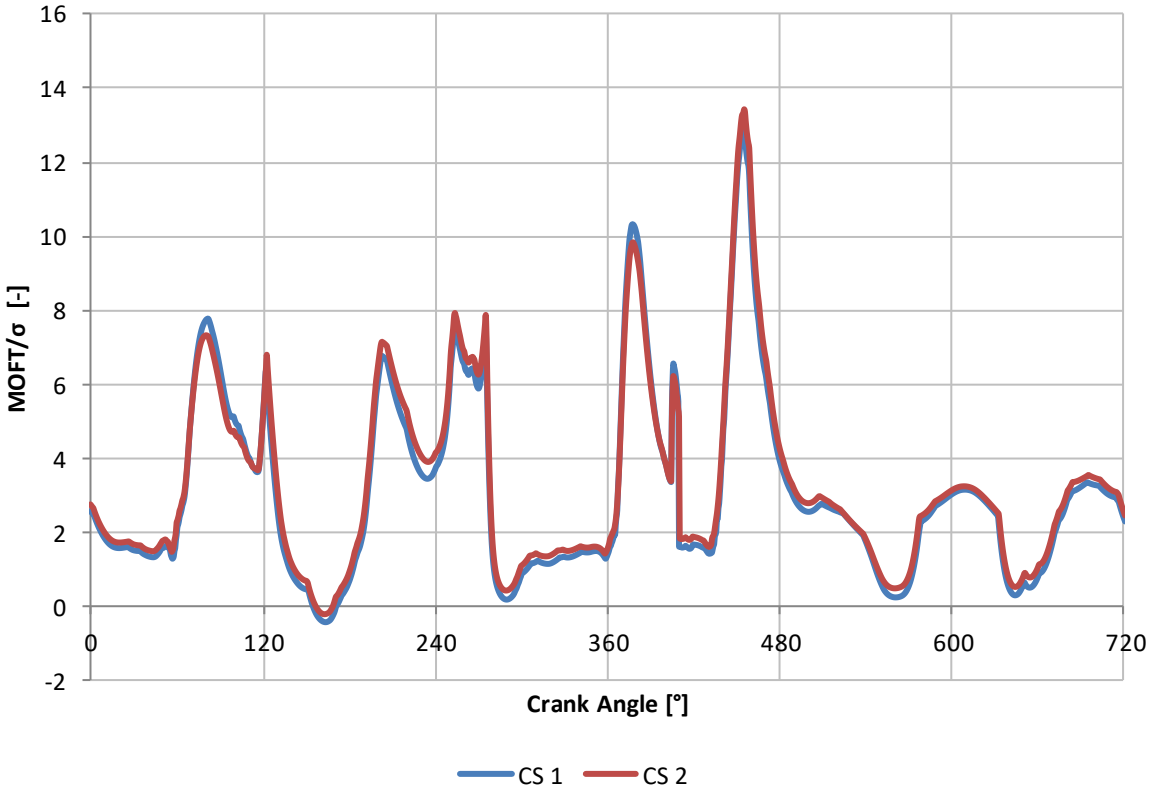

Figure B.28 Relation of the MOFT/σ of main bearing no.4 at OP 3

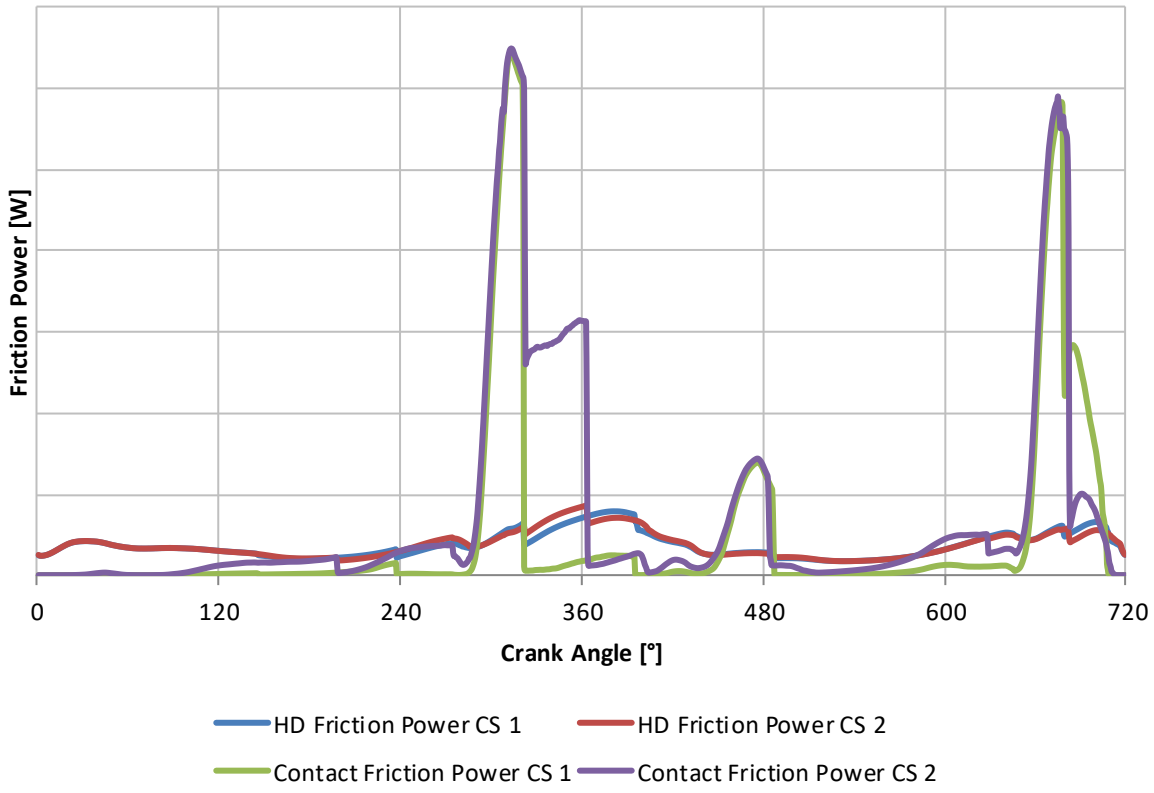

Figure B.29 Friction power of pin bearing at OP 3

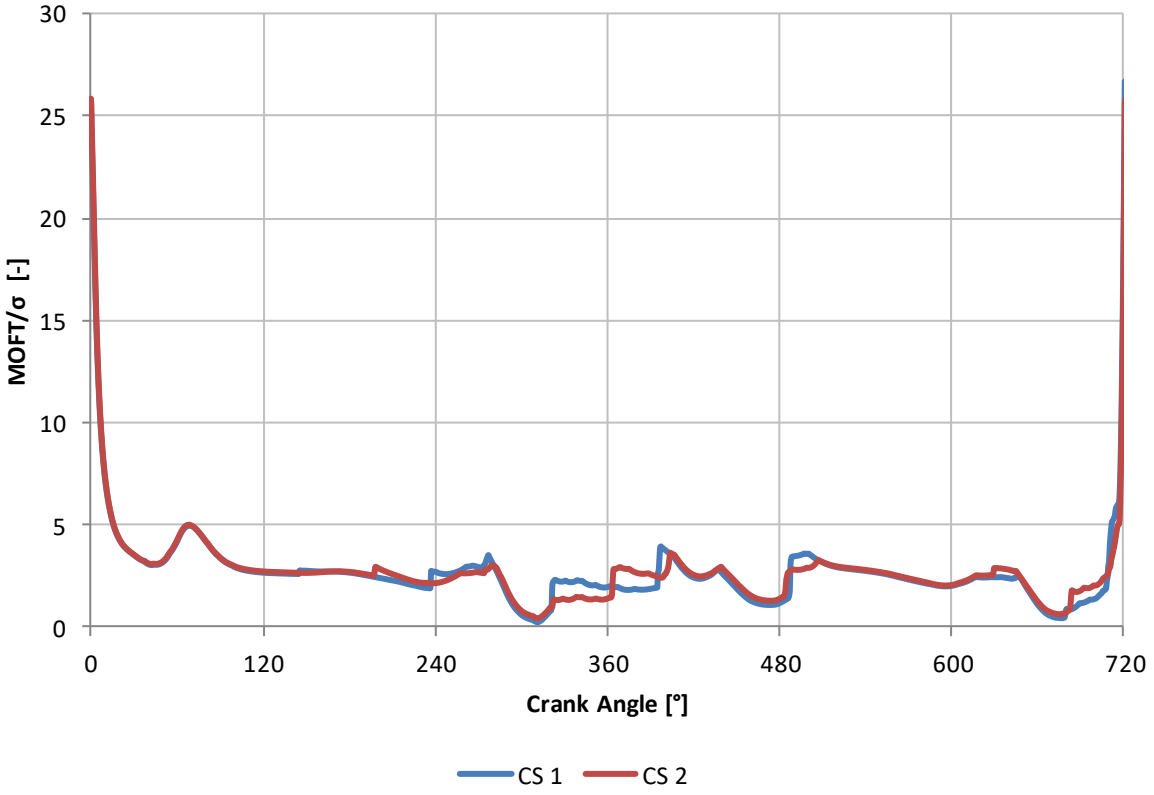

Figure B.30 Relation of the MOFT/σ of pin bearing at OP 3

Visualization of results at OP 4:

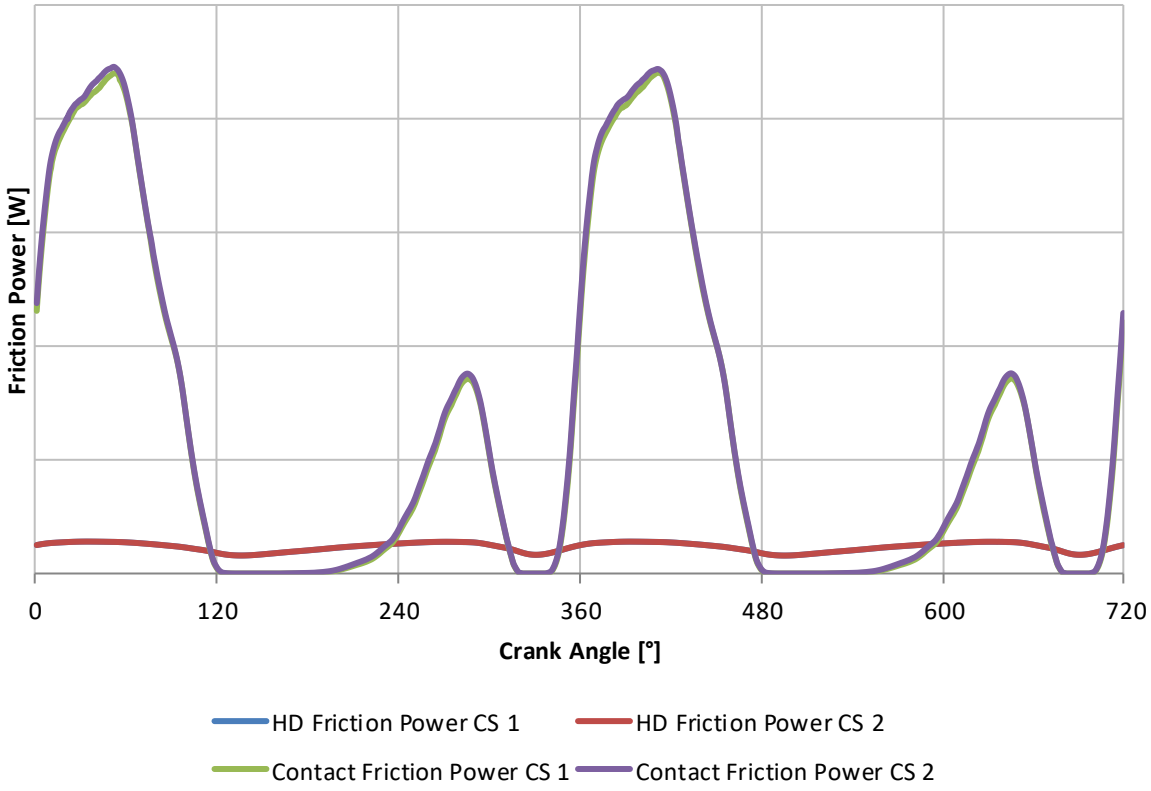

Figure B.31 Friction power of main bearing no.1 at OP 4

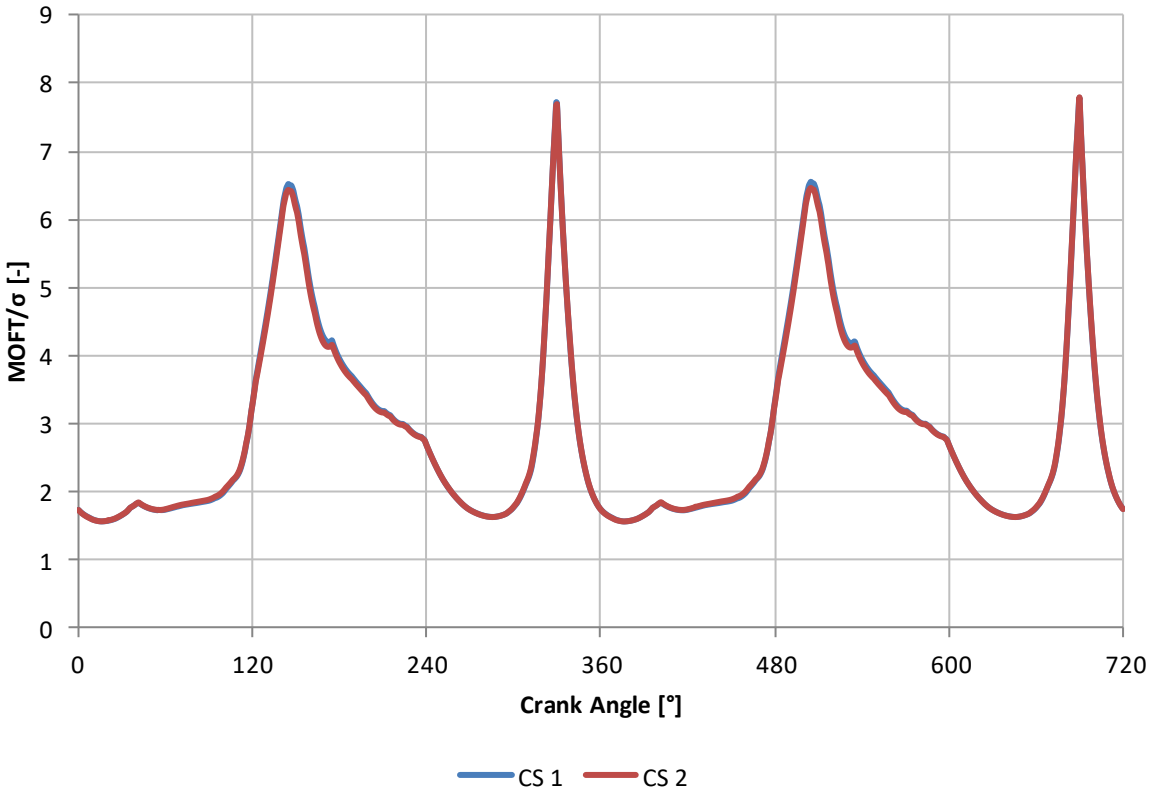

Figure B.32 Relation of the MOFT/σ of main bearing no.1 at OP 4

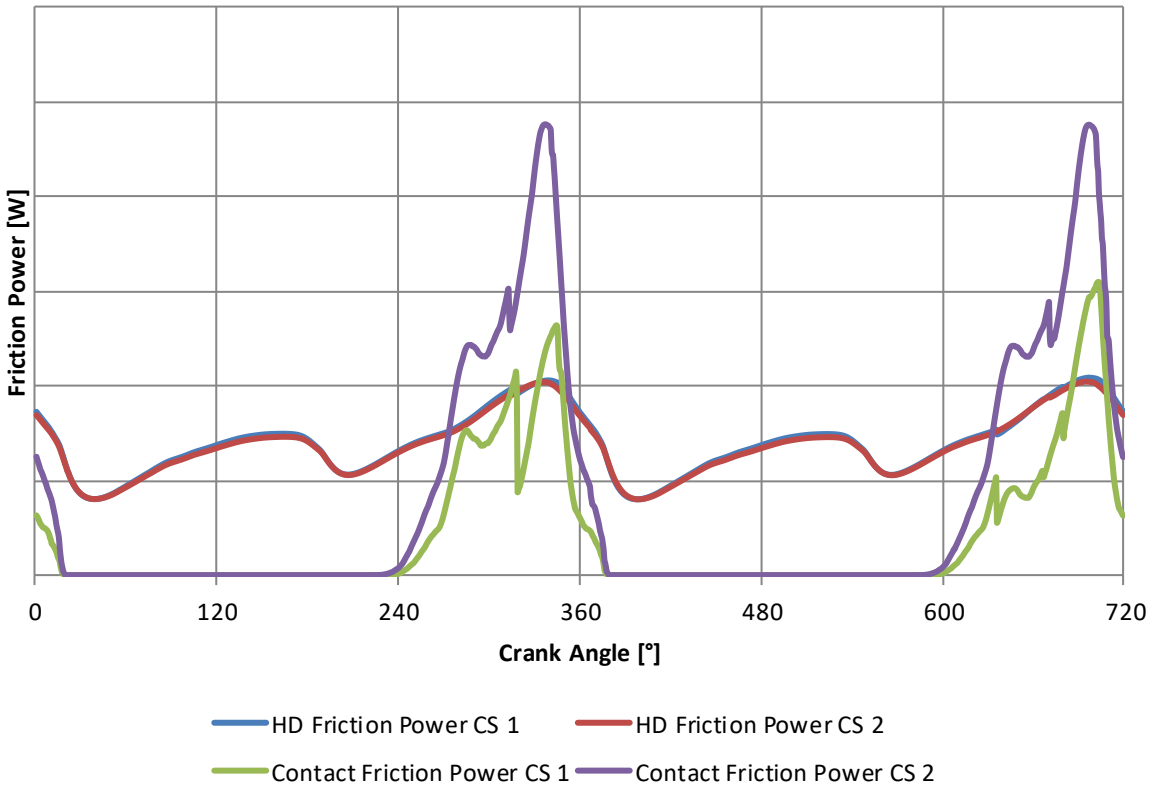

Figure B.33 Friction power of main bearing no.2 at OP 4

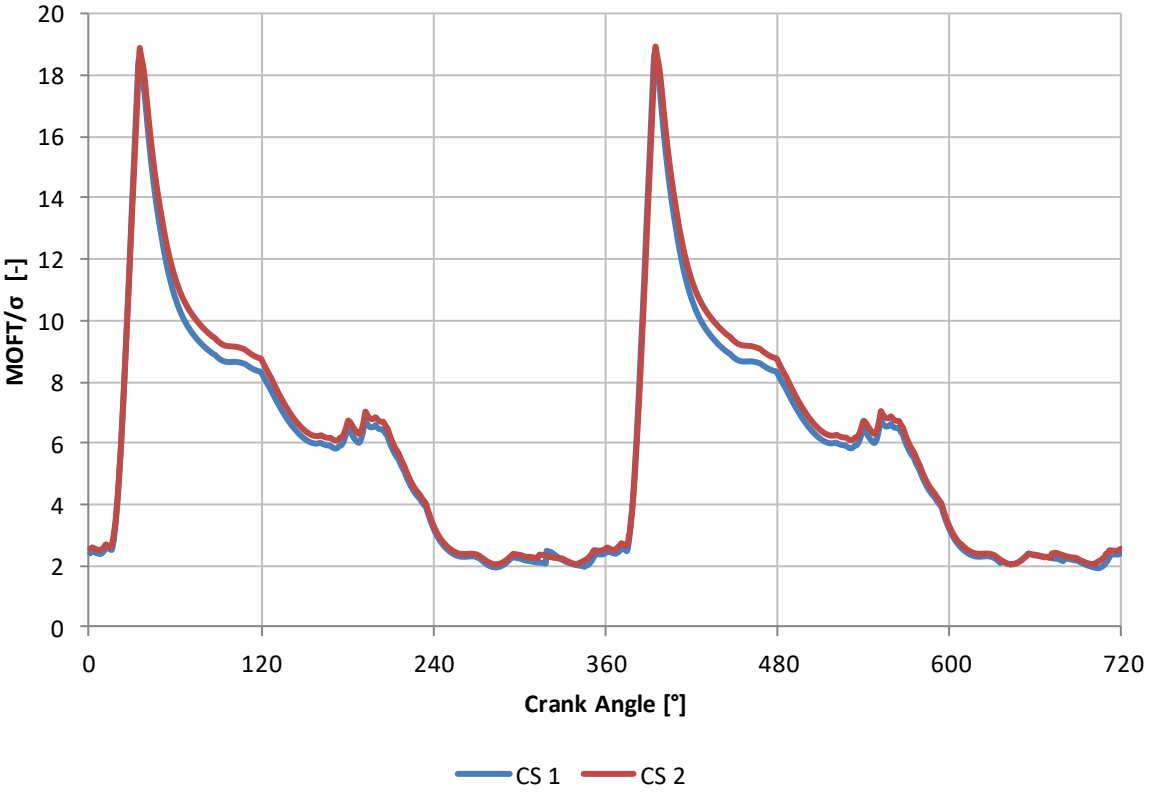

Figure B.34 Relation of the MOFT/σ of main bearing no.2 at OP 4

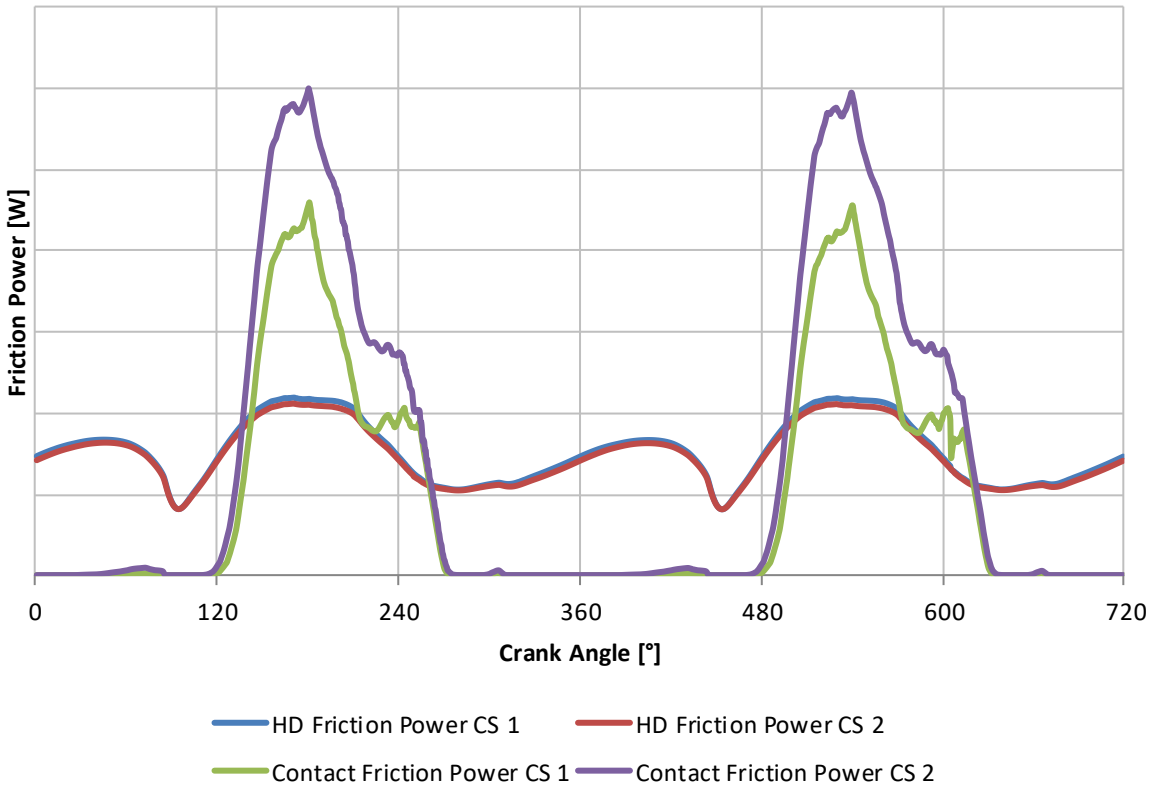

Figure B.35 Friction power of main bearing no.3 at OP 4

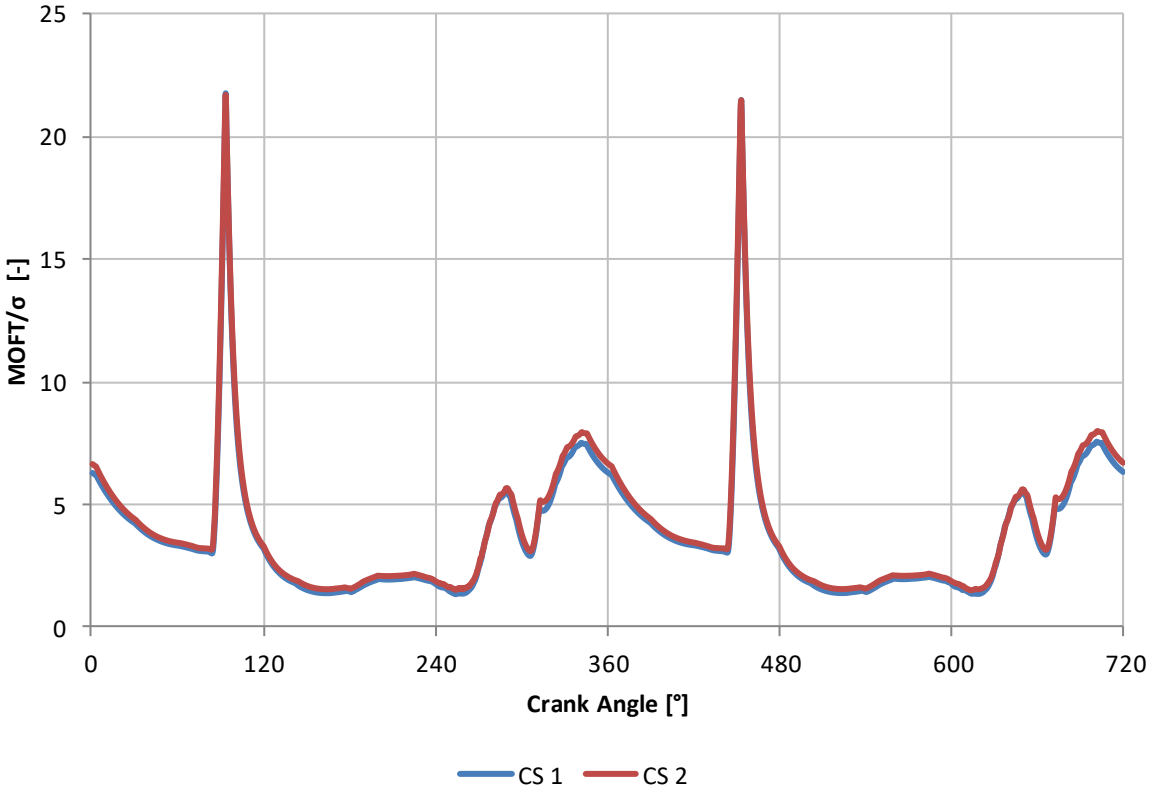

Figure B.36 Relation of the MOFT/σ of main bearing no.3 at OP 4

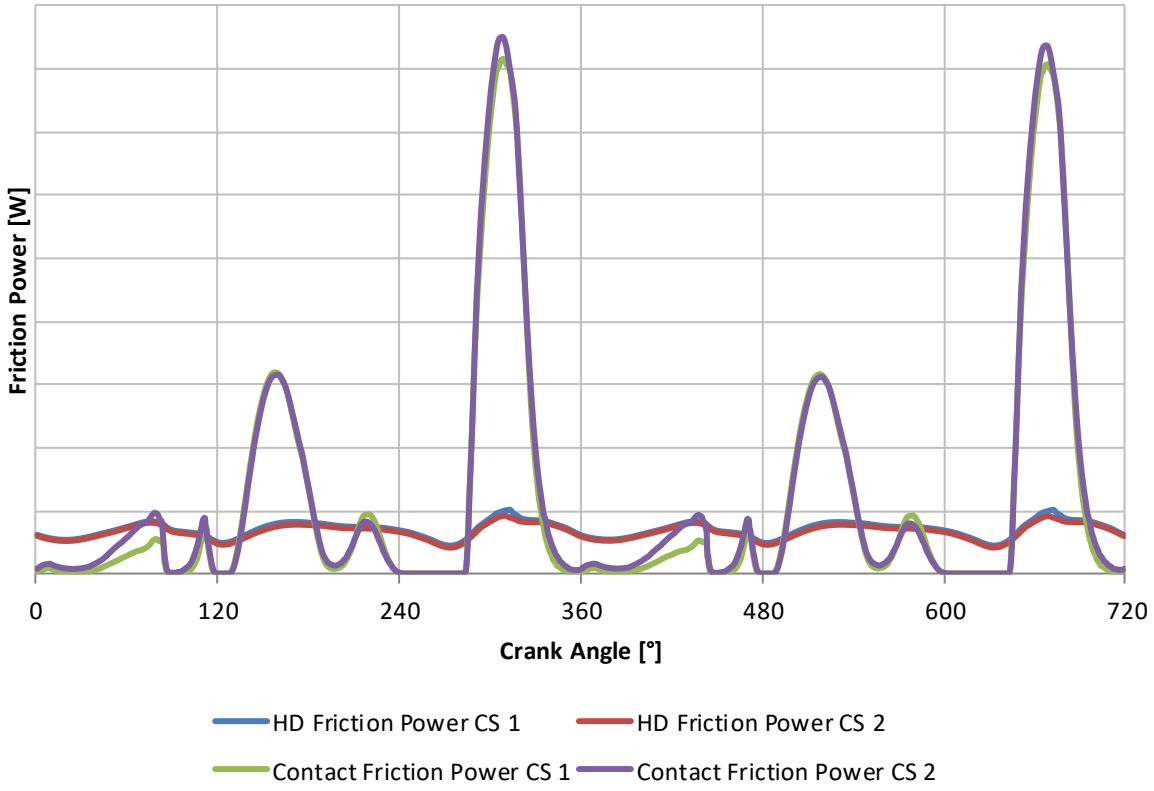

Figure B.37 Friction power of main bearing no.4 at OP 4

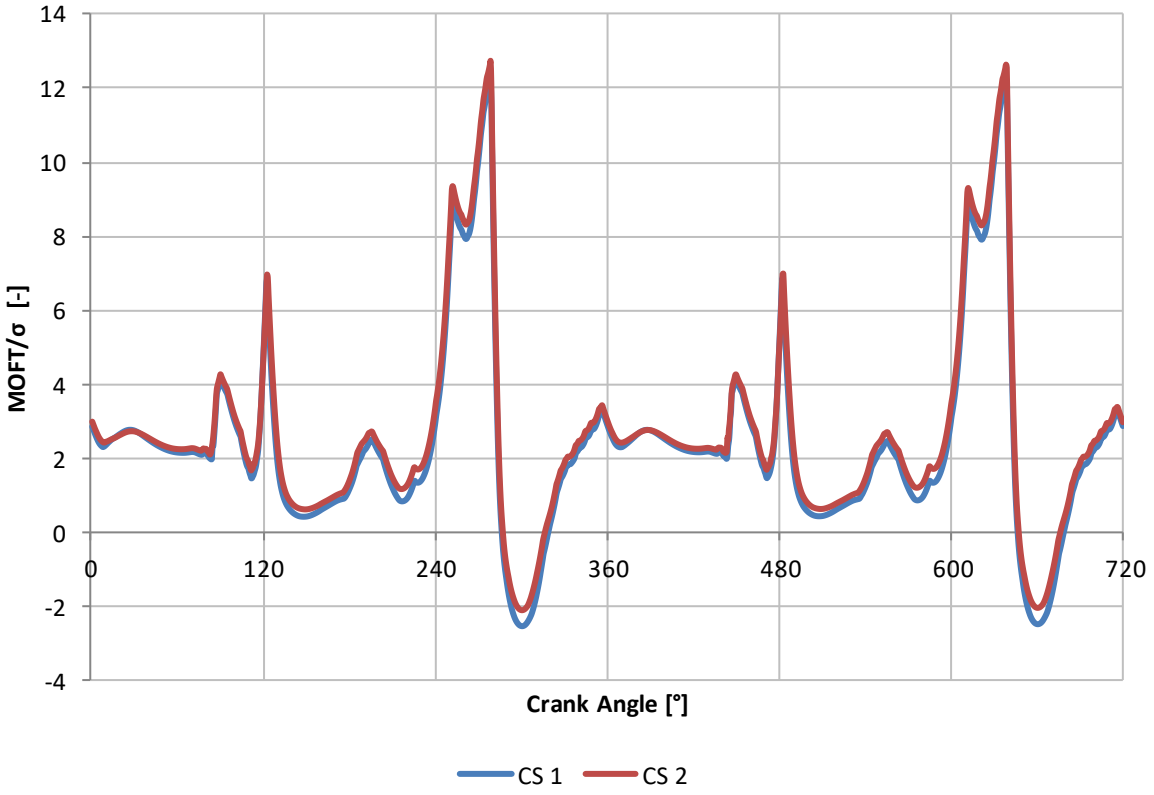

Figure B.38 Relation of the MOFT/σ of main bearing no.4 at OP 4

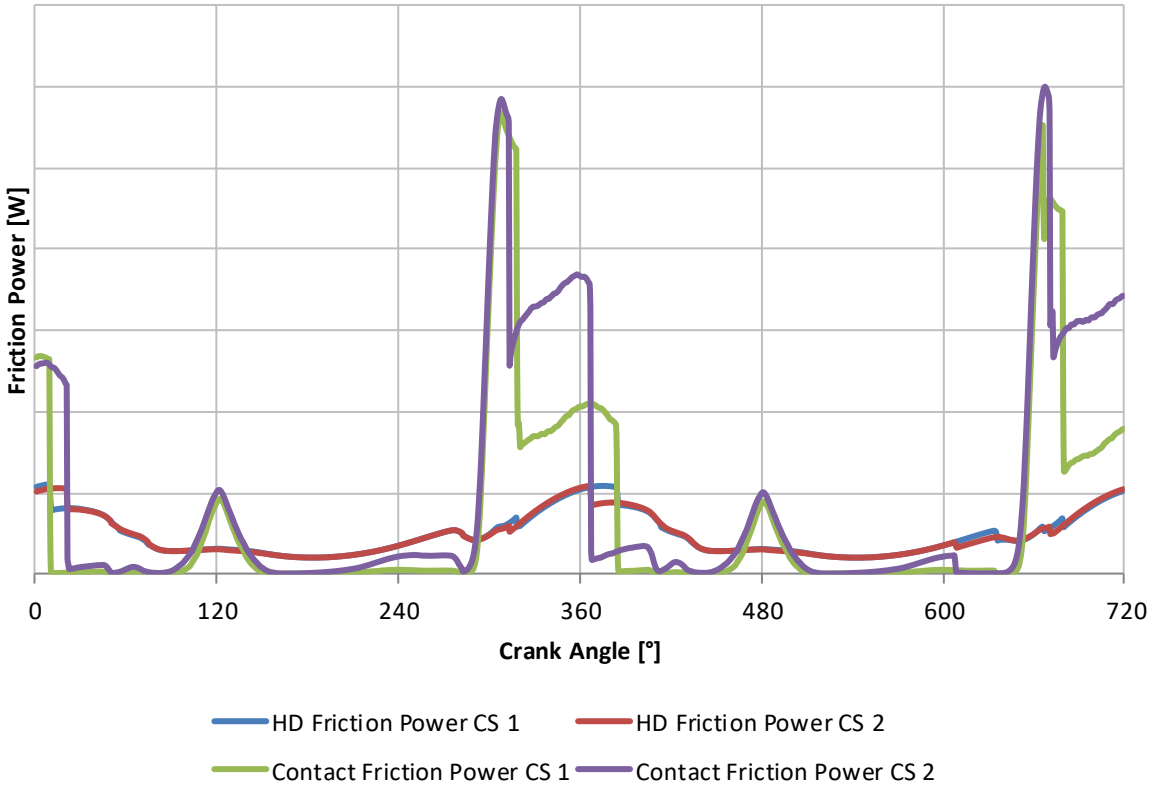

Figure B.39 Friction power of pin bearing at OP 4

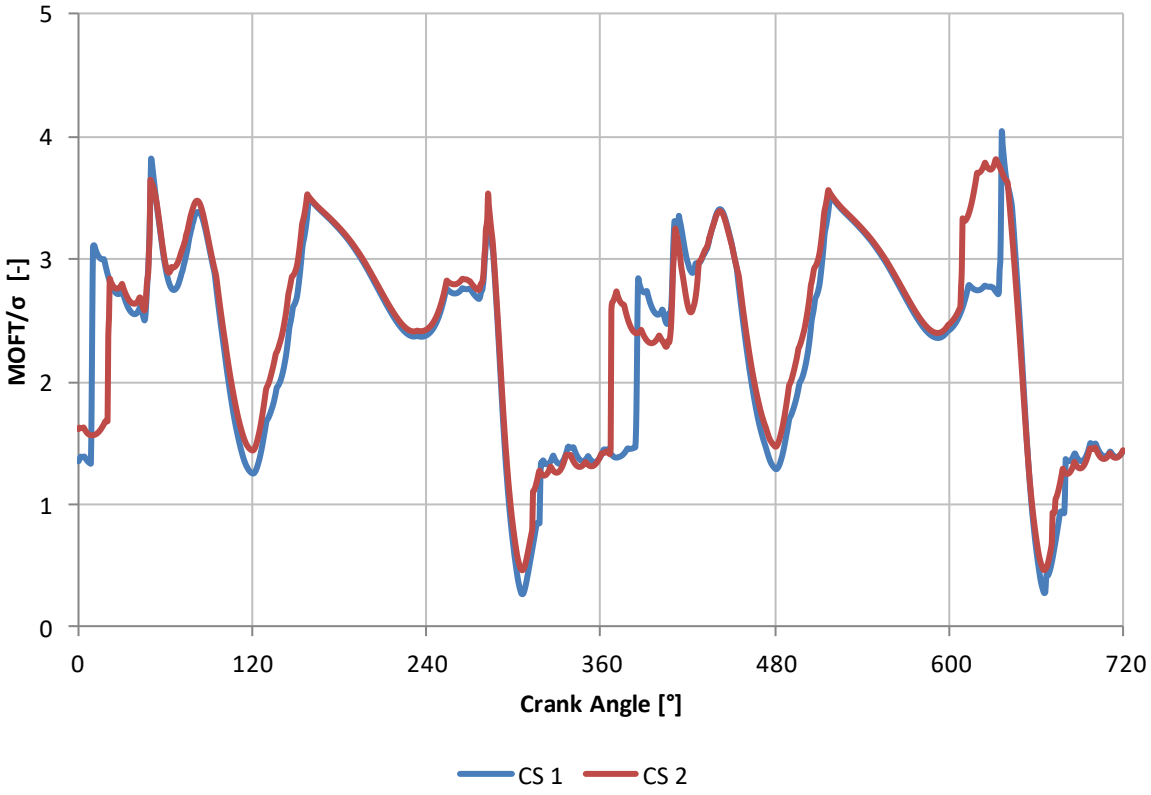

Figure B.40 Relation of the MOFT/σ of pin beargin at OP 4